UNIVERSITY OF ADELAIDE LIBRARY
24/7/86

The University of Adelaide
Department of Geology and Geophysics

LONGITUDINAL DUNES: THEIR GENESIS AND ORDERING

by

George Kuang Yee Tseo

Volume Two
(figures and plates)

January, 1986

A thesis submitted to the University of Adelaide
in fulfilment of the requirements for the
degree of
Doctor of Philosophy

Awarded 16-4-86

List of Plates

List of Figures

UNIVERSITY OF ADELAIDE LIBRARY

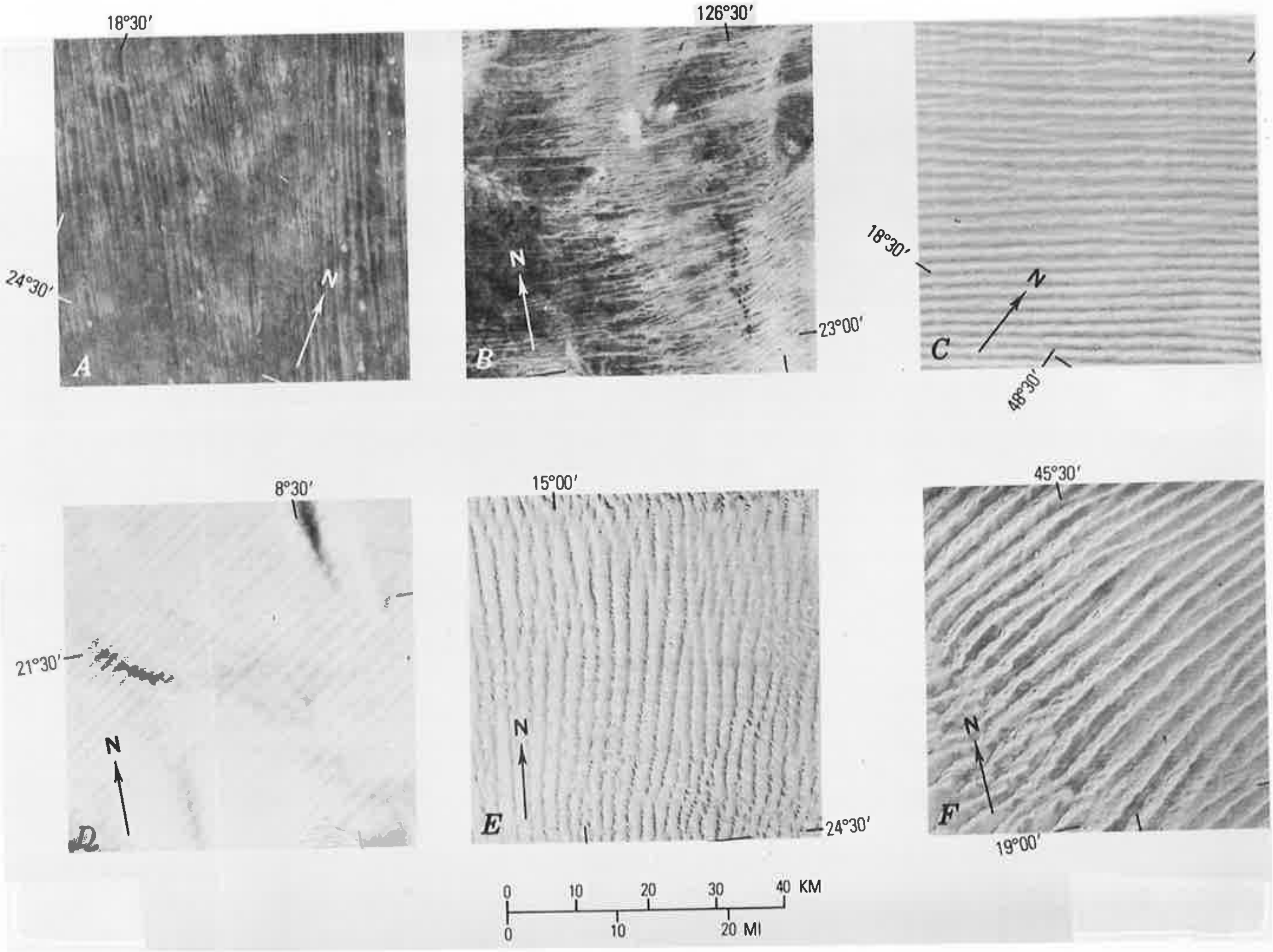

Plate 1. "Landsat imagery sample areas on which measurements of linear width, length, and wavelength were made. Numbers in parentheses refer to the regions listed in table 36. Each sample is an area 50 km by 50 km, or 2,500 km^2 (1,550 mi^2) in a sand sea. A) Kalahari Desert southern Africa; simple dunes B) Great Sandy Desert, Australia; simple dunes C) Southwestern Rub' al Khali, Saudi Arabia; compound dunes D) Southwestern Sahara; compound dunes E) Namib Desert, South-west Africa; complex dunes F) Western Rub' al Khali, Saudi Arabia; complex dunes." (From BREED and GROW, 1979).

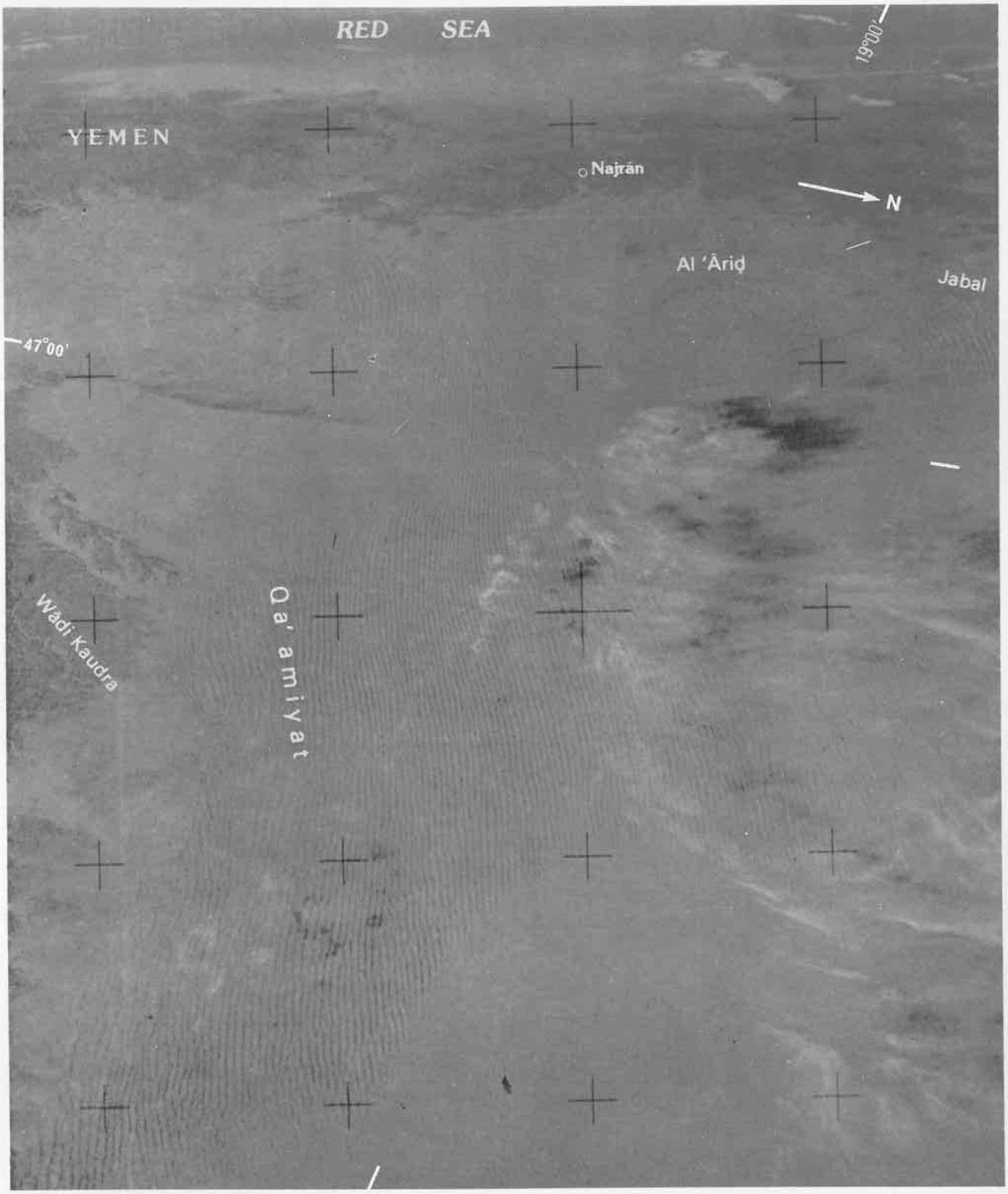

Plate 2. "Red linear dunes extending 600 km (360 mi) across the western Rub' al Khali to the foothills of Yemen. Skylab oblique photograph SL4-4643. Dunes in the Qa'amiyat region have an average crest-to-crest distance of 2.1 km (1.3 mi) and are commonly more than 100 km (60 mi) long." (From BREED et al., 1979).

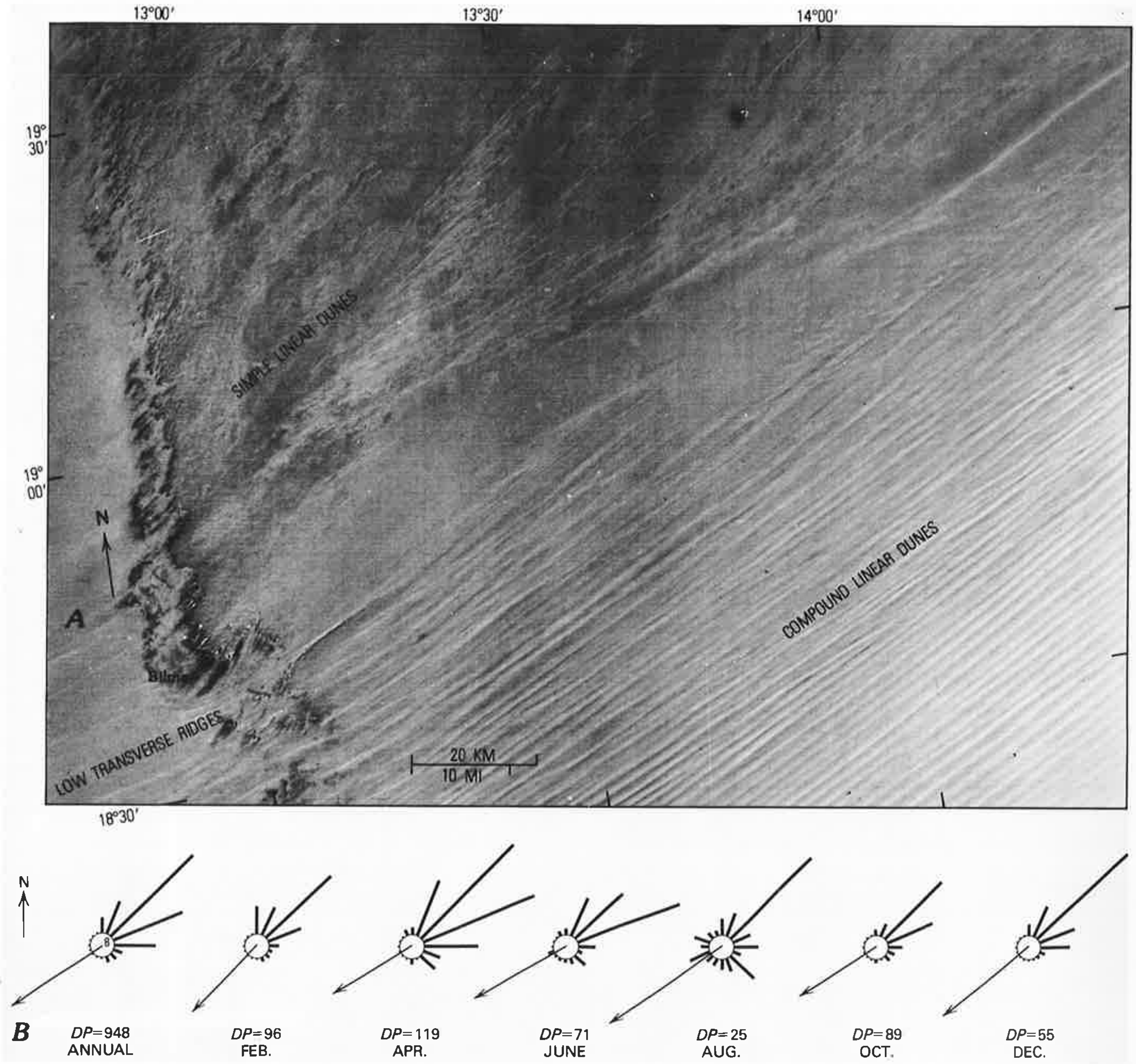

Plate 3. "Landsat imagery of linear dunes A) in the Erg Bilma. Both simple and compound linear dunes occur near Bilma in the same regional wind environment. B) Annual and six monthly sand roses for Bilma, Niger, illustrate a wide unimodal high-energy wind regime near the dunes. Arrow indicates resultant drift direction. Number in center circle of rose is reduction factor. DP (drift potential, in vector units) is given for each rose." (From FRYBERGER, 1979).

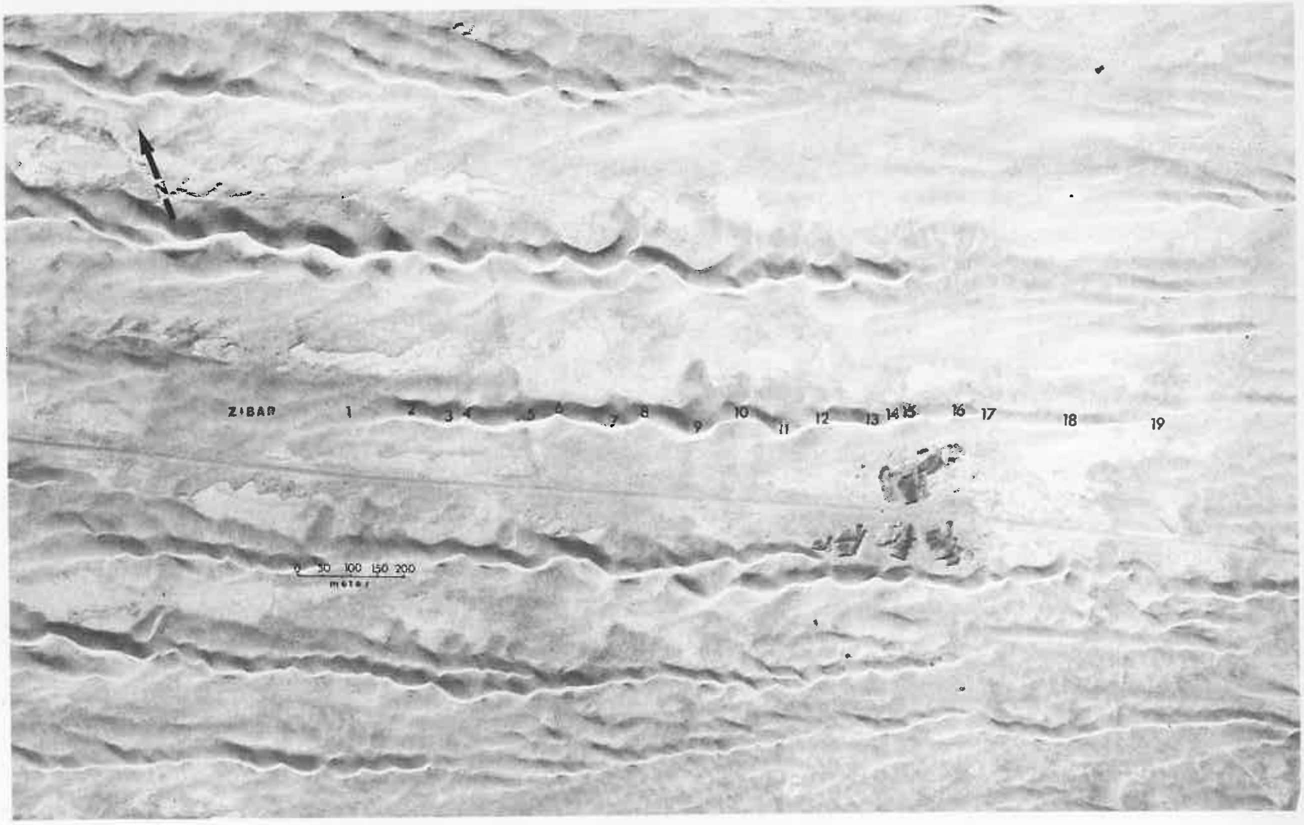

Plate 4. Snaking linear dune of the Negev Desert, Israel. Numbers are reference points used in TSOAR, 1978. (Original image provided to TSOAR Geological Survey of Israel, Tel Aviv).

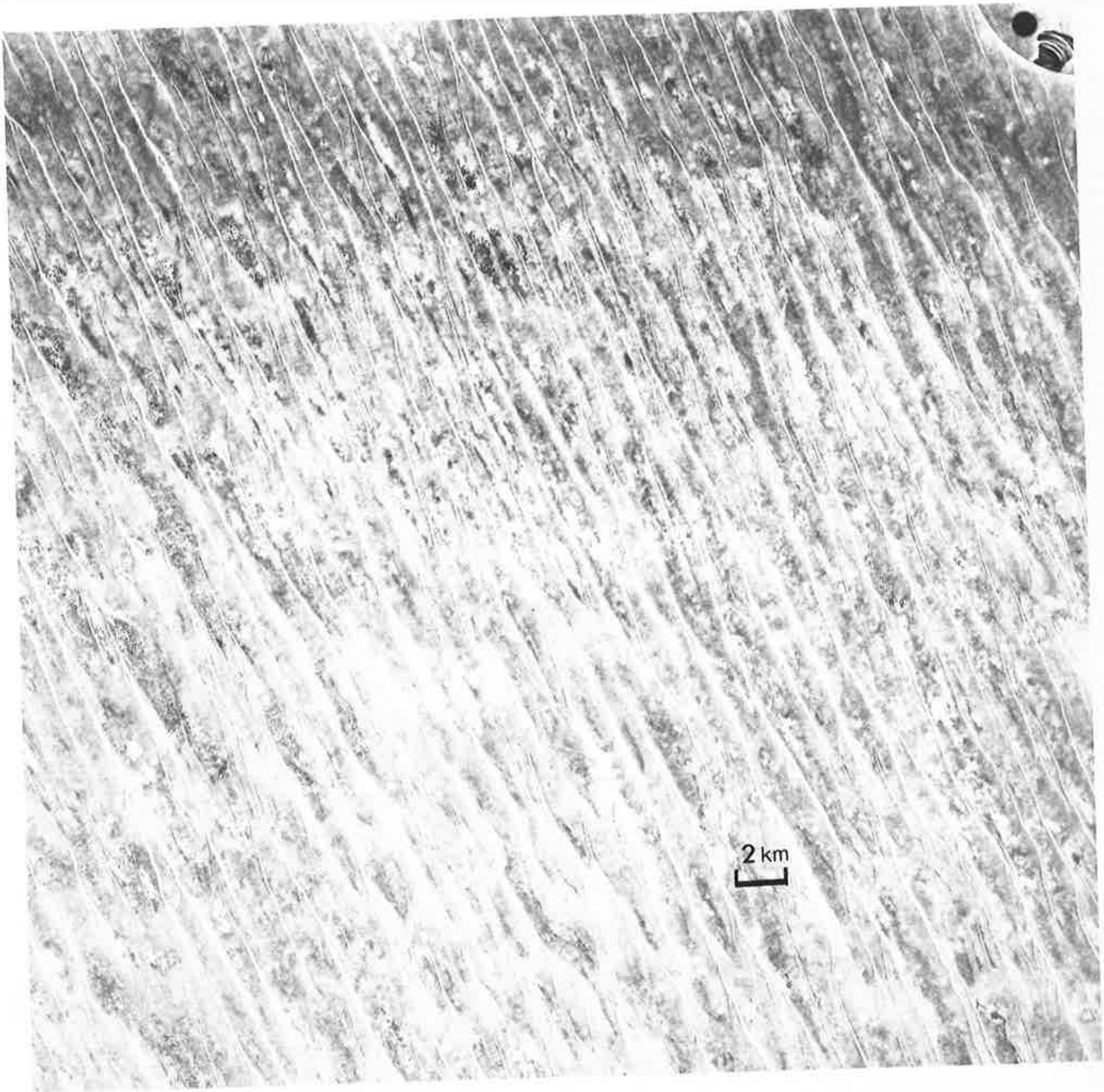

Plate 5. Simpson Desert dunes. (Poolowanna 1:250,000 photograph, SVY. 2445, Department of Lands, South Australia).

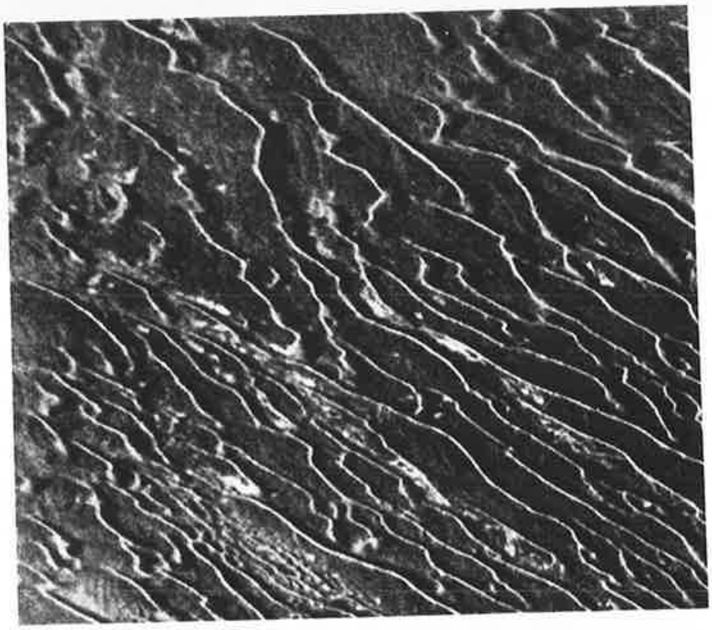

Plate 6. "Fishinghook" linear dunes of western China. (From CHINA TAMES HER DESERTS, 1977).

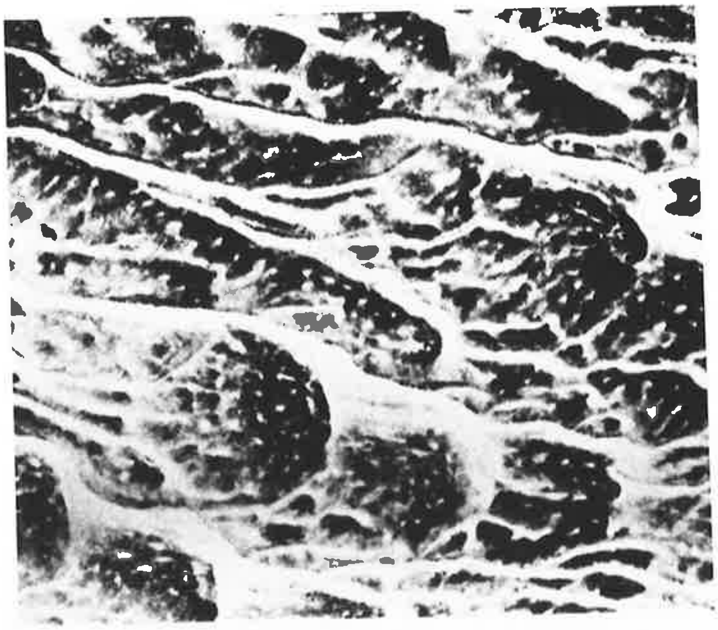

Plate 7. "Honeycomb" linear dunes of western China. (From CHINA TAMES HER DESERTS, 1977).

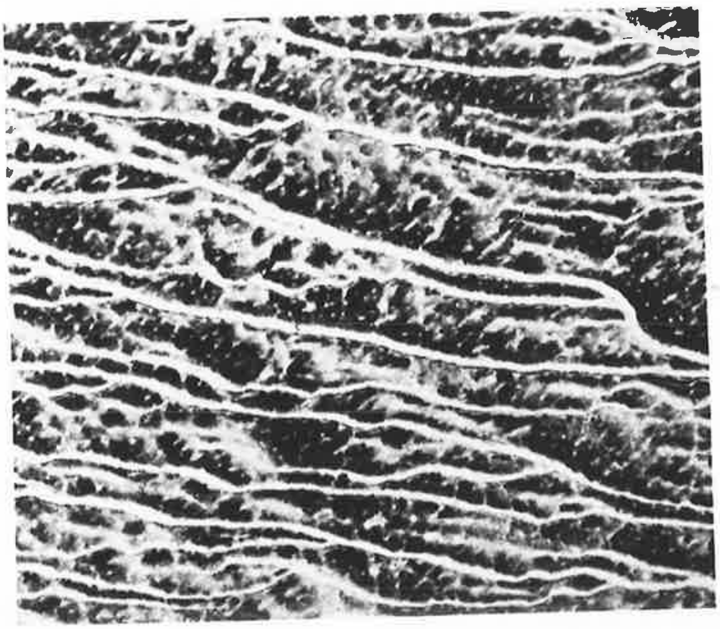

Plate 8. "Dendritic" linear dunes of western China. (From CHINA TAMES HER DESERTS, 1977).

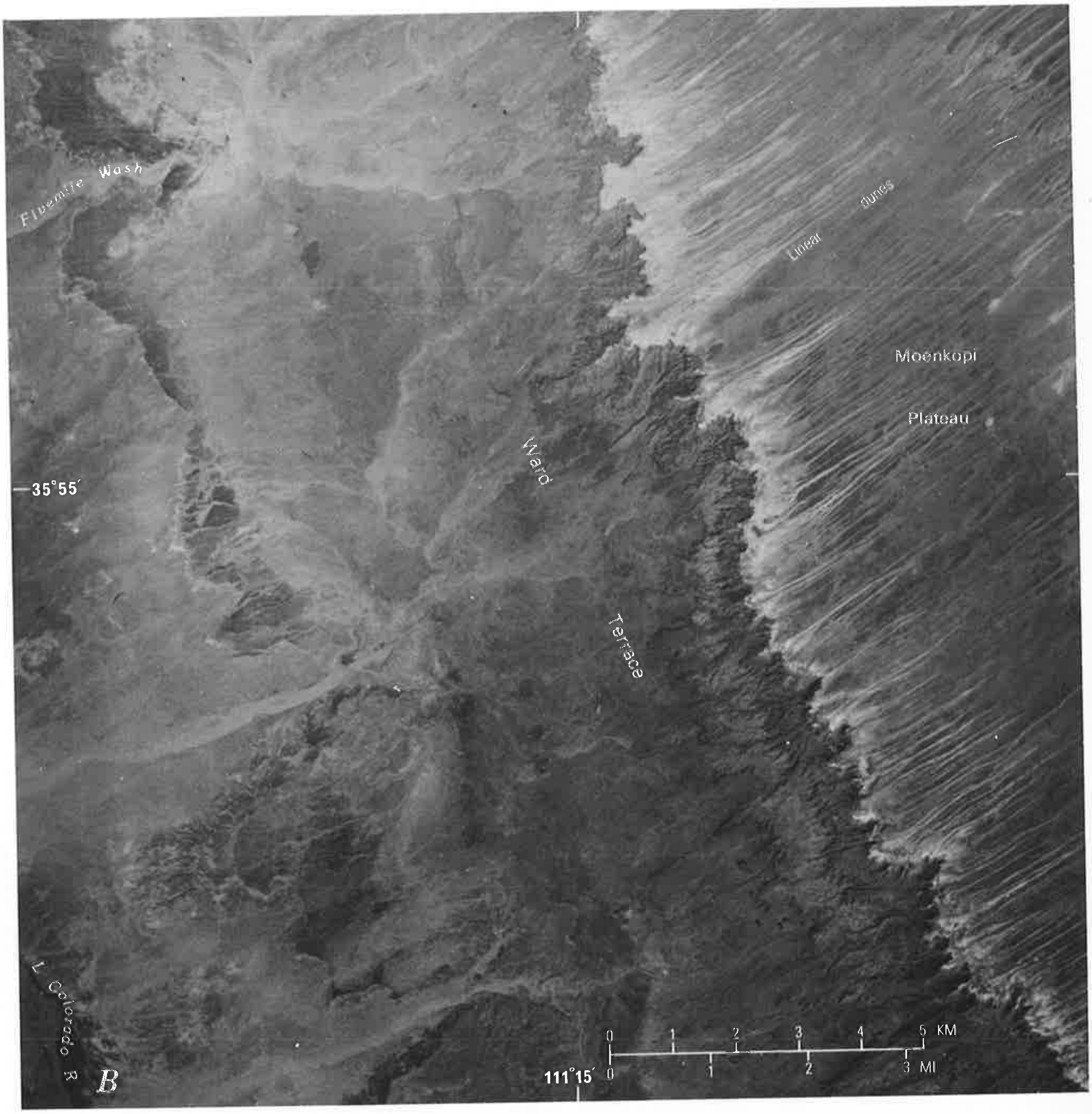

Plate 9. Simple linear dunes from the Navajo Indian Reservation, northern Arizona, U.S.A. (From BREED and GROW, 1979).

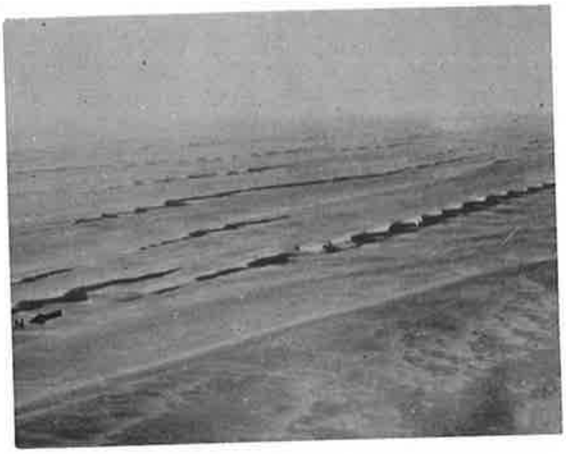

Plate 10. Linear dunes "with barchan-like slip faces developed on their western flanks as a result of gentle eastern winter winds. Central Wahiba Sands, Oman." (From GLENNIE, 1970.)

Plate 11. Snow barchans of the Lake Erie shore linked by the elongation of one of the horns of the windward barchan. (From HANNES and HANNES, 1982).

Plate 12. Linear dunes emerging from the leeward side of a transverse debris mound on the periphery of a dried lake bed. Many of the closely spaced dunes combine a short distance to leeward of the mound, thereby imposing greater order in the system away from the mound. This is most apparent on the right-hand side of the image. Note that in the image the dunes darken rapidly away from the debris mound. In nature this corresponds to a relatively abrupt transition in the dune from white to red sand.

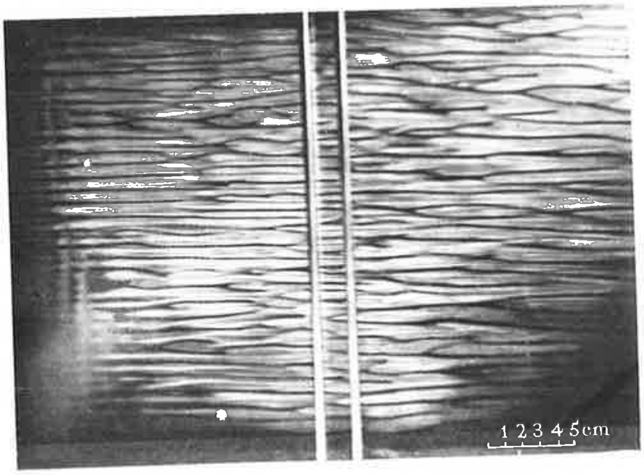

Plate 13. Smoke-marked roll vortices in a thin chamber in which shear is provided by the movement of a glass cover. The convection layer is 6 mm thick, the temperature difference between the top and bottom of the layer is 91°, and the shear is 2.3 cm/s. (From CHANDRA, 1938).

Plate 14. Rotation canister set up for photography. (From HORST, 1970b).

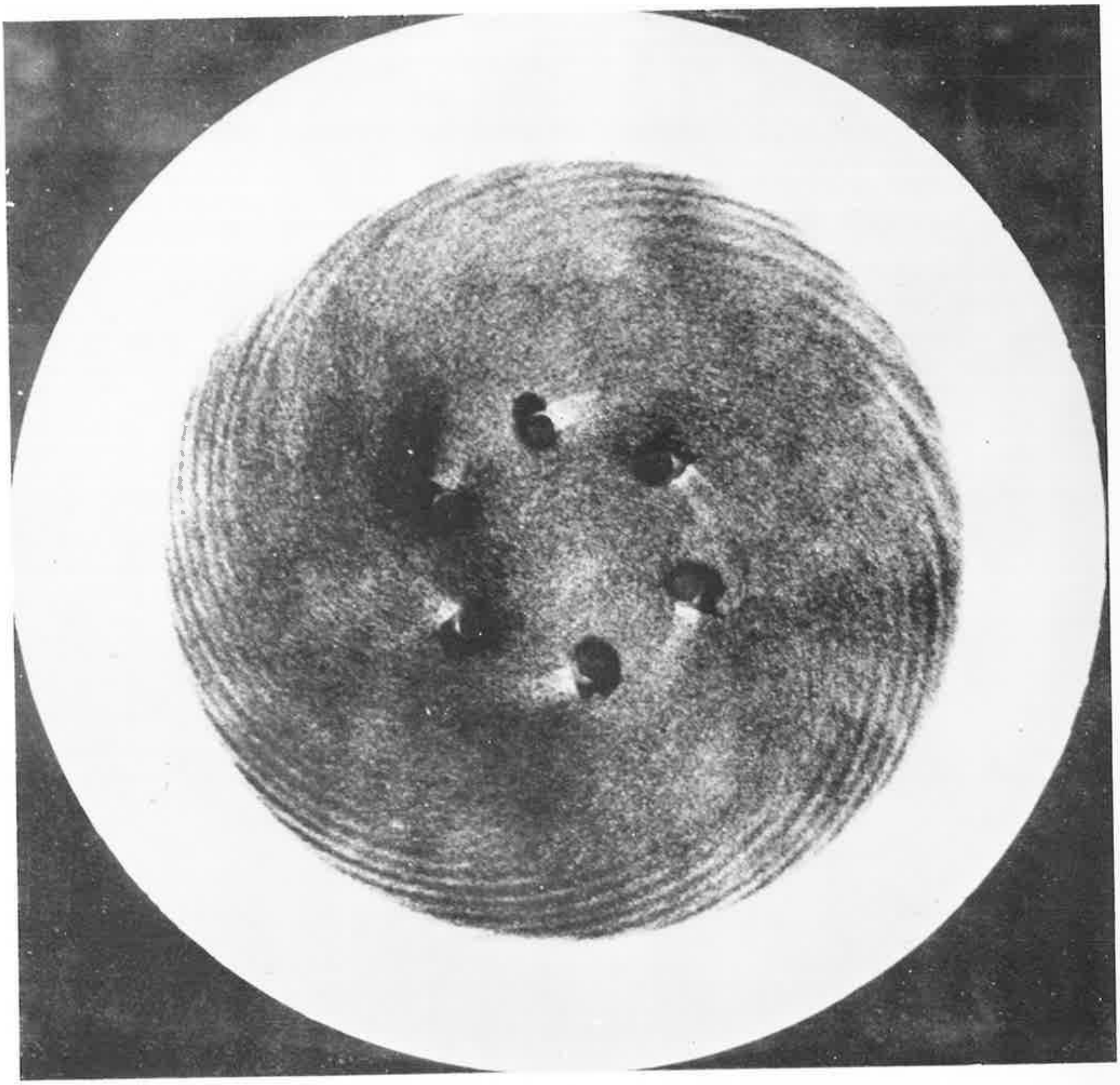

Plate 15. "China-clay record of instability." The direction of disk rotation was counterclockwise, the rotation rate was 3200 rev/min and the disk radius was 4.35 in. (From GREGORY, STUART and WALKER, 1955).

Plate 16. Longitudinal features developed on the bottom sand bed the rotation canister. (From HORST, 1970b).

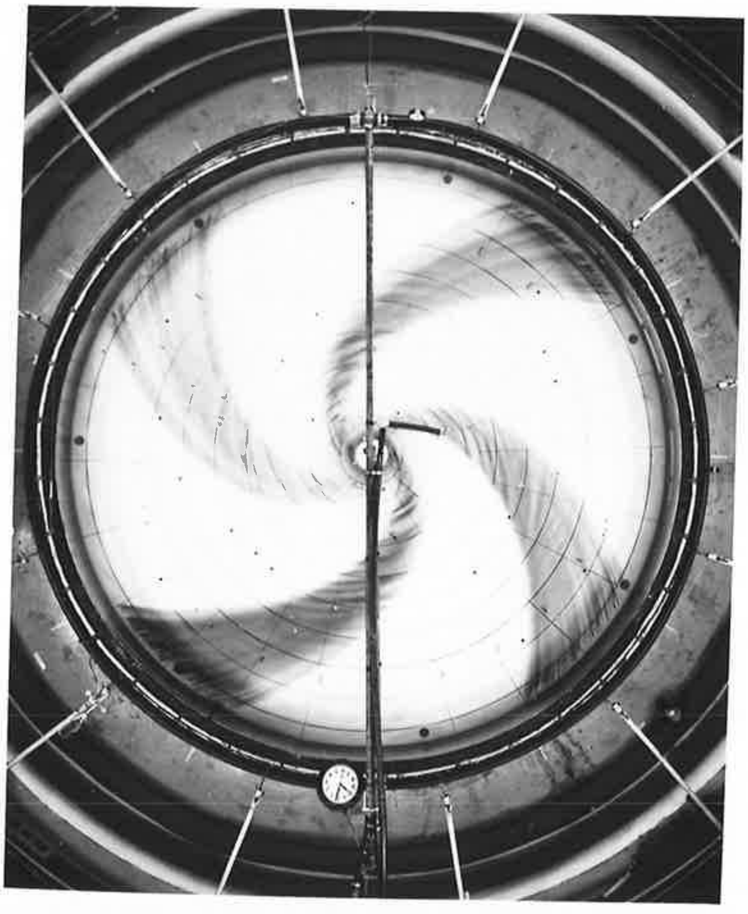

Plate 17. Stationary vortices produced in a rotation tank while fluid was moved radially across the bottom. (From FALLER and KAYLOR, 1966).

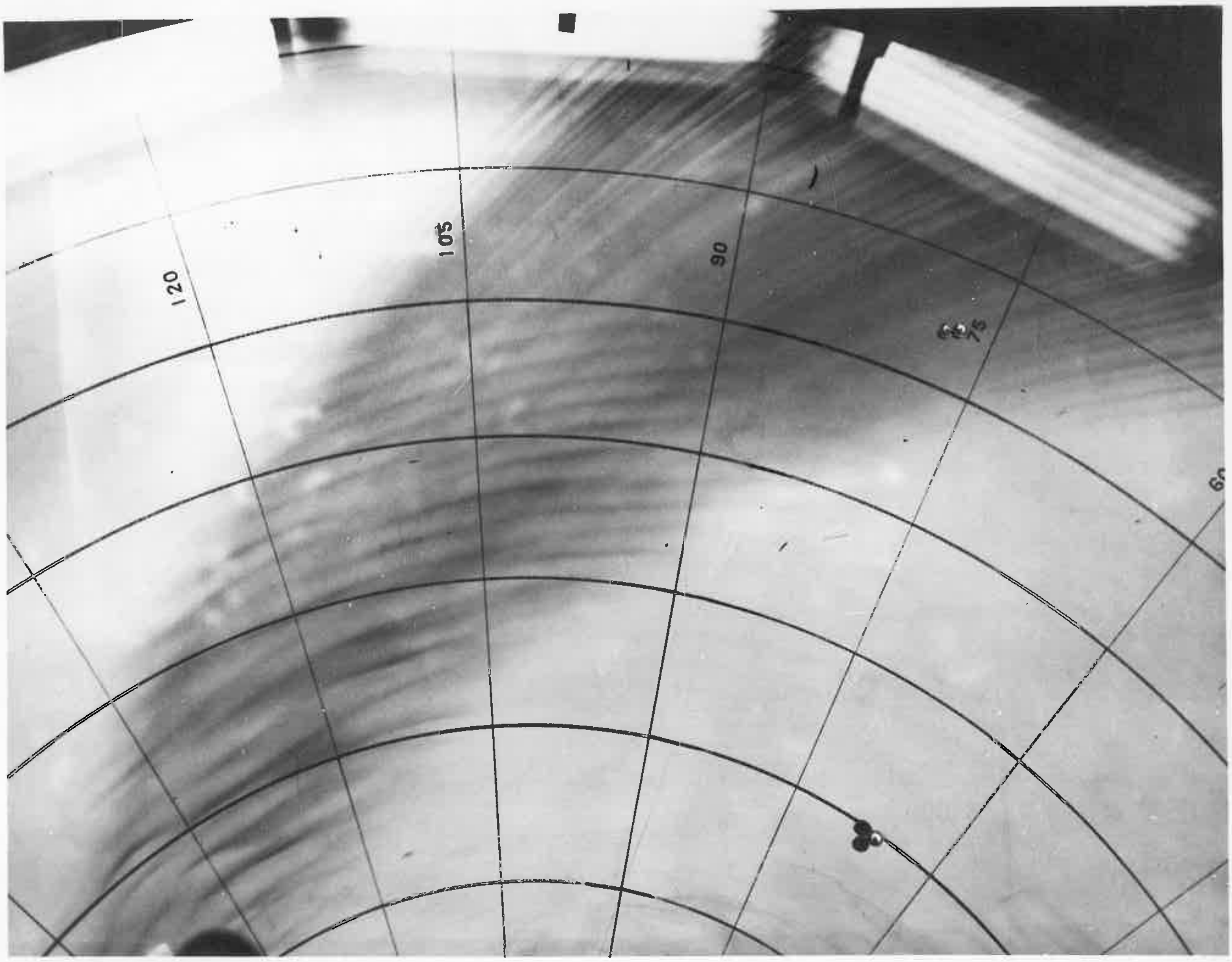

Plate 18. Isolated rotation tank vortice (see Pl. 17). (From FALLER and KAYLOR, 1966).

Plate 19. Longitudinal features in bottom sand bed of the rotation canister. Note that in this instance only the fluid near the fringe of the canister seems to have succombed to an organized instability. (From HORST, 1970b).

Plate 20. Notched linear dunes of northern Africa. Note that secondary ridges are nearly orthogonal and extend to the left of the primary linear dunes. (From CLOS-ARCEDUC, 1968).

Plate 21. Notched linear dune of central Australia. Here the secondary ridges extend to the right of the primary dune. If notched dunes do result from transverse roll vortices, which are secondary to longitudinal roll vortices, then it would be expected that secondary ridges produced would be to the left of the primary dune in the northern hemisphere and to the right of the primary dune in the southern hemisphere. (C. R. Twidale).

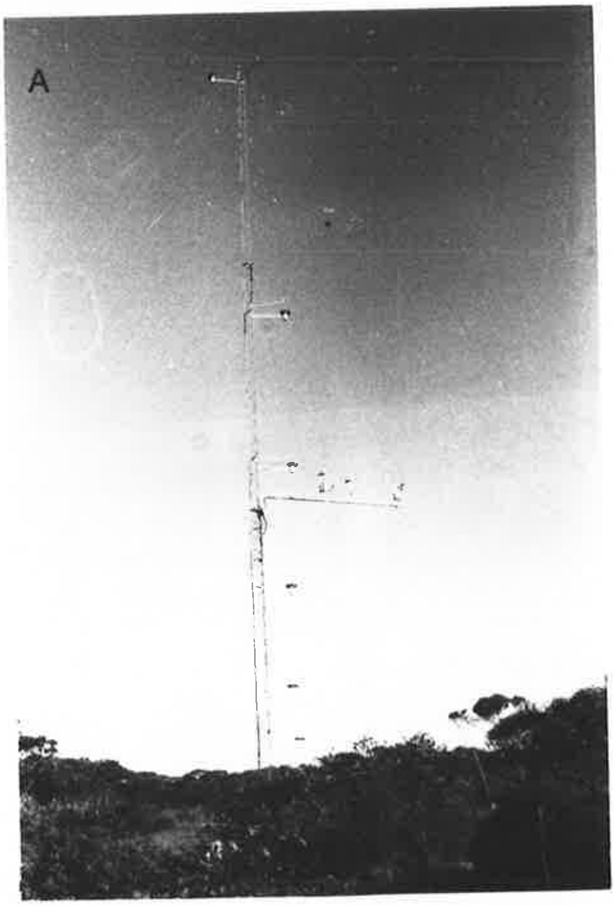

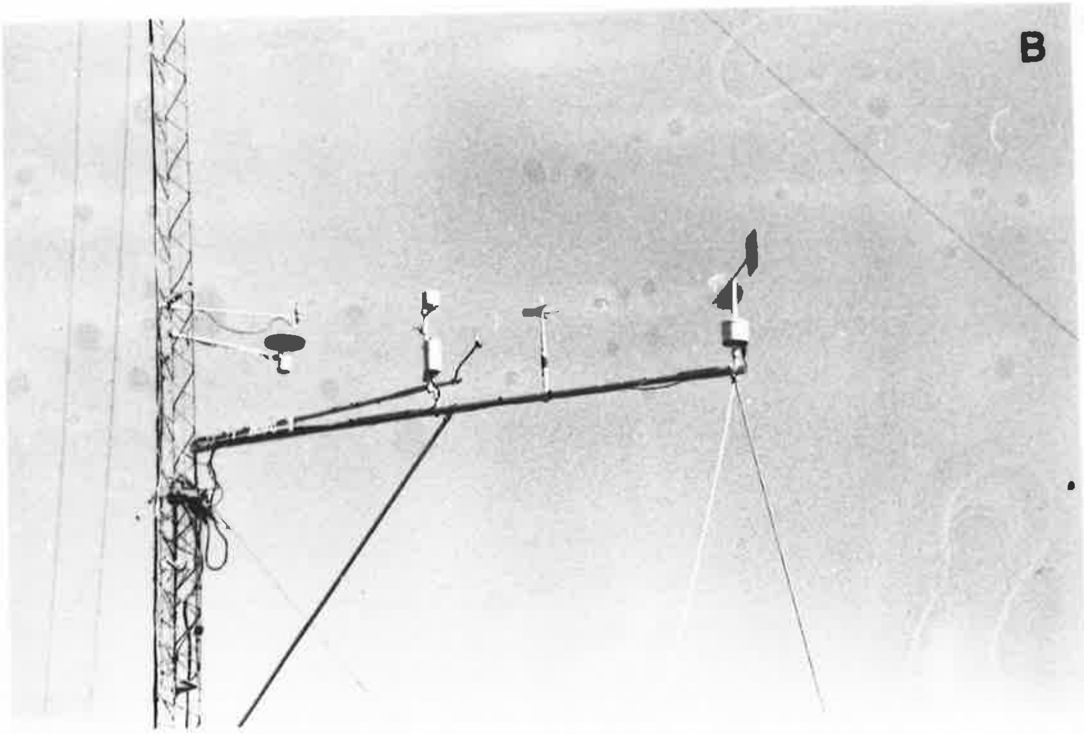

Plate 22. A) 100 m tower instrumented for the observation of turbulant eddies over the low canopy of a forest in central Eyre Penninsula, South Australia. Note that the pairs of short extension arms, mounted with a cup anemometer and a shielded temperature sensor, are logarithmically spaced. This is configuration is prompted by the logarithmic vertical variation in wind speed and temperature. B) Long horizontal boom mounted with, from right to left, wind vane and propellor anemometer, vertical wind component rotor anemometer, and hygrometer. The encasement for the thermometer mounted on the short arm, of which a clearer view is afforded in this image, is designed to shield the sensor from direct solar radiation and wind. (Chen Fa Zu, Chinese Academy of Science).

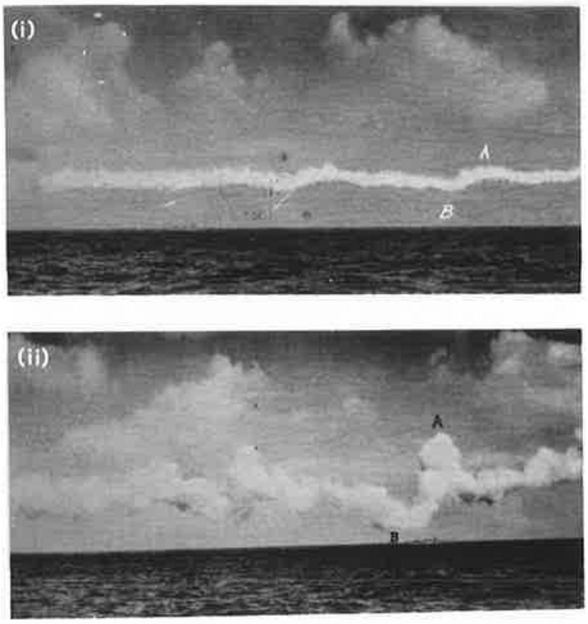

Plate 23. "Smoke laid parallel to the wind by a plane flying horizontally. Note the vertical development of points A and B. Elapsed time between (i) and (ii) is 88 seconds." (Taken from WOODCOCK and WYMAN, 1947).

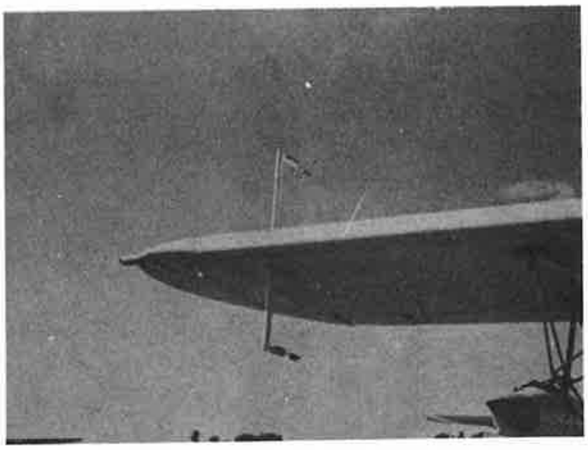

Plate 24. "Installation of potential gradient probes on wing of Tripacer aircraft." (From VONNEGUT, MOORE and MALLAHAN, 1961).

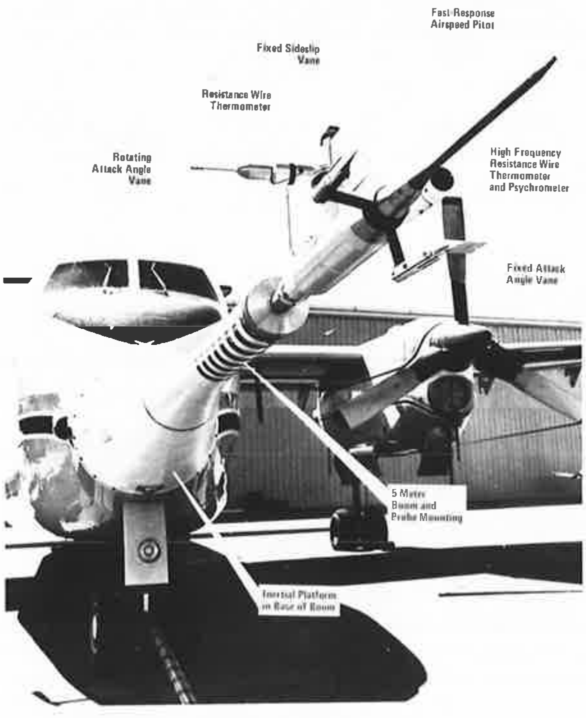

Plate 25. The instrumented foremast or noseboom of the de Havilland Buffalo aircraft N326D of the National Center for Atmospheric Research (NCAR), Boulder, Colorado, U.S. (From LENSCHOW, 1972).

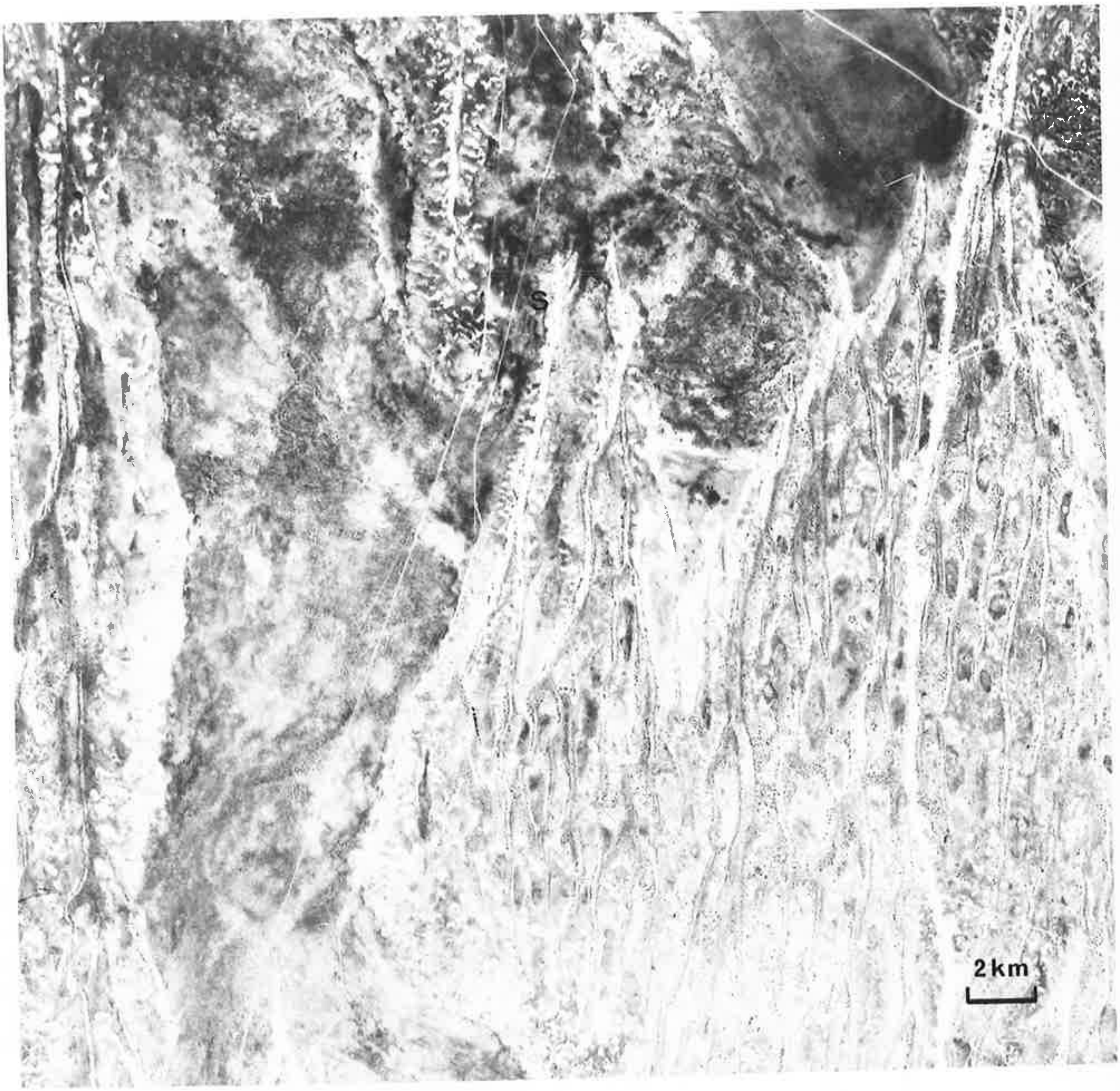

Plate 26. Landsat image of the area just to the south of Moomba gas camp. The study dune is marked "s". (Strzelecki 1:250,000 photograph, SVY. 2548, Department of Lands, South Australia).

Plate 27. Eastern flank of the study dune.

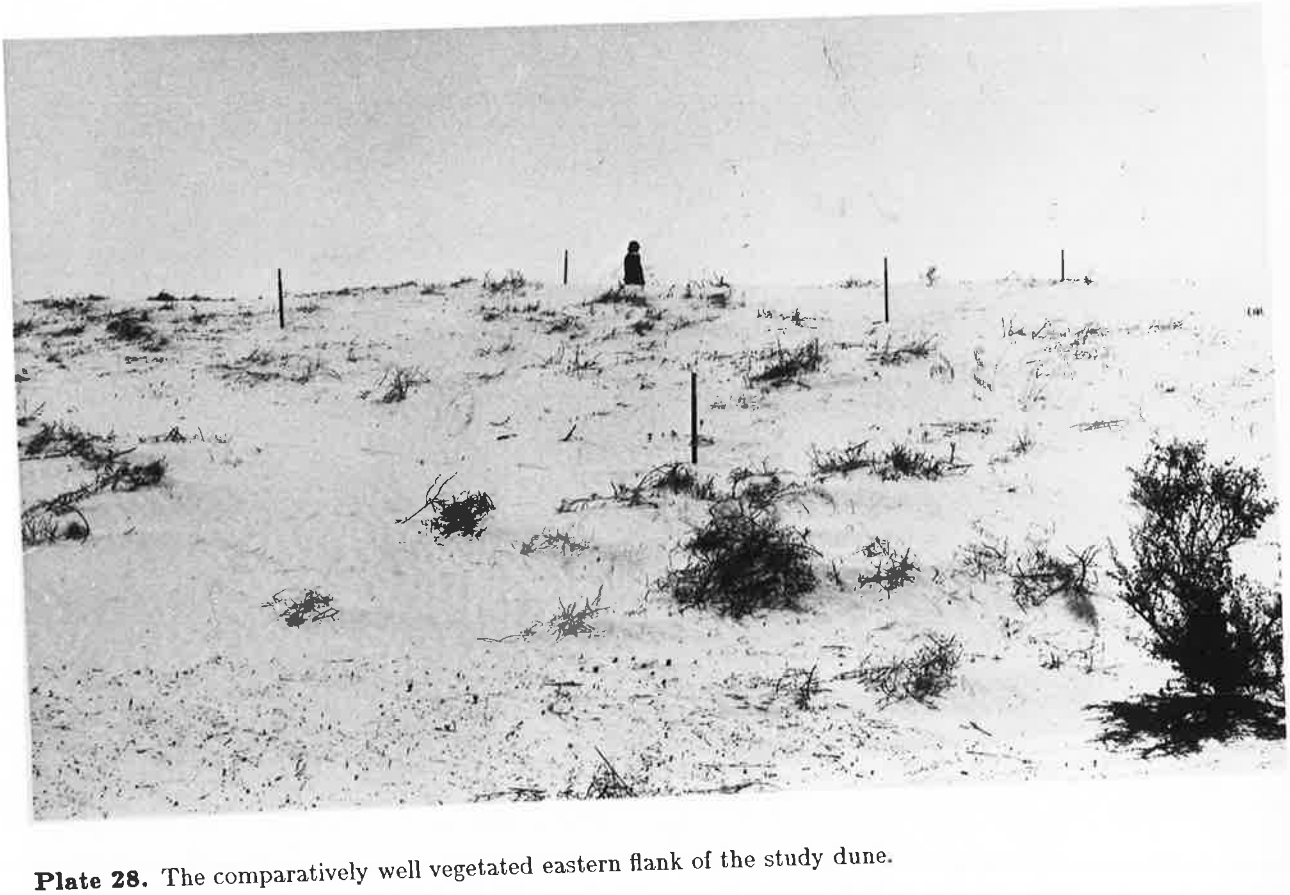

Plate 28. The comparatively well vegetated eastern flank of the study dune.

Plate 29. Study dune summits as viewed from the west.

Plate 30. Study dune summits as viewed from the crest looking south.

Plate 31. Ripples on the study dune surface as viewed looking south and into the wind.

Plate 32. A point along the western perimeter of the study dune at which the transition between the dune and the firm material of the interdune corridor is abrupt.

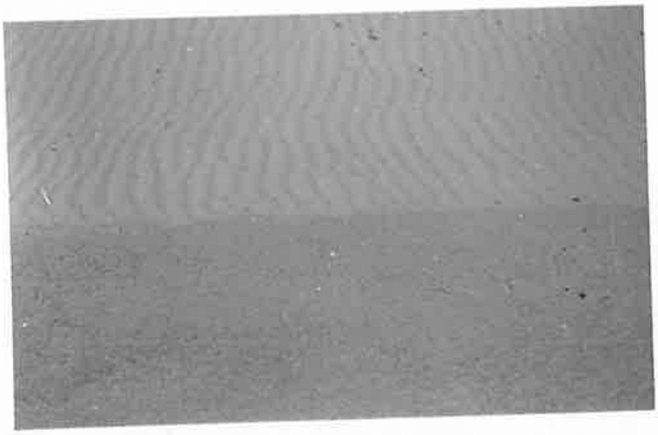

Plate 33. A close-up view of the transition between the dune and the interdune corridor (See Pl. 32).

Plate 34. A point along the western perimeter of the study dune at which exists an intermediate stage of gently sloping, rippled sand between the main body of the dune and the interdune corridor.

Plate 35. "Clay leave,"erosional structures just beyond the eastern perimeter of the study dune.

Plate 36. Interdune corridor area to the west of the study dune consisting mainly of low vegetation.

Plate 37. Grassy interdune area to the east of the study dune.

Plate 38. Sandy interdune corridor area just to the west of the study site with a very sparse population of low vegetation.

Plate 39. Pebbly interdune corridor area to the west of the study dune with some low, woody debris.

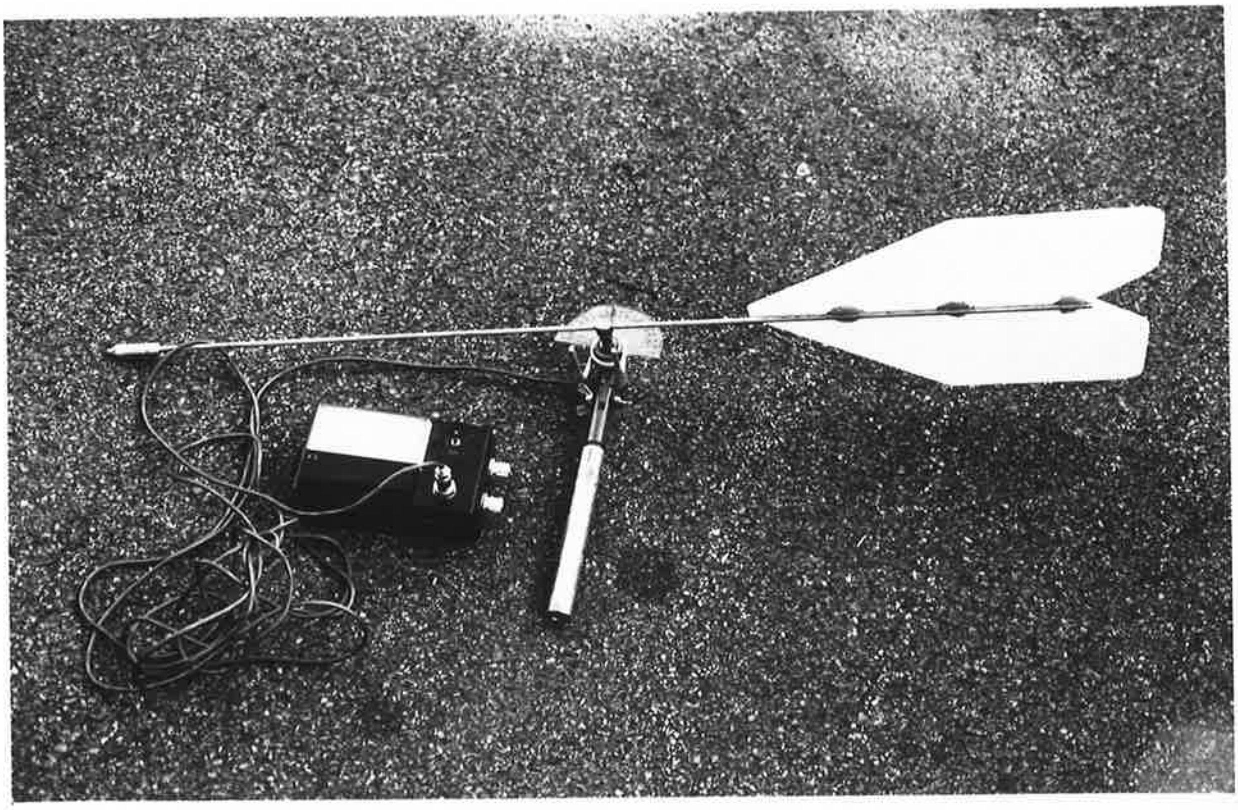

Plate 40. Variable resistance wind vane utilizing a styrofoam tail and a DC 100 microampere meter.

Plate 41. Electronic wind vane mounted on top of a ~ 2.5 m wooden pole for measurements.

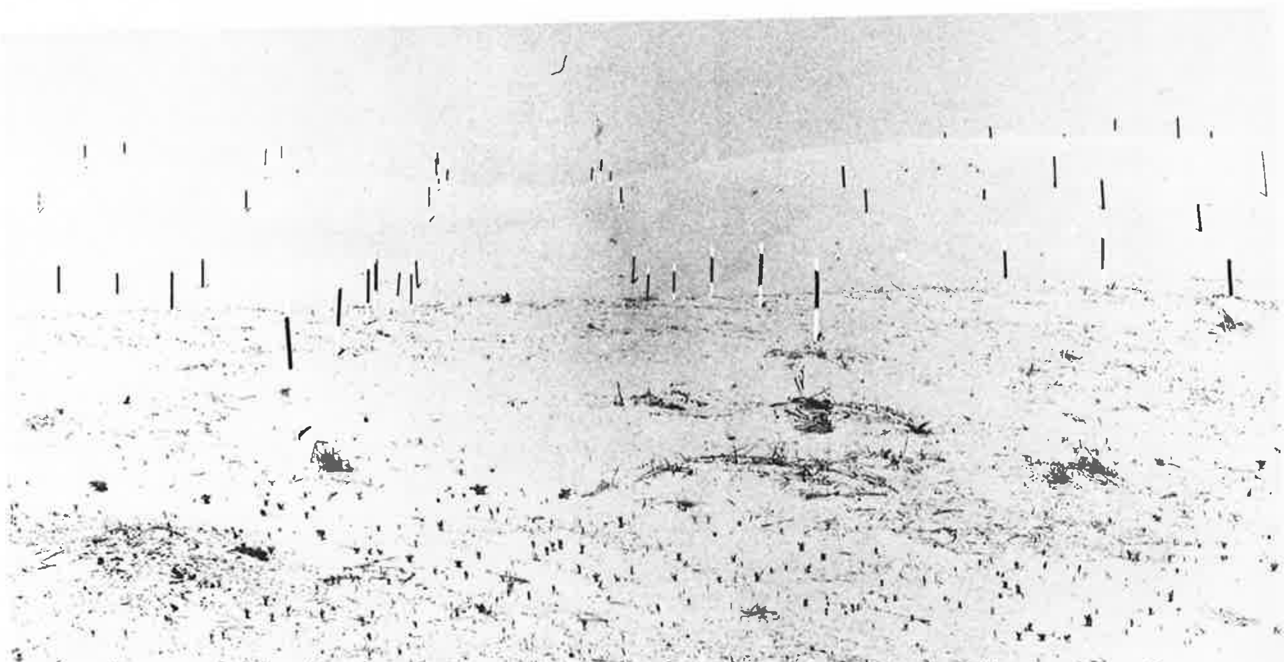

Plate 42. Grid of stakes planted over the study site for use in deposition/erosion monitoring.

Plate 43. Tracking theodolite and balloons before launching close to the western perimeter of the study dune.

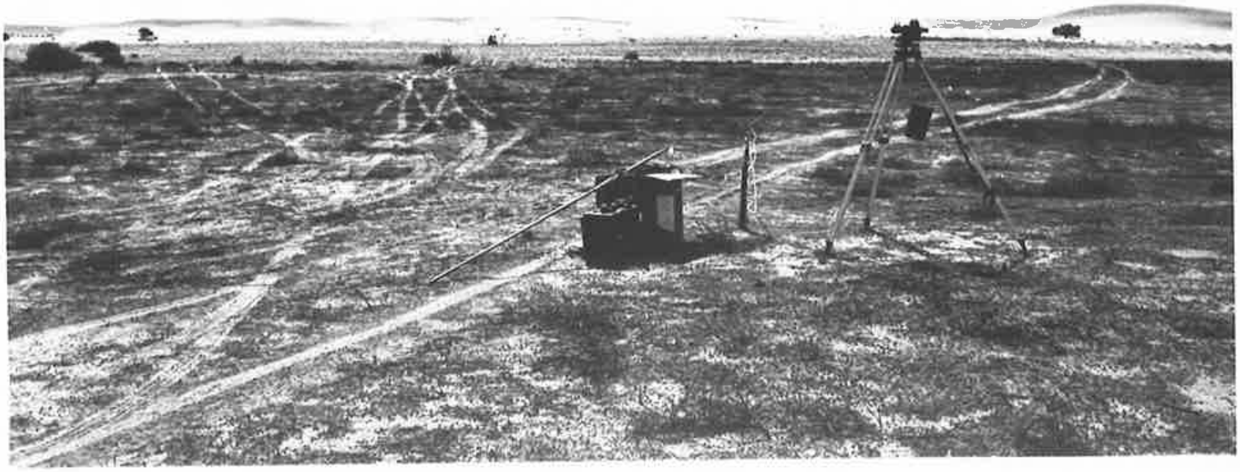

Plate 44. Tracking theodolite ~ 200 m west of the dune.

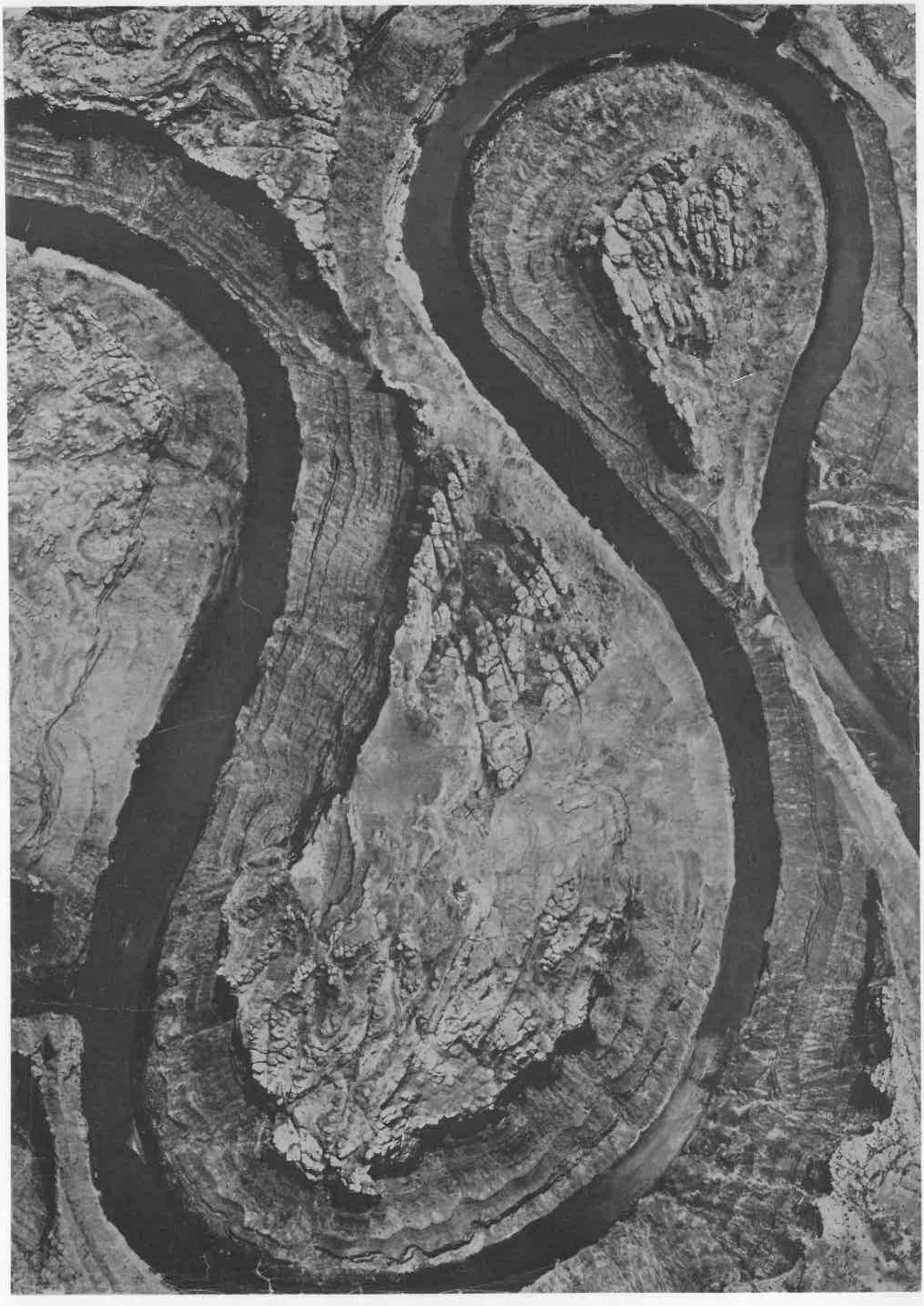

Plate 45. Meander in the Colorado River, Southern Utah, as seen from an altitude of ~ 3000 m. (From LEOPOLD and LANGBEIN, 1966).

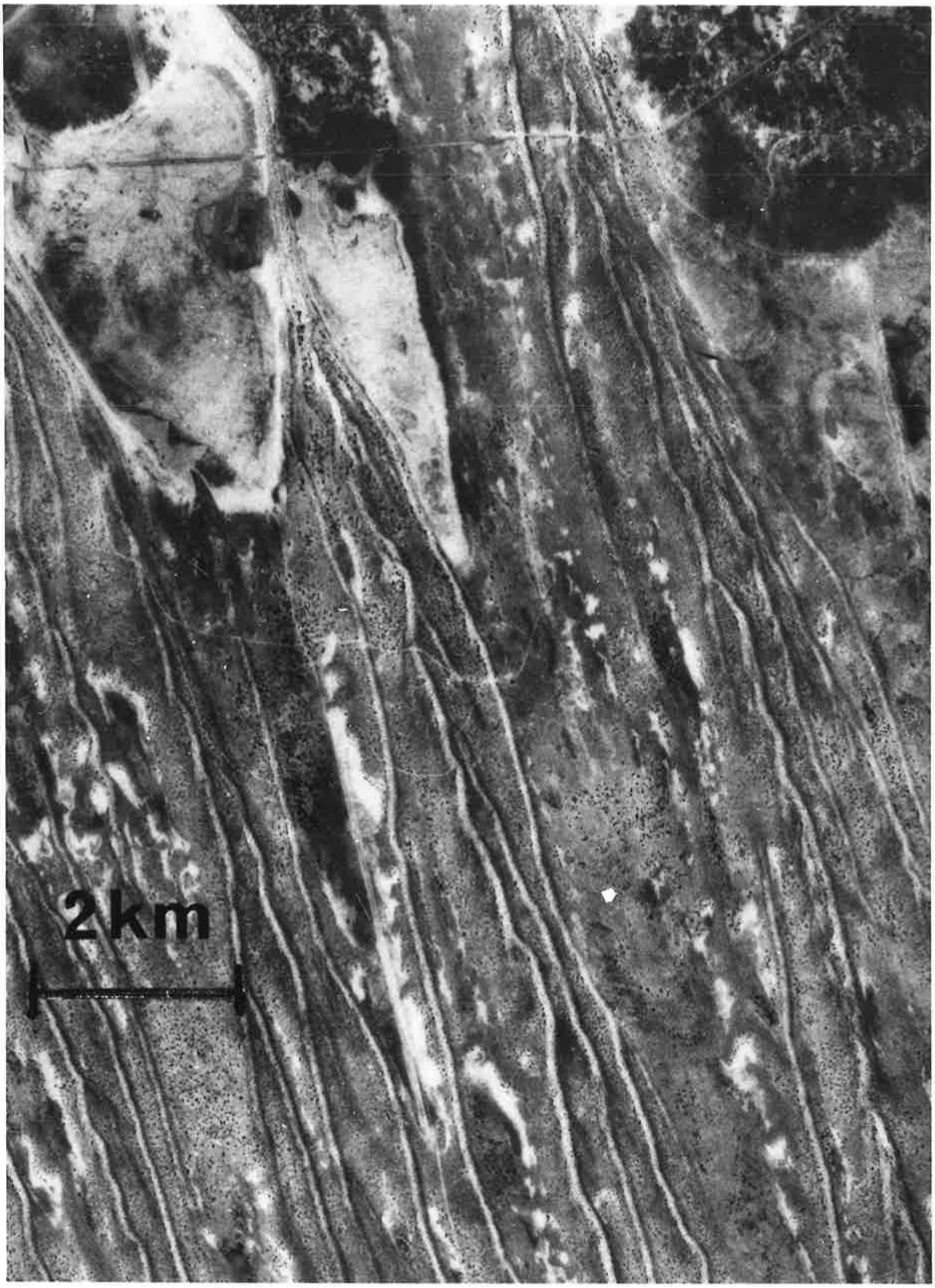

Plate 46. Several examples of dunes that converge but do not coalesce can be found in this image, most notably the three convergent dunes in the center. (Gason 1:250,000 photograph, SVY. 2473, Department of Lands, South Australia.)

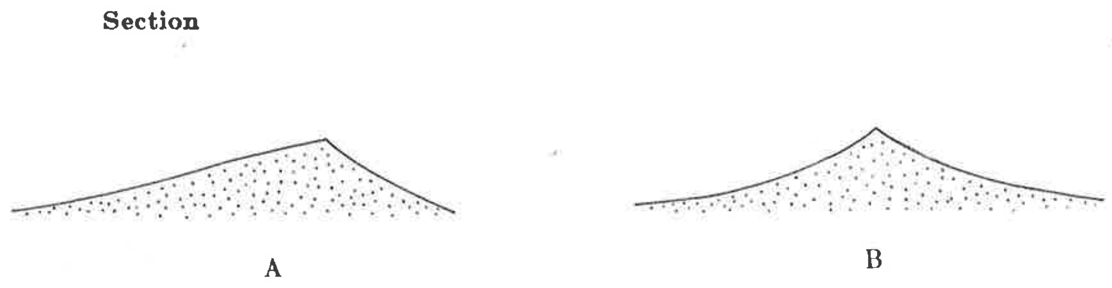

Figure 1. A) Section through a typical longitudinal dune. B) Section through the sharp-crested longitudinal dunes found in the vicinity of Qinghai, central China.

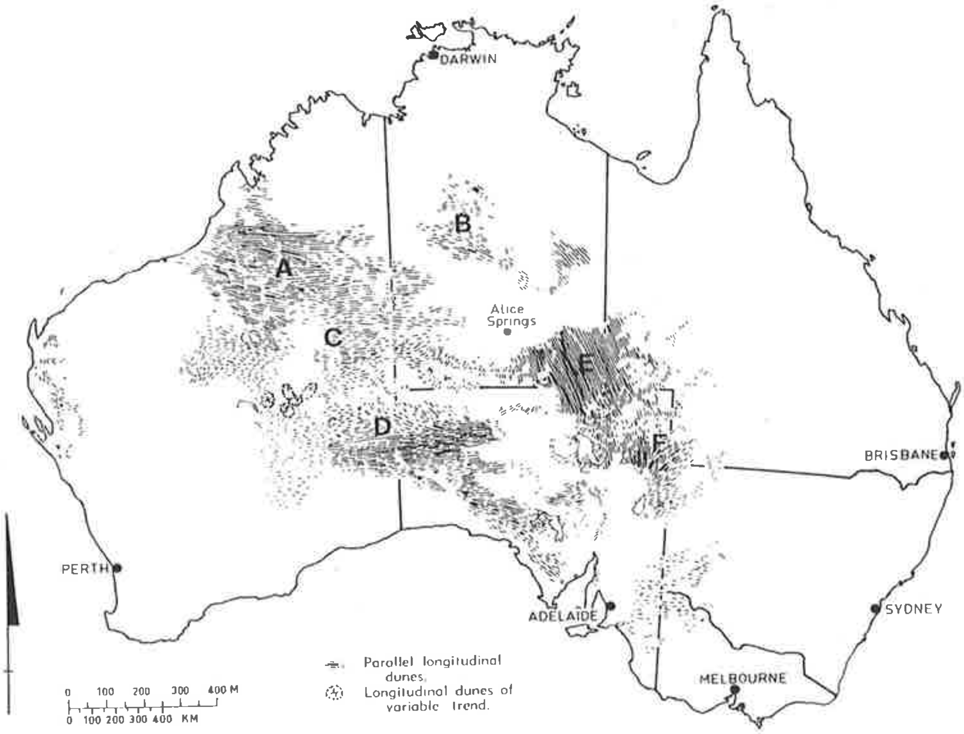

A Great Sandy Desert
B Tanami Desert
C Gibson Desert
D Great Victoria Desert
E Simpson Desert
F Sturt's Stony Desert

[TWIDALE, 1981]

Figure 2. The continental system of Australian linear dune fields.

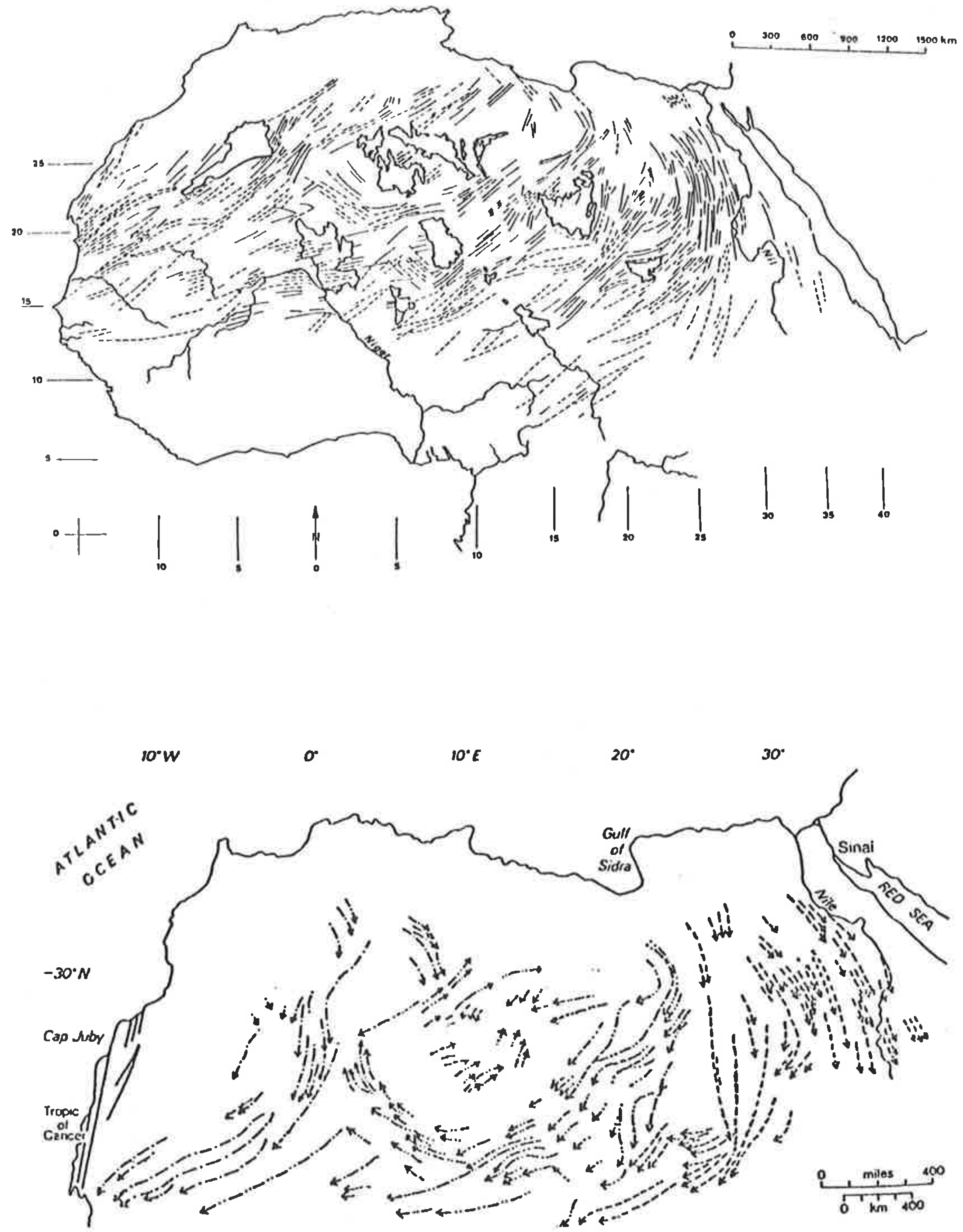

Figure 3. A) Saharan and Sahelian linear deposition and deflation feature patterns as derived from satellite data. Dashed lines represent what are presumably deposition features, and solid lines represent what are presumably deflation features. B) Saharan wind patterns based on satellite data.

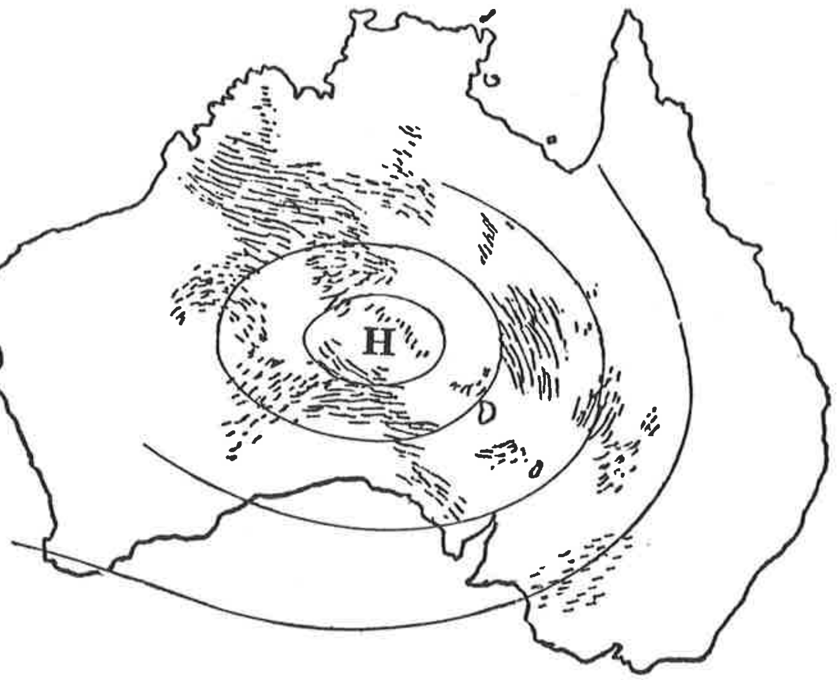

Figure 4. The Australian continental arc of relict linear dunes and an approximation of the mean trace of ancient summer anticyclones (surface high pressure systems).

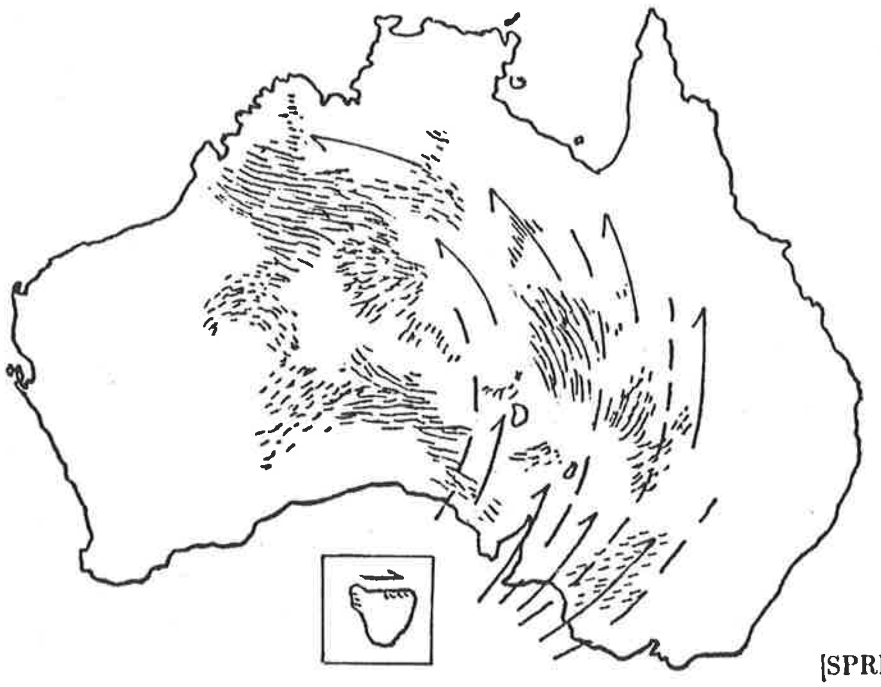

[SPRIGG, 1980]

Figure 5. Prevailing winds of the modern summer anticyclone.

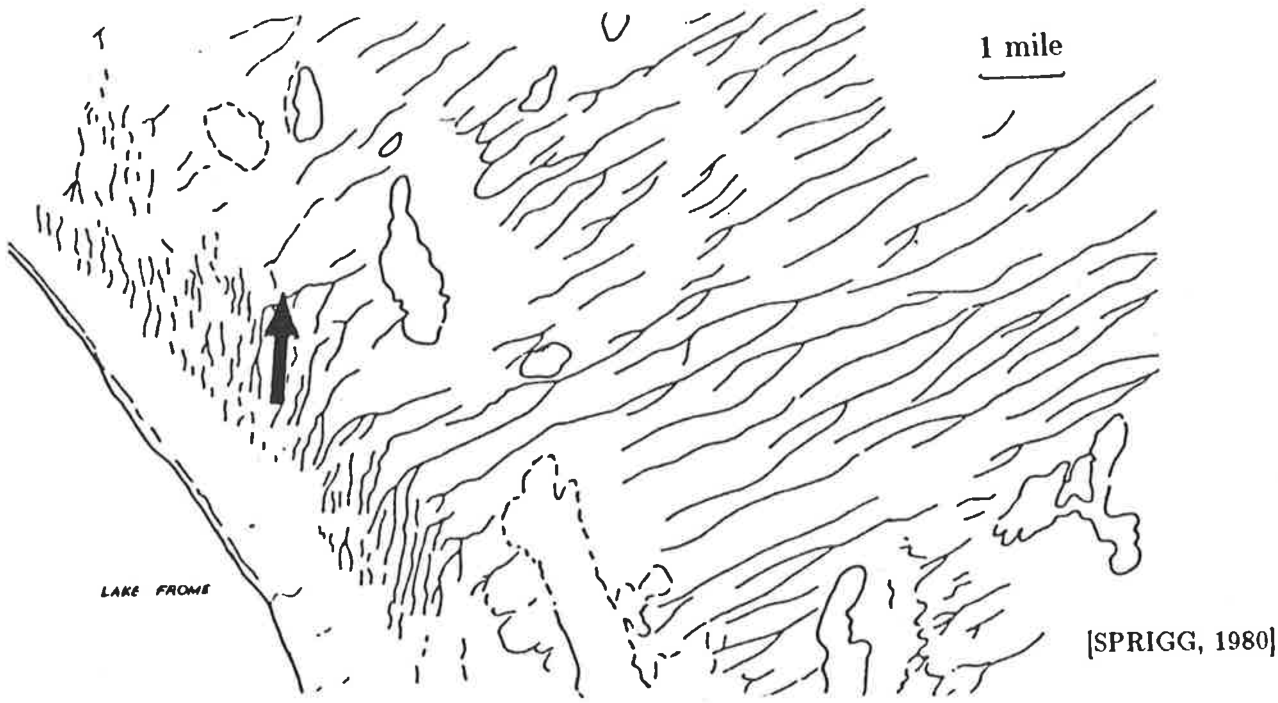

Figure 6. Present prevailing winds, as indicated by the thick arrow, freshly forming longitudinal dunes on the northeastern shore of Lake Frome. The forming dunes are greatly divergent from the preexisting ones.

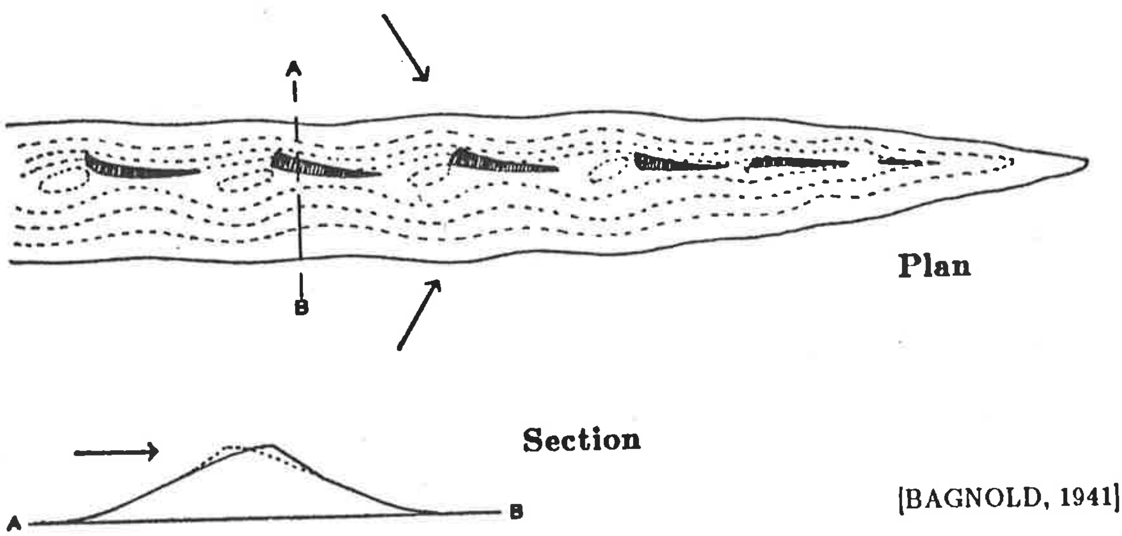

Figure 7. Longitudinal dune with shifting crest. Arrows are storm wind vectors.

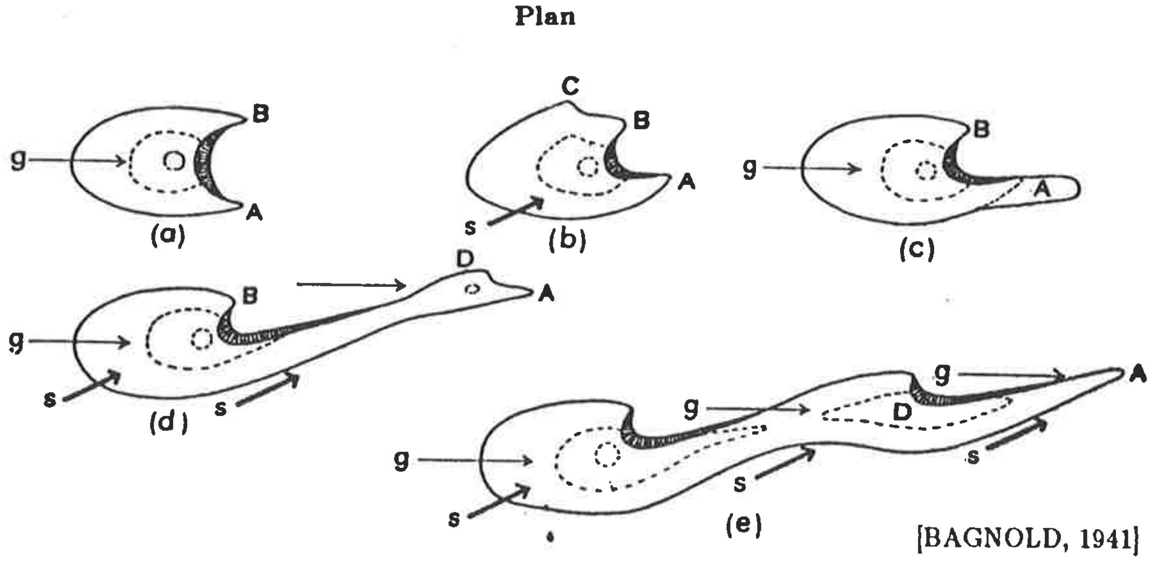

Figure 8. Transition from barchan to linear dune as a result of bidirectional winds.

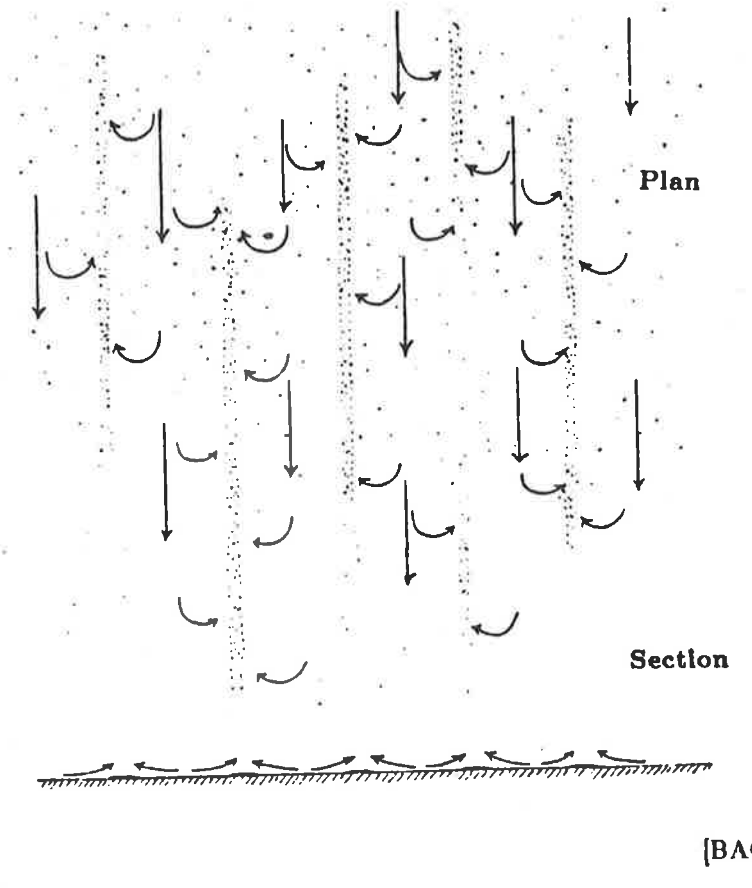

Figure 9. Strips of fine sand deposited during a storm and the hypothetical secondary circulation.

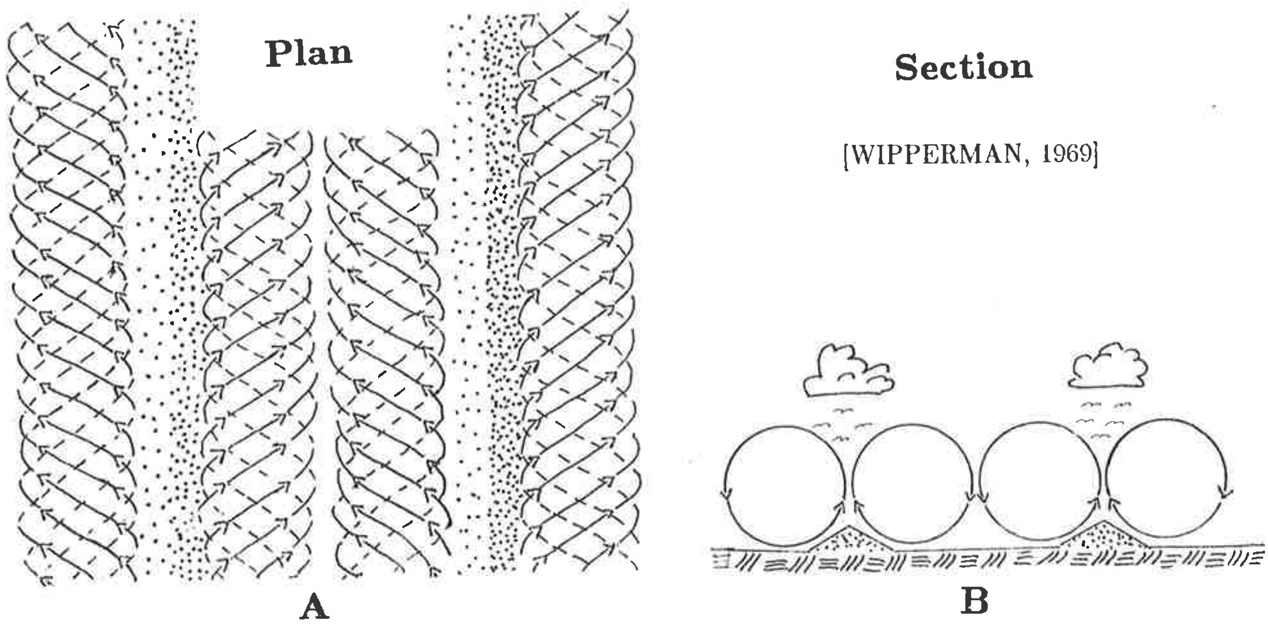

Figure 10. A) Roll vortices and longitudinal dunes. B) Roll vortices, longitudinal dunes, soaring birds and longitudinal clouds or cloudstreets.

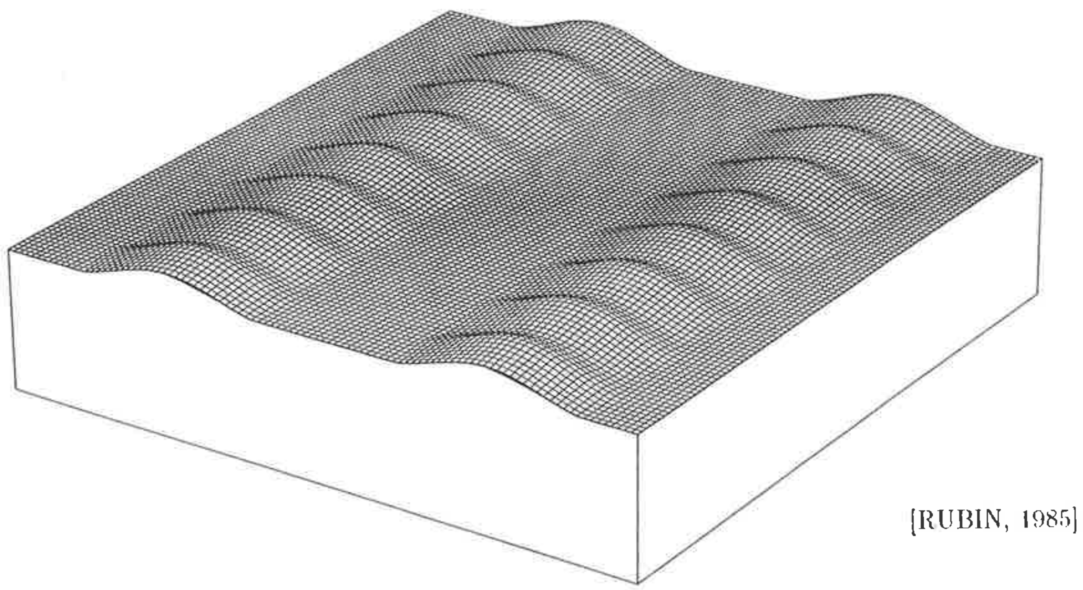

Figure 11a. Laterally stationary windrift-type linear dunes. Here dunes are presumably aligned with mean sediment transport.

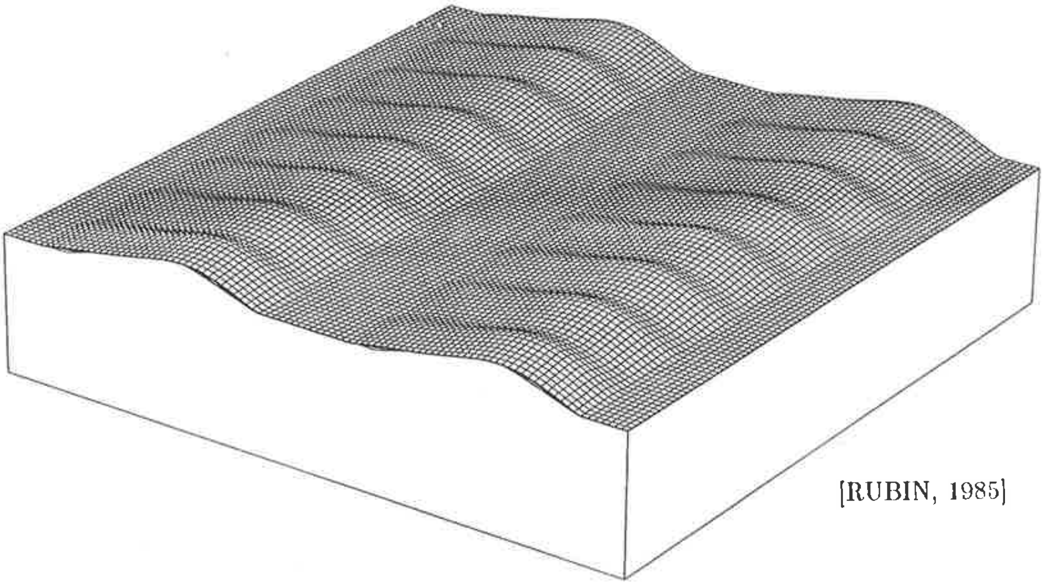

Figure 11b. Linear dunes that cause downward scouring during lateral migration. Dunes are not aligned with mean sediment transport.

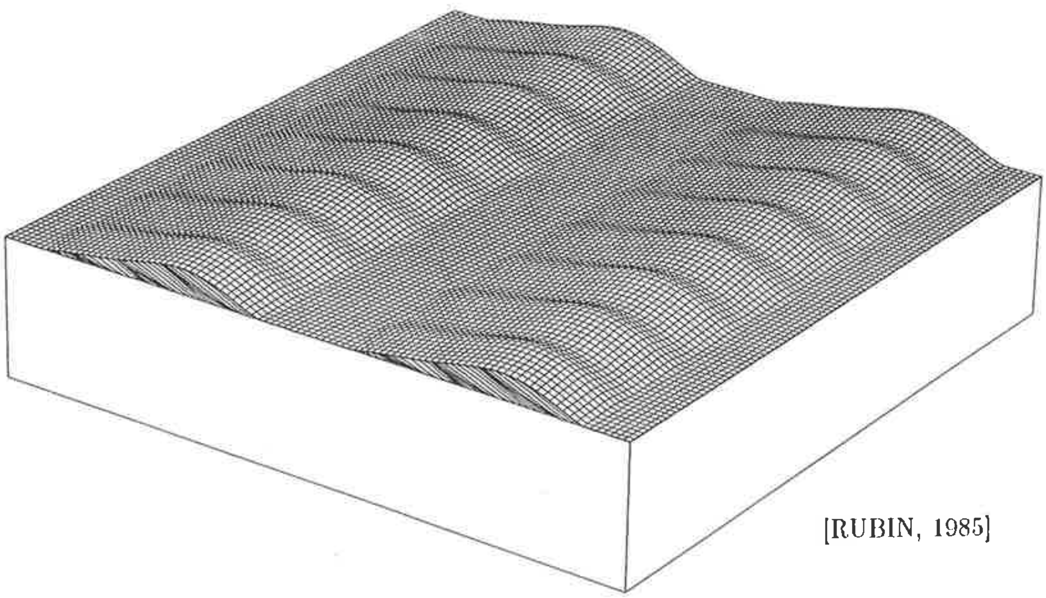

Figure 11c. Linear dunes that neither scour or climb during lateral migration.

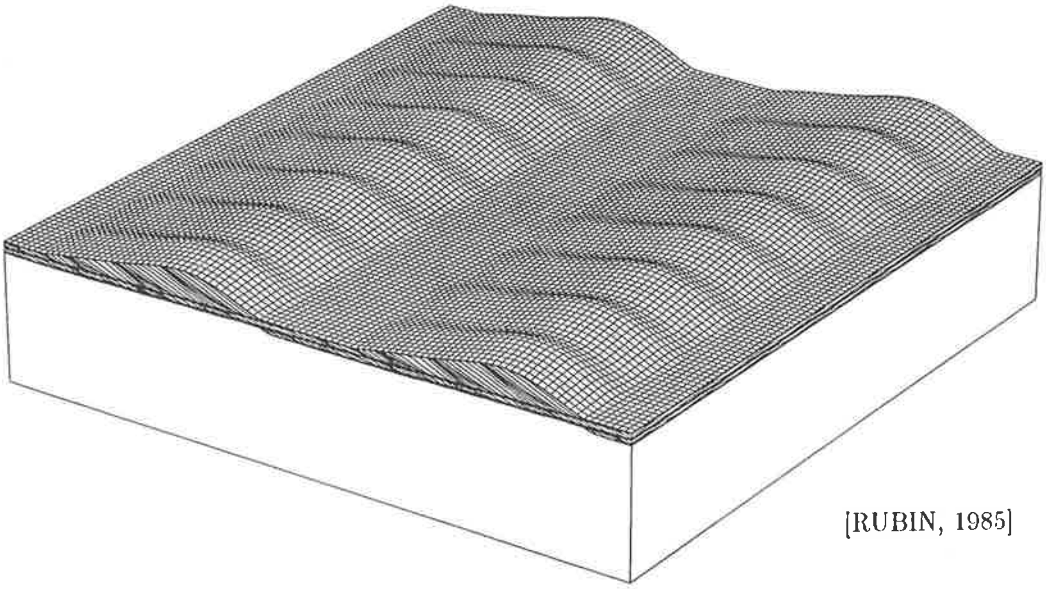

Figure 11d. Linear dunes that climb at a slight angle during lateral migration.

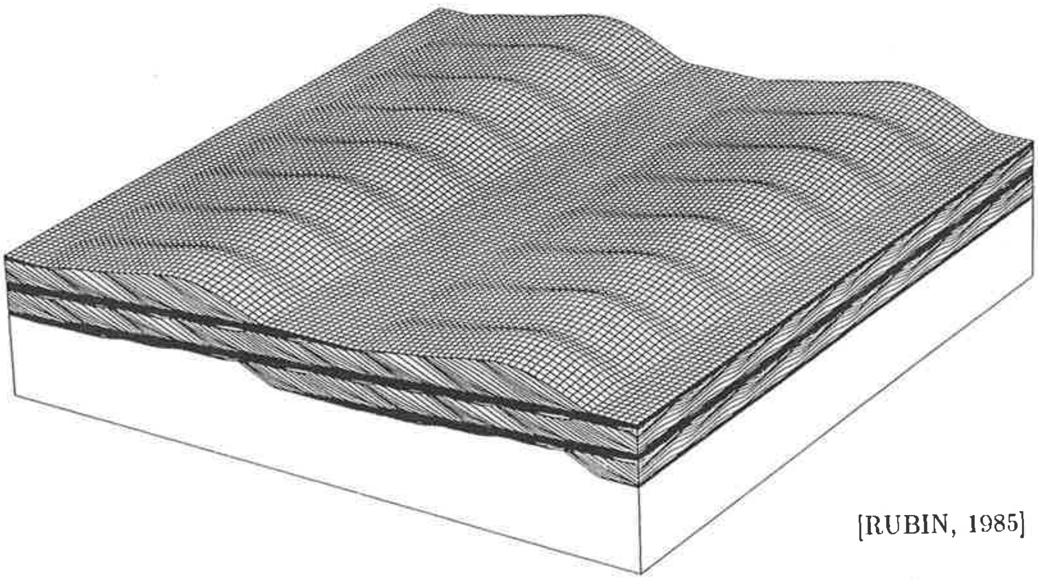

Figure 11e. Linear dunes that climb at a substantial angle during lateral migration

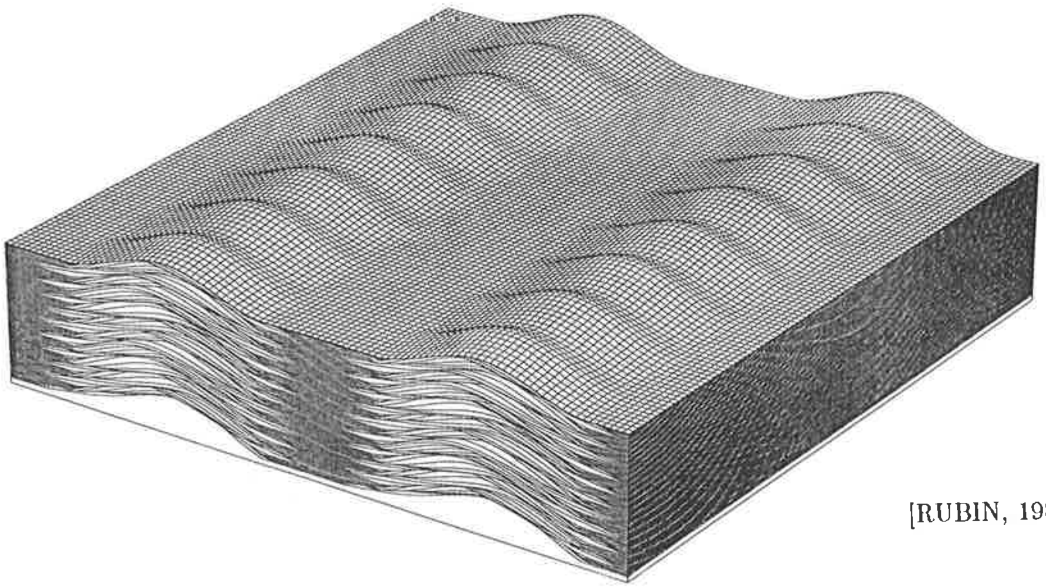

[RUBIN, 1985]

Figure 11f. Linear dunes "that accrete vertically without migrating laterally." Here dunes are either aligned with sediment transport, or deposition rate is unusually high.

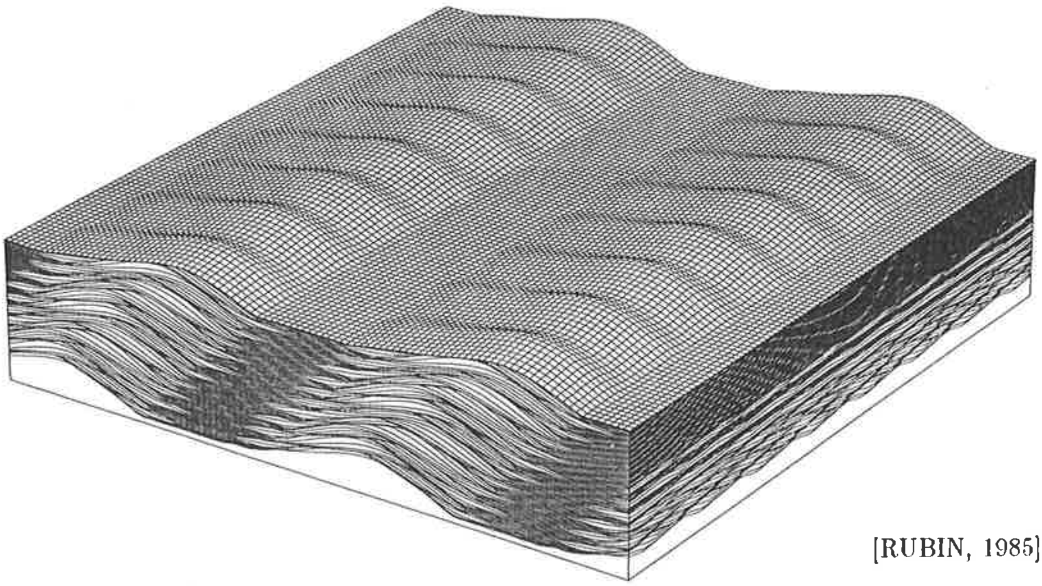

[RUBIN, 1985]

Figure 11g. Linear dunes that both accrete vertically and migrate laterally.

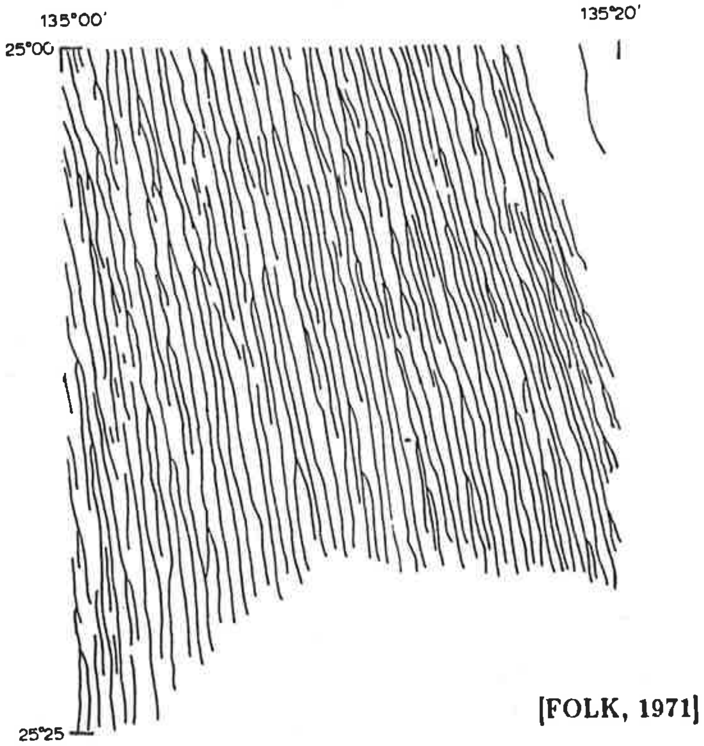

Figure 12. "Tracing of the northwest corner of McDill's topographic sheet, showing dune trends typical of the central Simpson desert. Observe the fantastic parallelism of the dunes, and the systematic opening of the tuning-fork junctures to the SSE. A count on the original map showed 81 out of 83 junctures opening to the south."

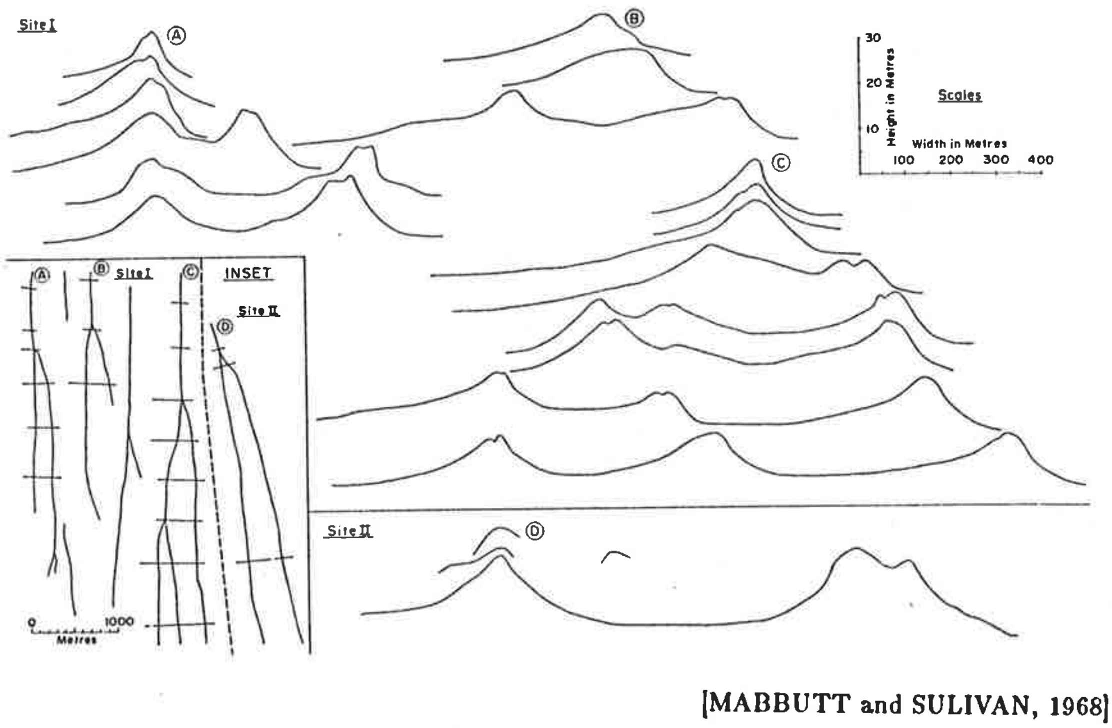

Figure 13. "Dune profiles in relation to junctions as shown inset."

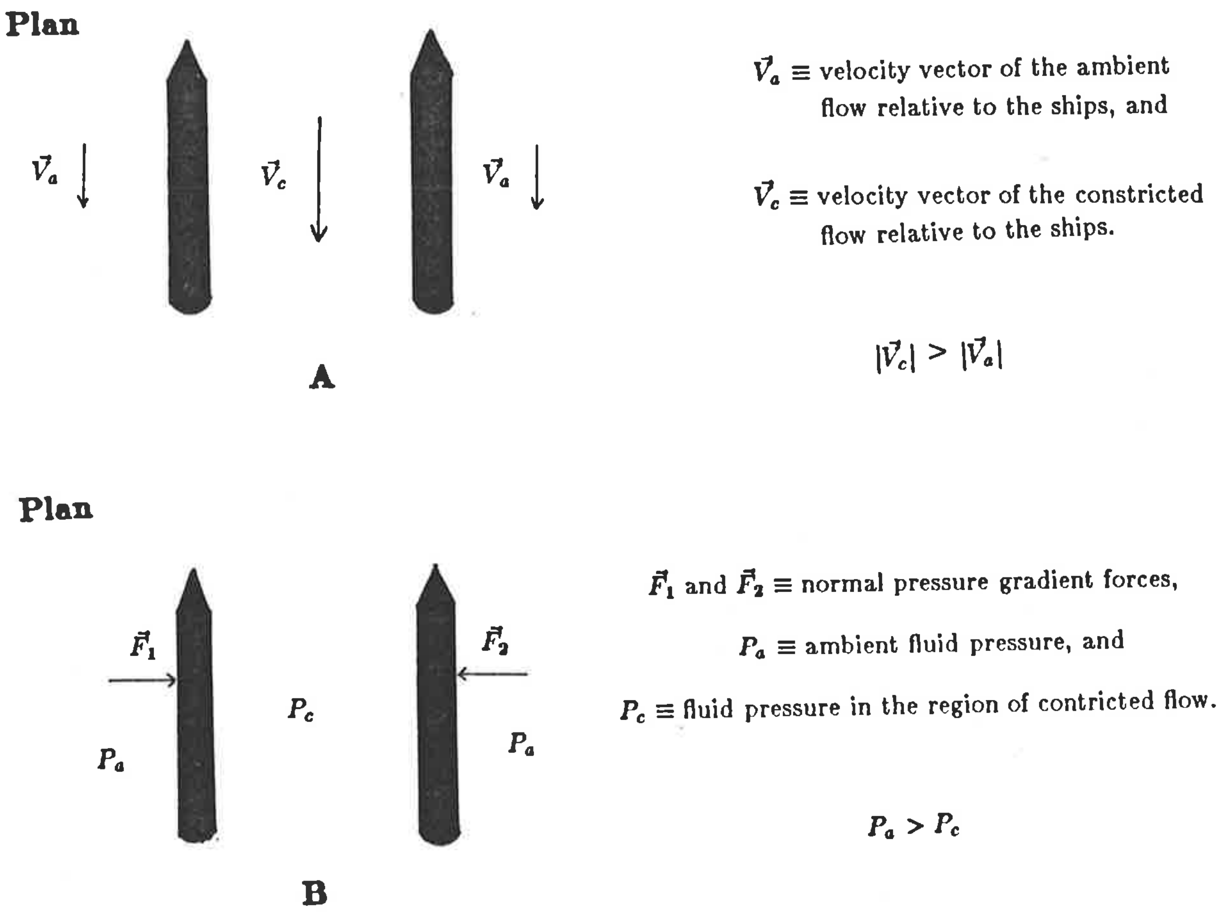

Figure 14. A) Flow around ships travelling in parallel. B) Pressure field and normal pressure gradient forces upon ships travelling in parallel.

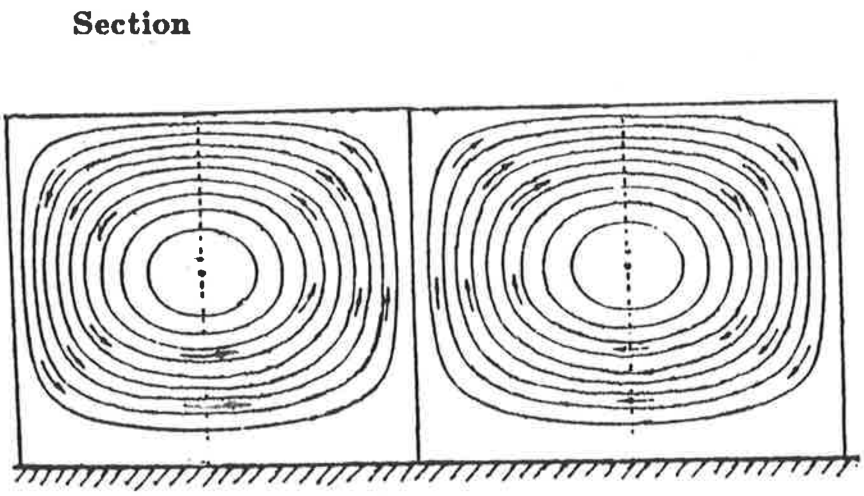

[BRUNT, 1951]

Figure 15. "Circulation in the Bénard convection cell."

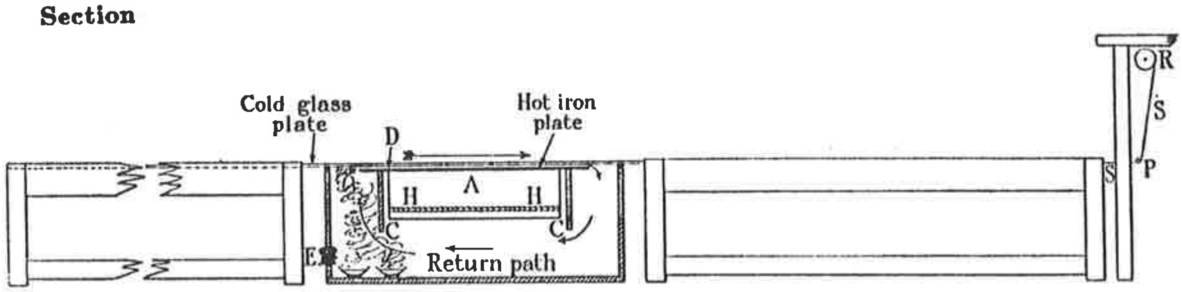

[GRAHAM, 1933]

Figure 16. Smoke chamber for the observation of microscale roll vortices. The convective fluid layer is between the hot iron plate and the cold glass plate.

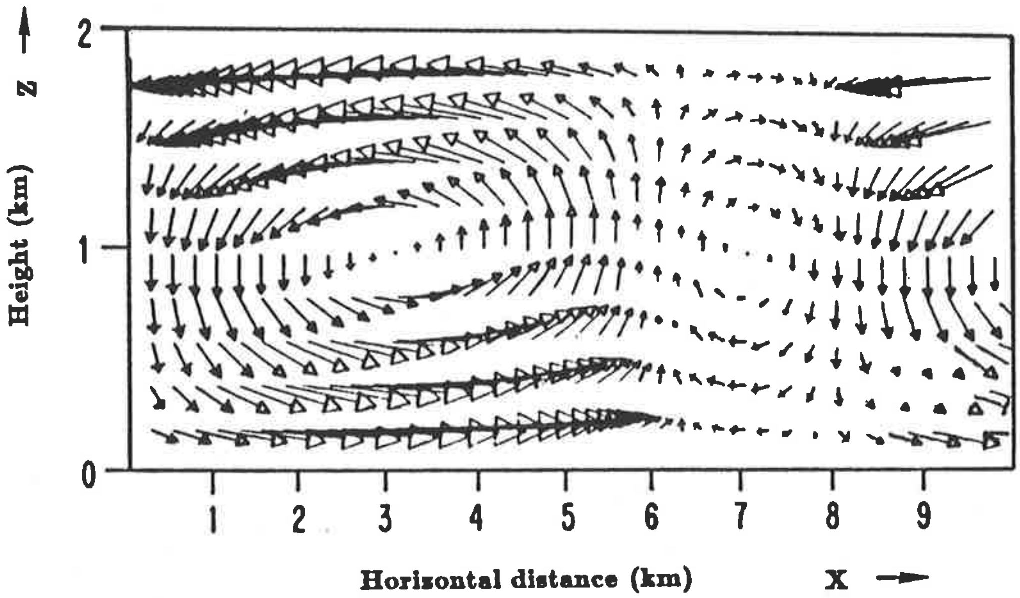

[KROPFI and KOHN, 1978]

Figure 17. Wind field over an urban topography simulated using Doppler radar data. The wind is directed orthogonally out of the plane of the paper, towards the viewer. Note that the wavelength of these roll vortices is approximately twice as large as usual.

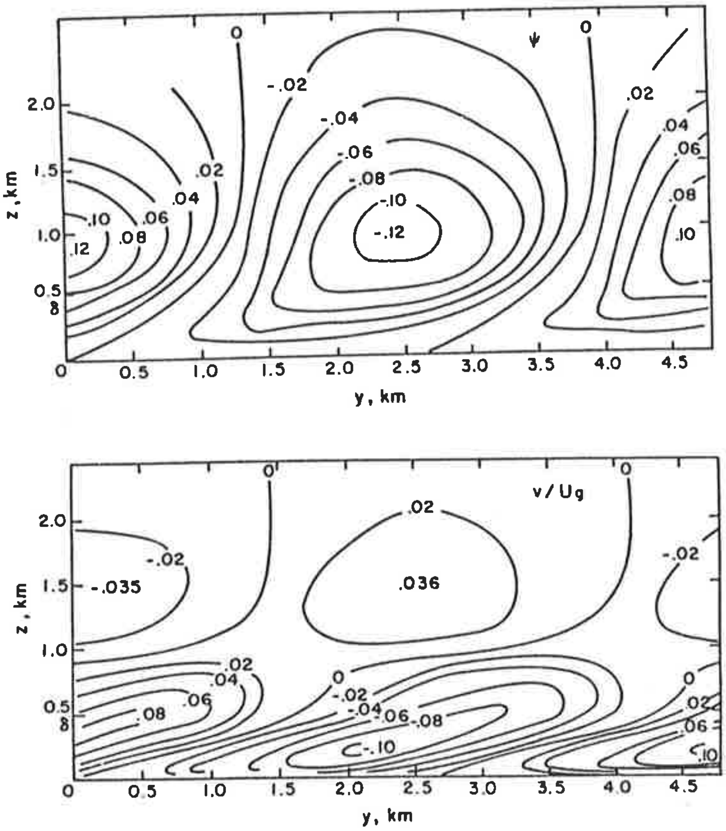

[BROWN, 1980]

Figure 18. "Theoretical secondary flow parameters, stream function ψ, and lateral velocity v for latitude 45°, Ekman depth δ = 400 m, U_g = 10 m/s, and $Re = U_g\delta/K = 486$, where K is the eddy viscosity."

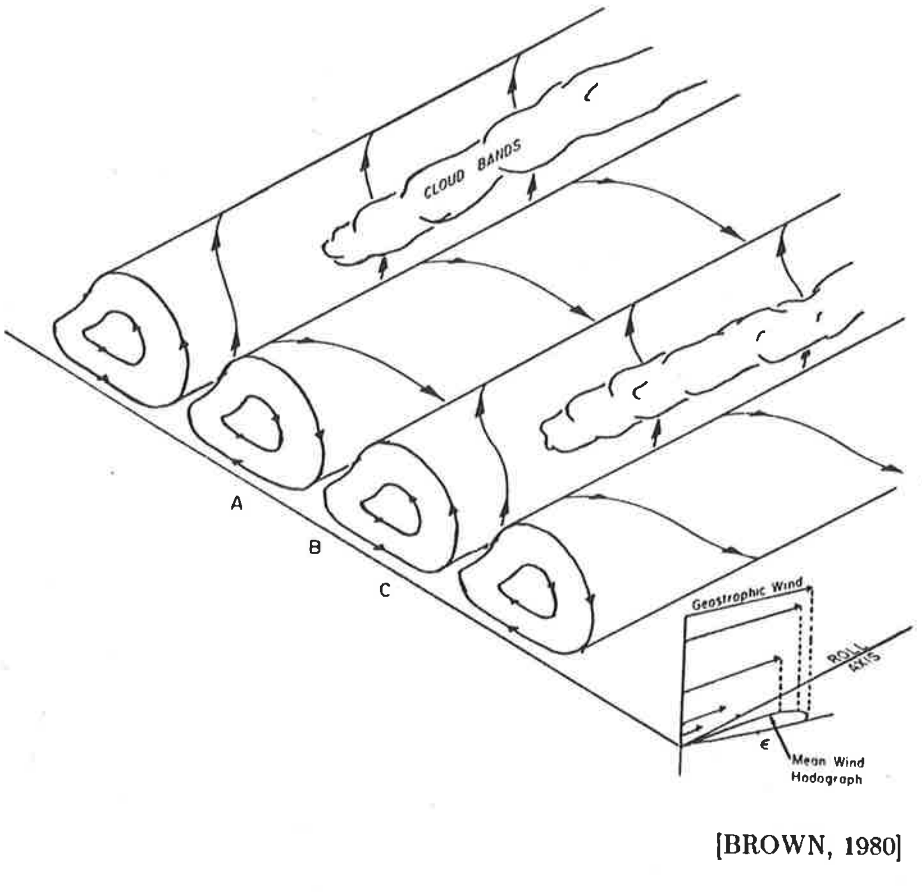

[BROWN, 1980]

Figure 19. Theoretical secondary flow in the planetary boundary layer.

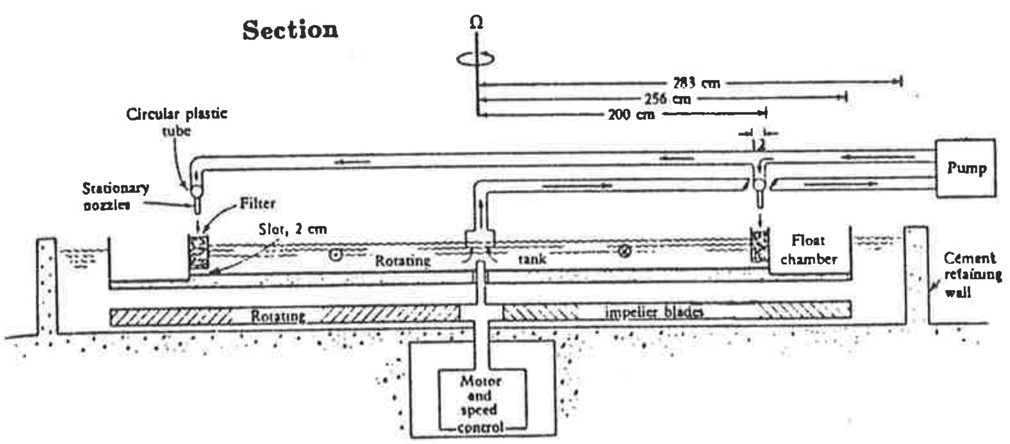

[FALLER and KAYLOR, 1966]

Figure 20. "Schematic diagram of the rotating tank and mechanism"

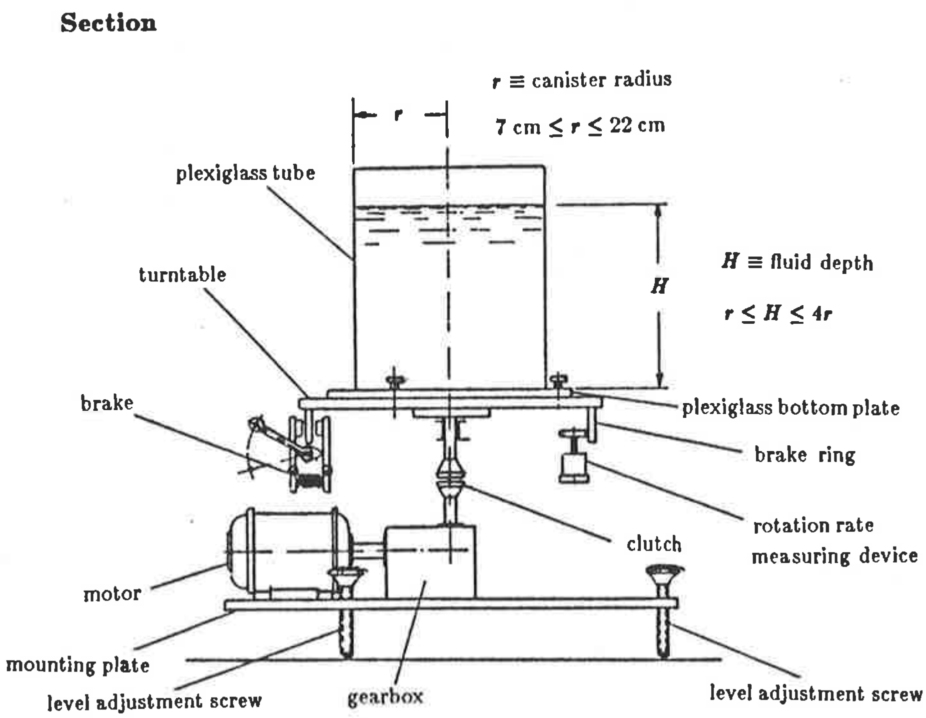

[HORST, 1970b]

Figure 21. Schematic diagram of the rotating canister and mechanism.

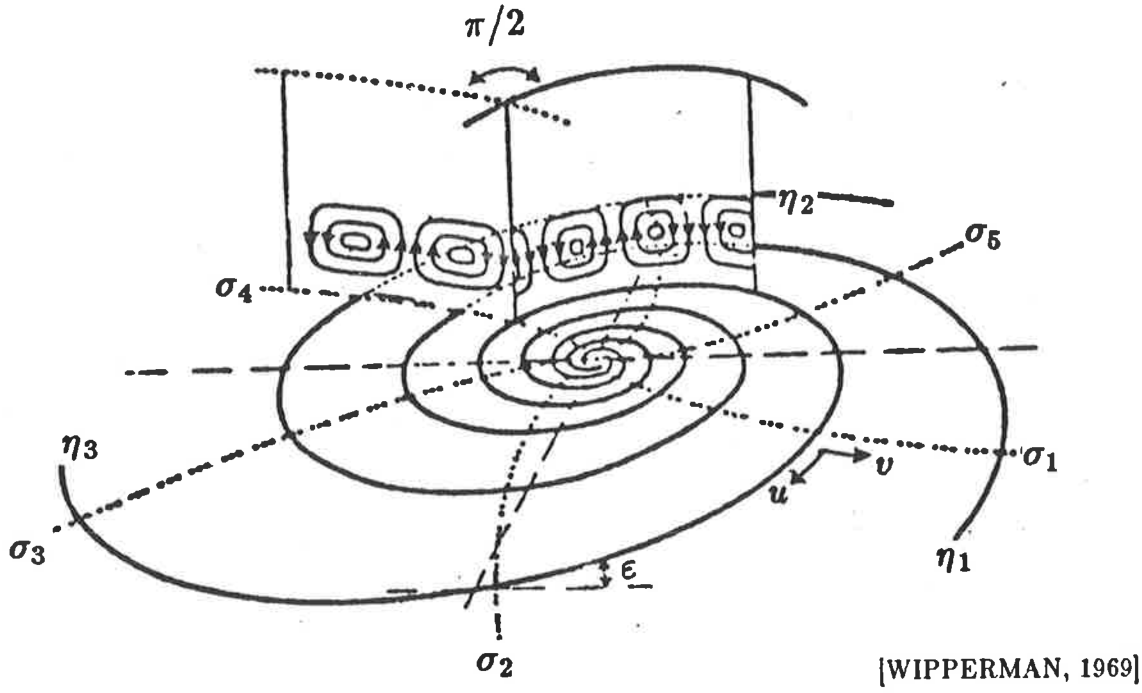

Figure 22. Axes of the two mutually orthogonal sets of roll vortices. $\sigma_i \equiv$ axes of transverse roll vortices, and $\eta_i \equiv$ axes of longitudinal roll vortices

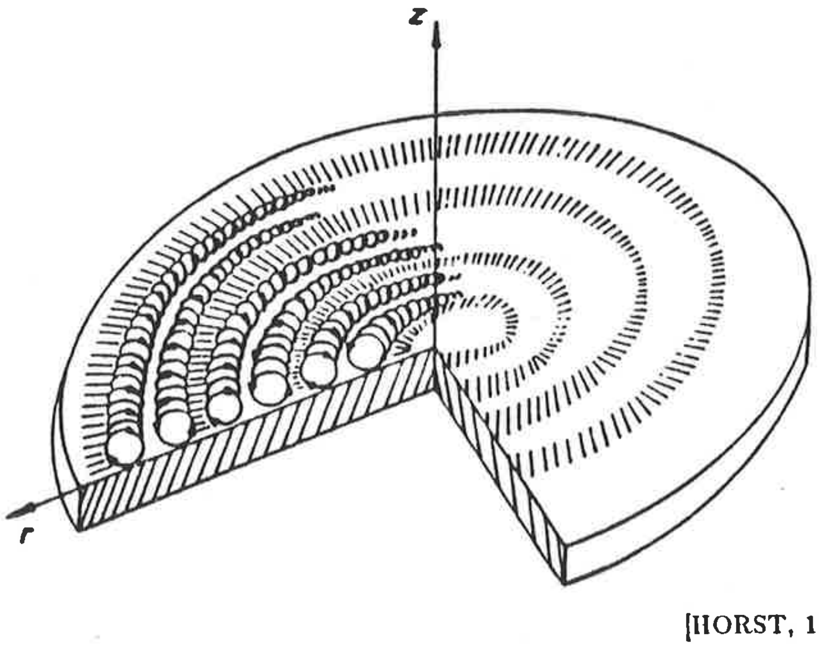

Figure 23. The formation of spiral sediment bands by roll vortices.

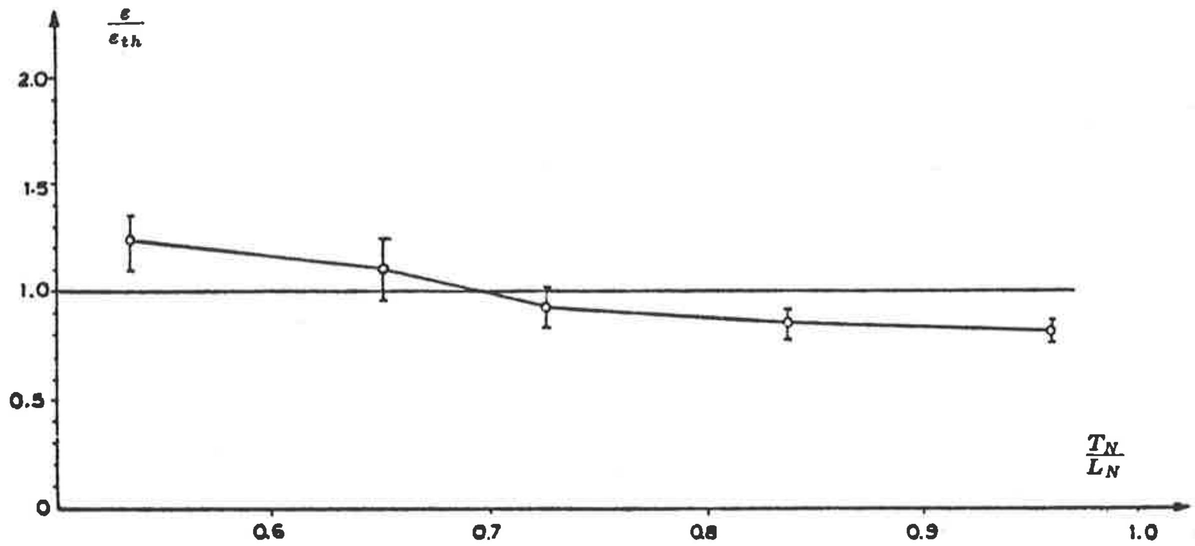

[HORST, 1970b]

$\bar{\varepsilon} = 13°11'$ $\bar{\varepsilon}_{th} = 13°11'$

ε ≡experimental value of the angular difference between longitudinal roll vortices and the mean flow

ε_{th} ≡theoretical value of the angular difference between longitudinal roll vortices and the mean flow

$\frac{T_N}{L_N} \equiv \frac{\lambda_\mu}{\lambda_\nu}$ in WIPPERMAN.

T_N ≡wavenumber of transverse roll vortices

L_N ≡wavenumber of longitudinal roll vortices

Figure 24. The ratio of the measured to calculated angular divergence of longitudinal roll vortices from the mean flow as a function of the ratio of longitudinal roll vortices wavelength to transverse roll vortices wavelength.

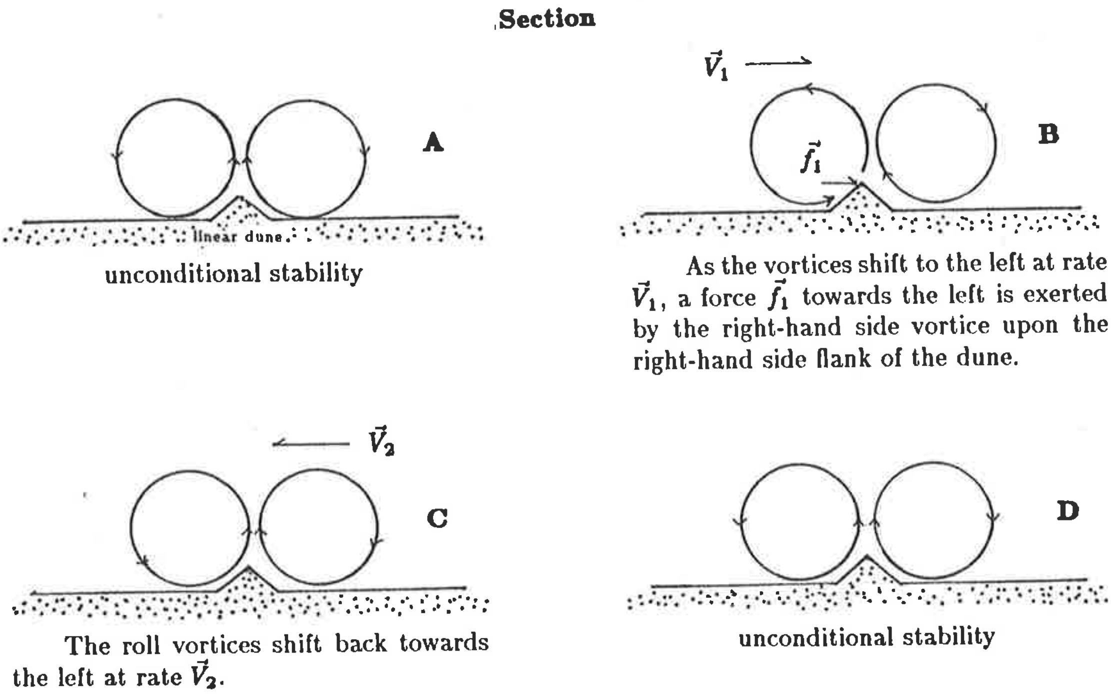

Figure 25.

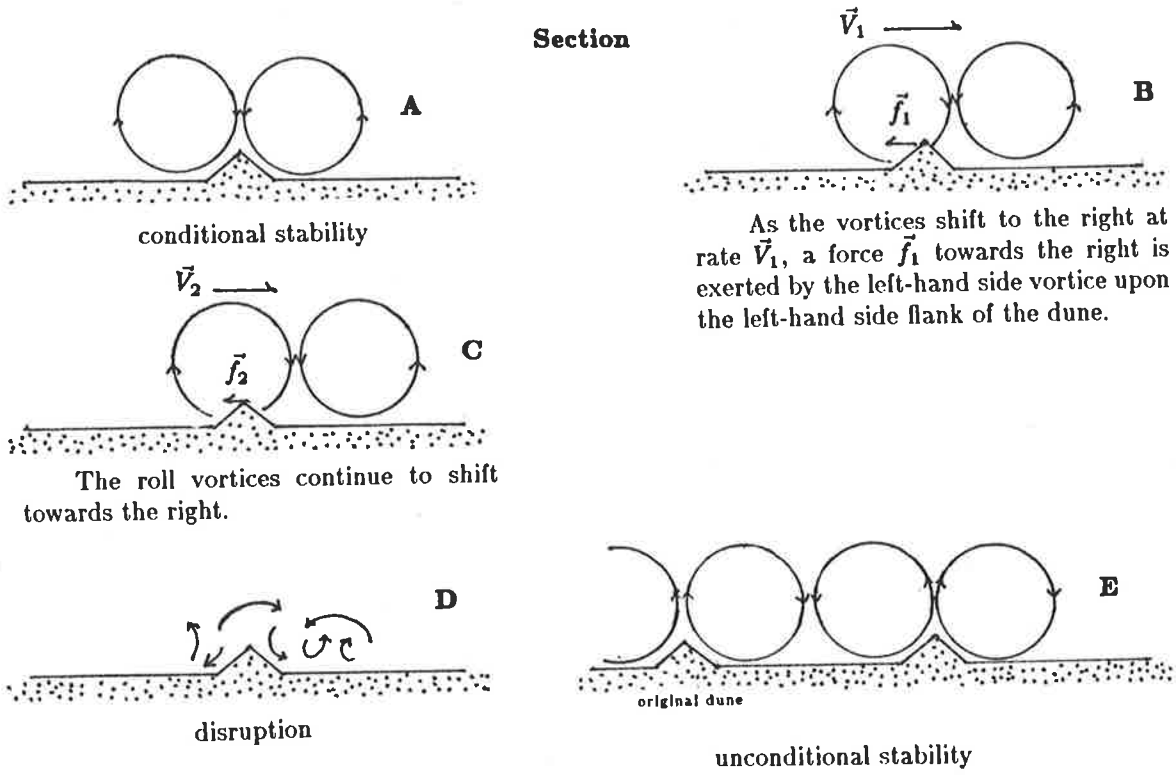

Figure 26.

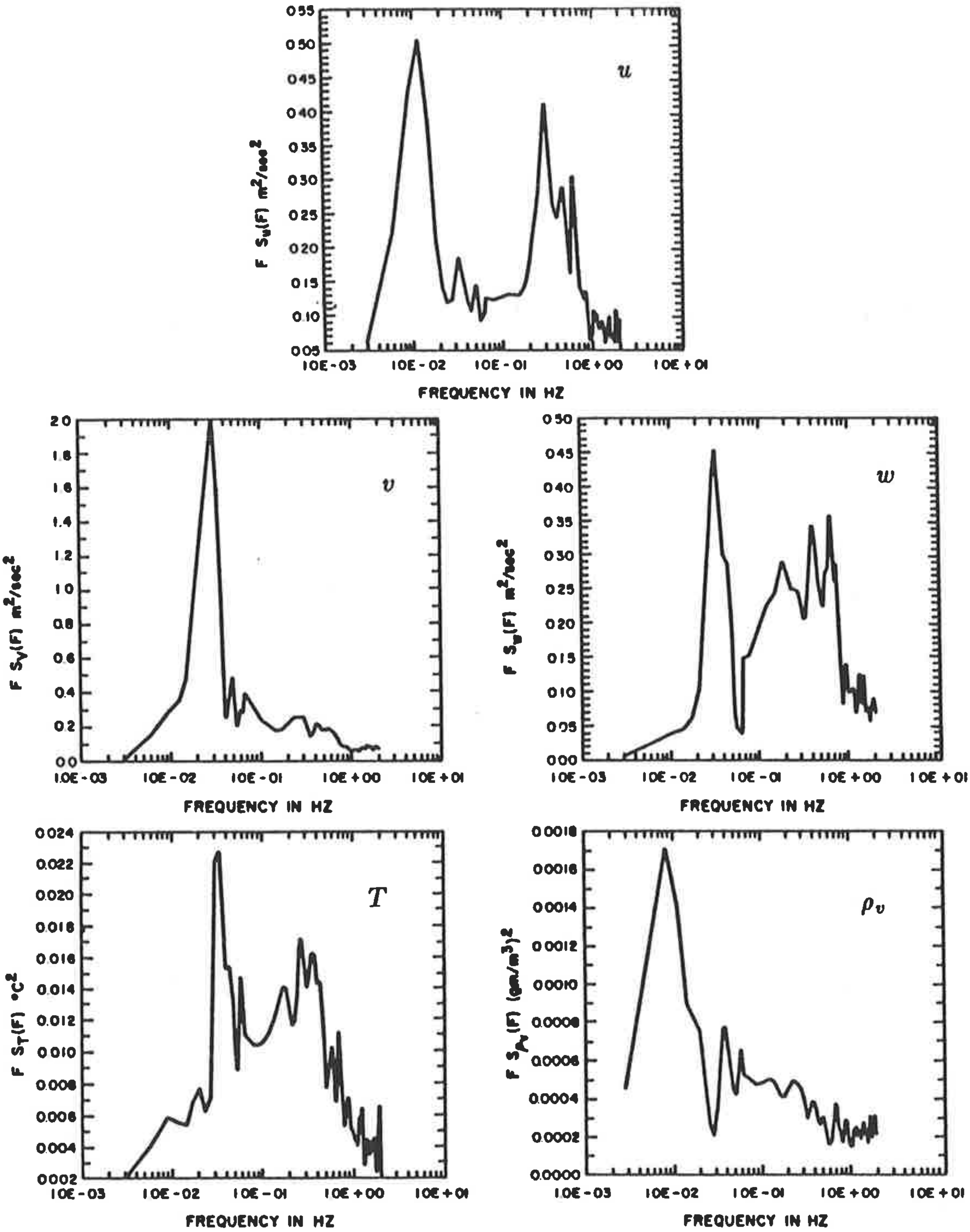

[LEMONE, 1976]

Figure 27. Spectra of velocity components of u, v and w (roll coordinates), temperature T, and absolute humidity ρ_v from the NCAR Buffalo aircraft flying normal to roll axis at 100-170 m above undulating terrain, near Haswell, Colo., meteorological tower. Airspeed 70 m/s. Spectra computed from 5 min of data.

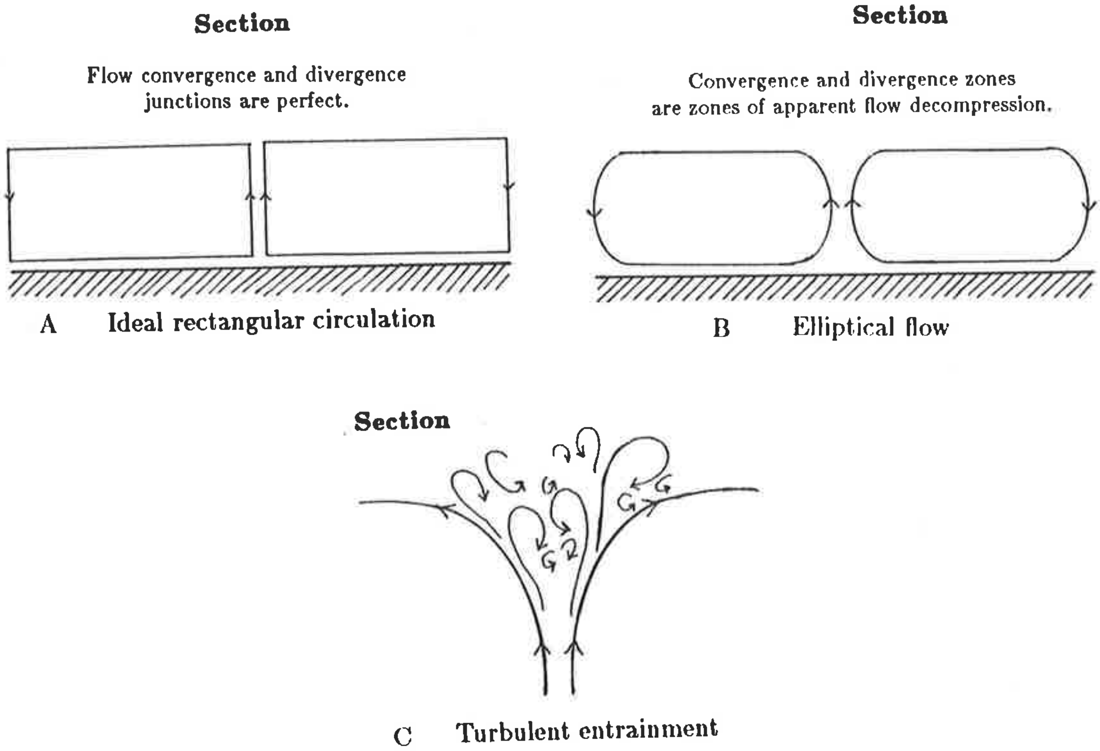

Figure 28. A) Ideal rectangular circulation in which the flow convergence and divergence zones experience neither flow decompression or turbulent entrainment. B) Natural elliptical circulation with apparent flow decompression and therefore apparent violation of mass conservation in flow convergence and divergence zones. C) Turbulent entrainment of air in the convergence and divergence zones maintain mass conservation.

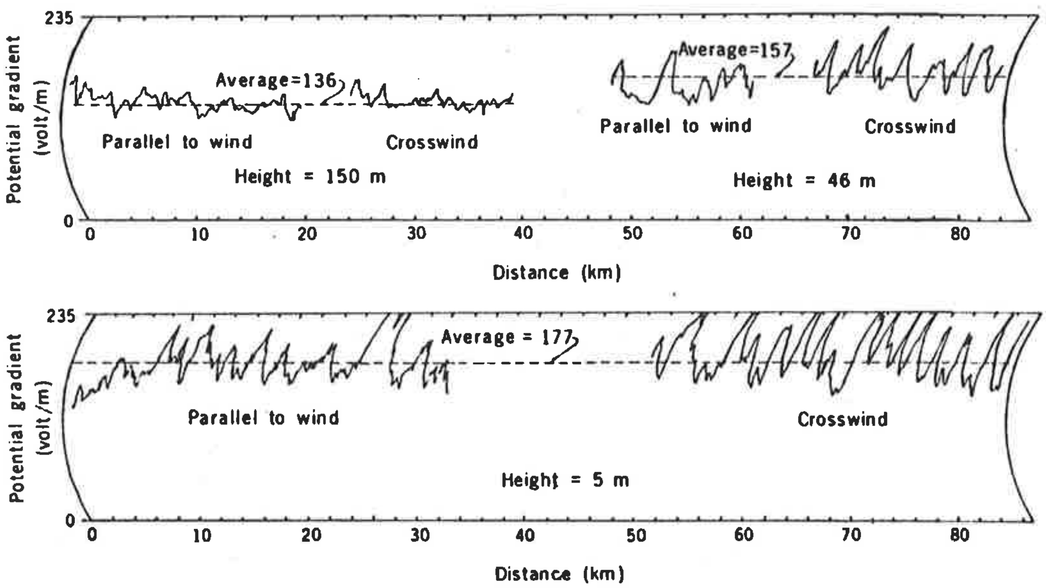

[MARKSON, 1975]

Figure 29. "Variations of the vertical potential gradient during measurement periods of extended duration and constant height close to the sea east of Eleuthera, Bahamas, on 19 December 1971."

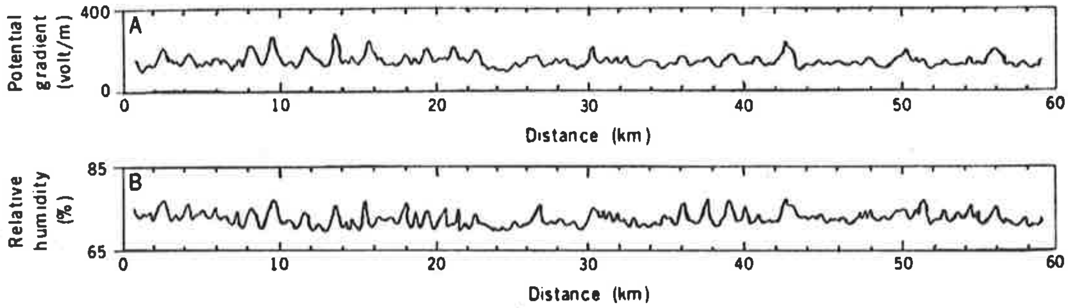

Figure 30. "Simultaneous records of the vertical potential gradient (A) and relative humidity (B) showing correlation. Data were obtained at an altitude of 16 m over the ocean off Eleuthera."

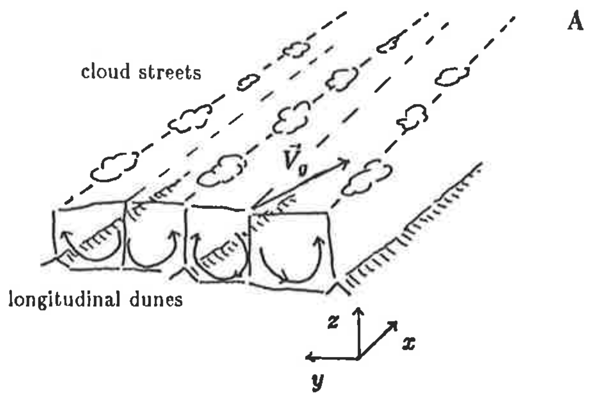

[as modified from LEMONE, 1972]

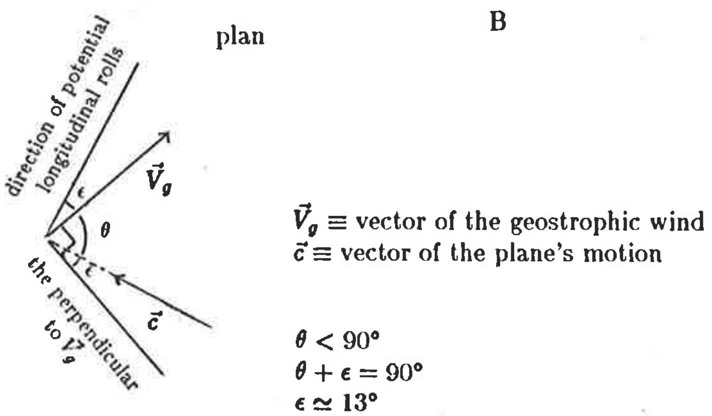

Figure 31. A) The relationship between geostrophic wind $\vec{V}_g$ and roll vortices. B) The orientation of potential roll vortices during strong winds and the crossflow direction for observation flights.

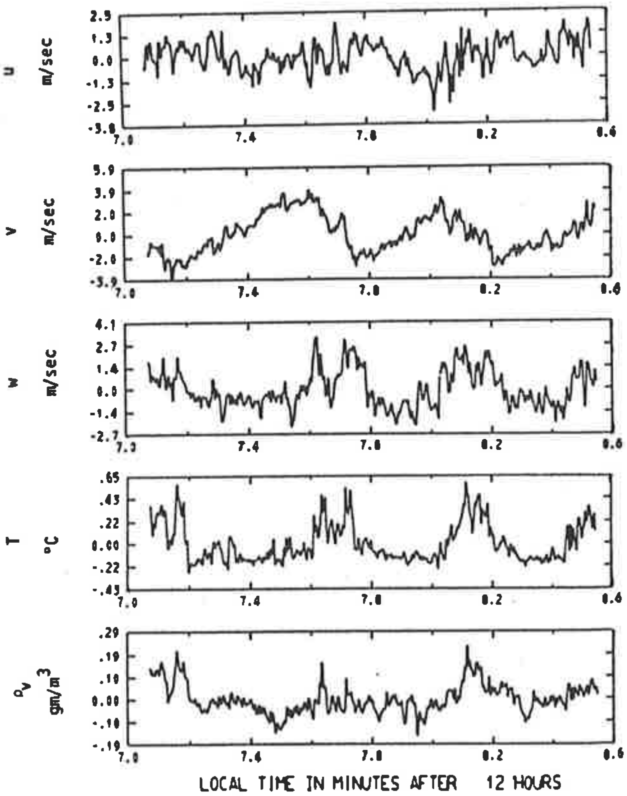

[LEMONE, 1976]

Figure 32. "Fluctuations of wind components u, v and w (roll coordinates), temperature T, and absolute humidity ρ_v, as recorded by the NCAR Buffalo aircraft flying normal to well-organized rolls 175 m above the surface. Airspeed is 70 m/s; Obukhov length L, -100 m; inversion height, 1000 m; Haswell, Colo., 1 October 1970."

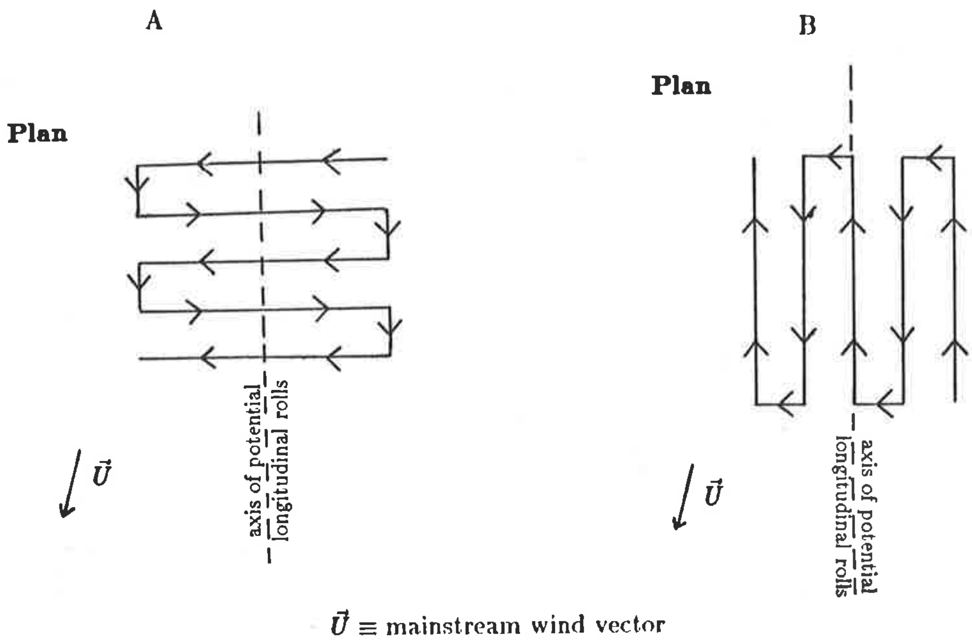

Figure 33. A) Recommended flight pattern for crosswind observation. B) Recommended flight pattern for observation parallel to potential roll vortices.

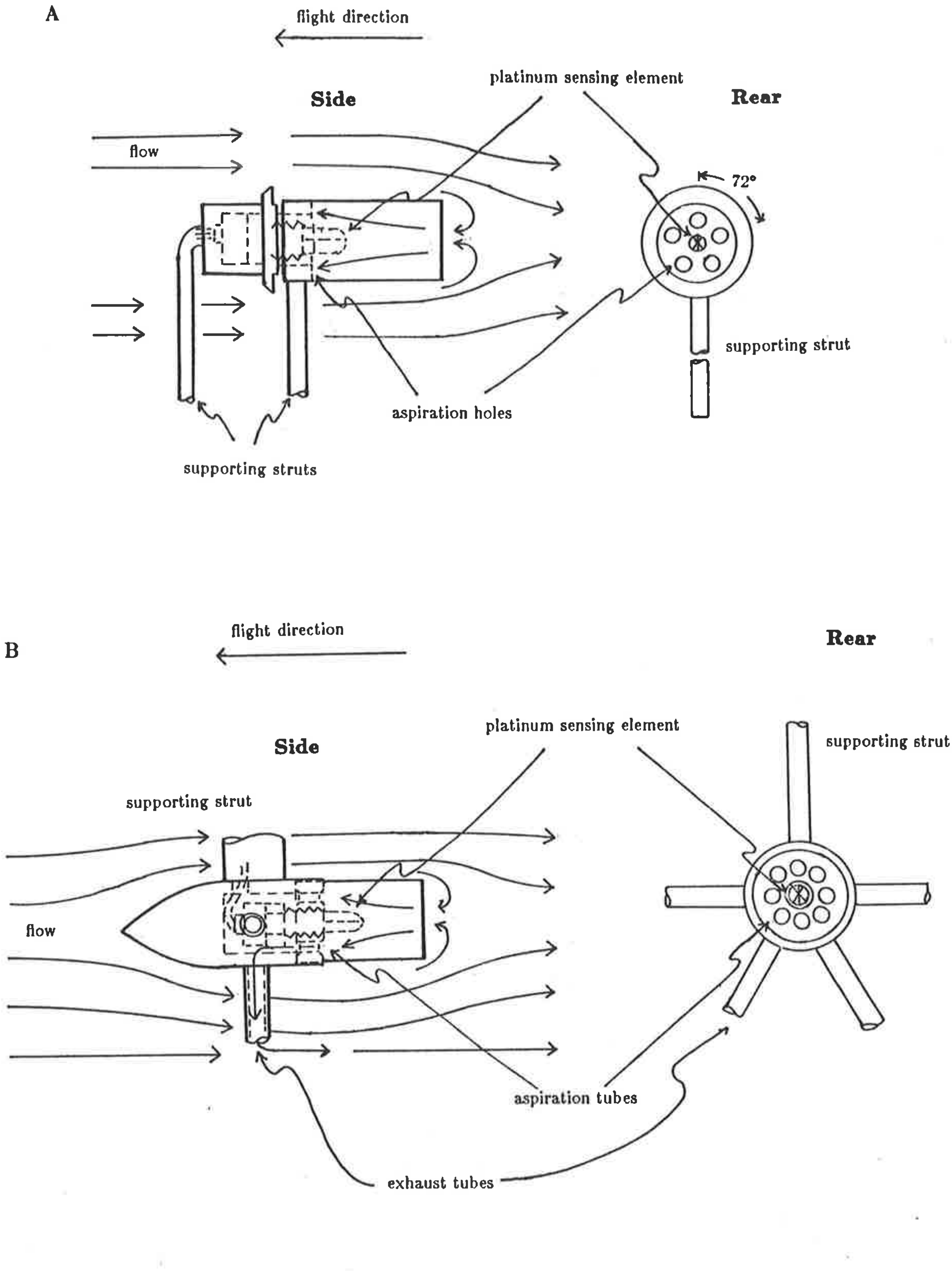

[after RODI and SPYERS-DURAN, 1971]

Figure 34. A) Reverse-flow temperature probe. B) Improved reverse-flow temperature probe.

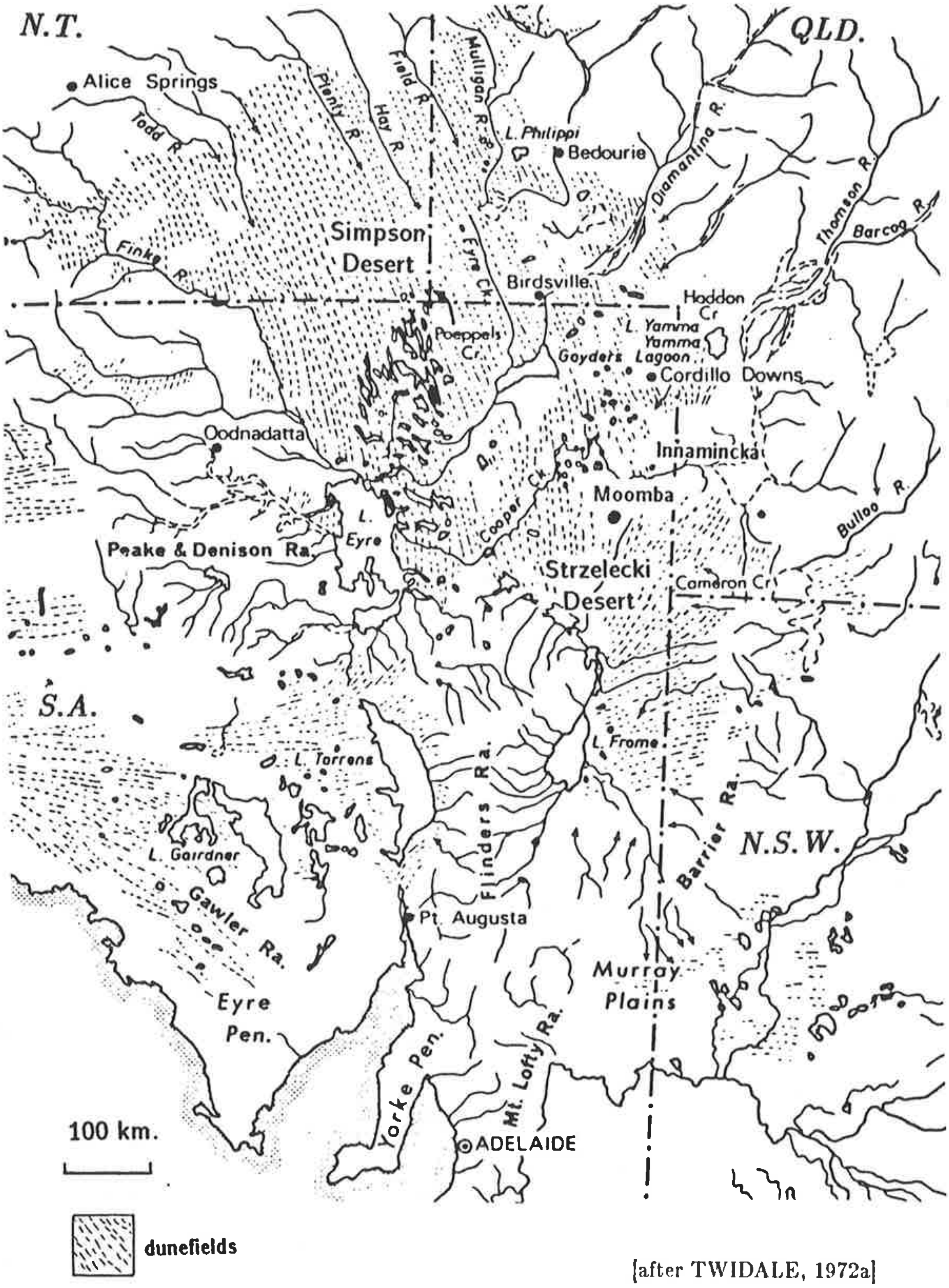

[after TWIDALE, 1972a]

Figure 35. Simpson Desert, Strzelecki Desert and environs.

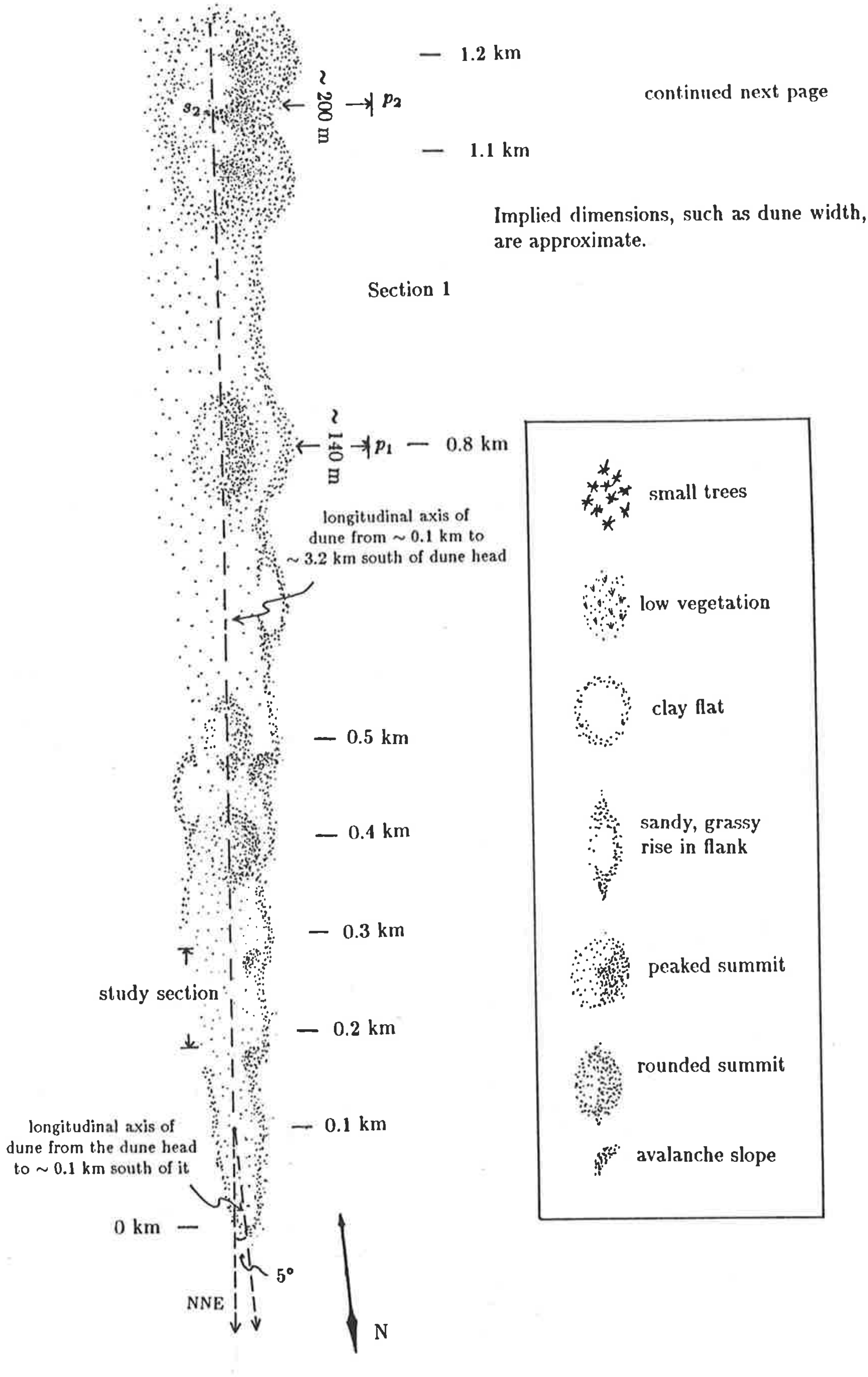

Figure 36. Plan-view symbolic representation of study linear dune depicting salient geomorphic features. Due to insufficient information, the outline of the eastern dune flank in Secton 1 is incomplete. The peak of summit s_1 is ~ 20 m above the base of the dune, and the peak of summit s_2 is ~ 30 m above the base. This latter is perhaps the highest point along the dune. At point p_1, the dune base slopes up towards the dune at ~ 5°, and at point p_2, the dune base slopes up towards the dune at ~ 4°. Finally, the longitudinal axis of the dune shifts towards the west by ~ 5° twice, at points ~ 0.1 km and ~ 3.2 km south of the dune head.

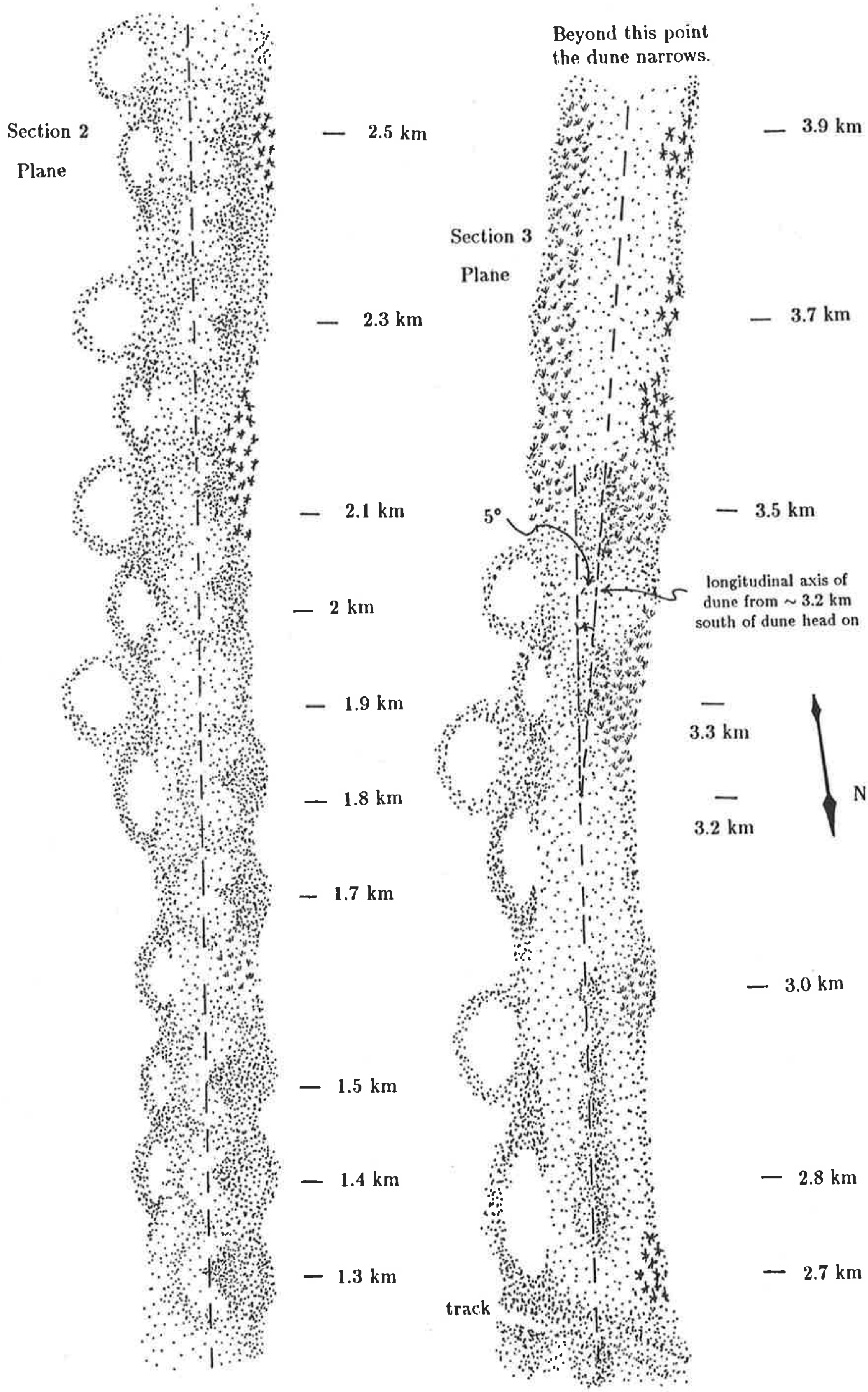
Section 2
Plane
2.5 km
2.3 km
2.1 km
2 km
1.9 km
1.8 km
1.7 km
1.5 km
1.4 km
1.3 km
Beyond this point
the dune narrows.
Section 3
Plane
3.9 km
3.7 km
3.5 km
5°
longitudinal axis of
dune from ~ 3.2 km
south of dune head on
3.3 km
3.2 km
N
3.0 km
2.8 km
2.7 km
track

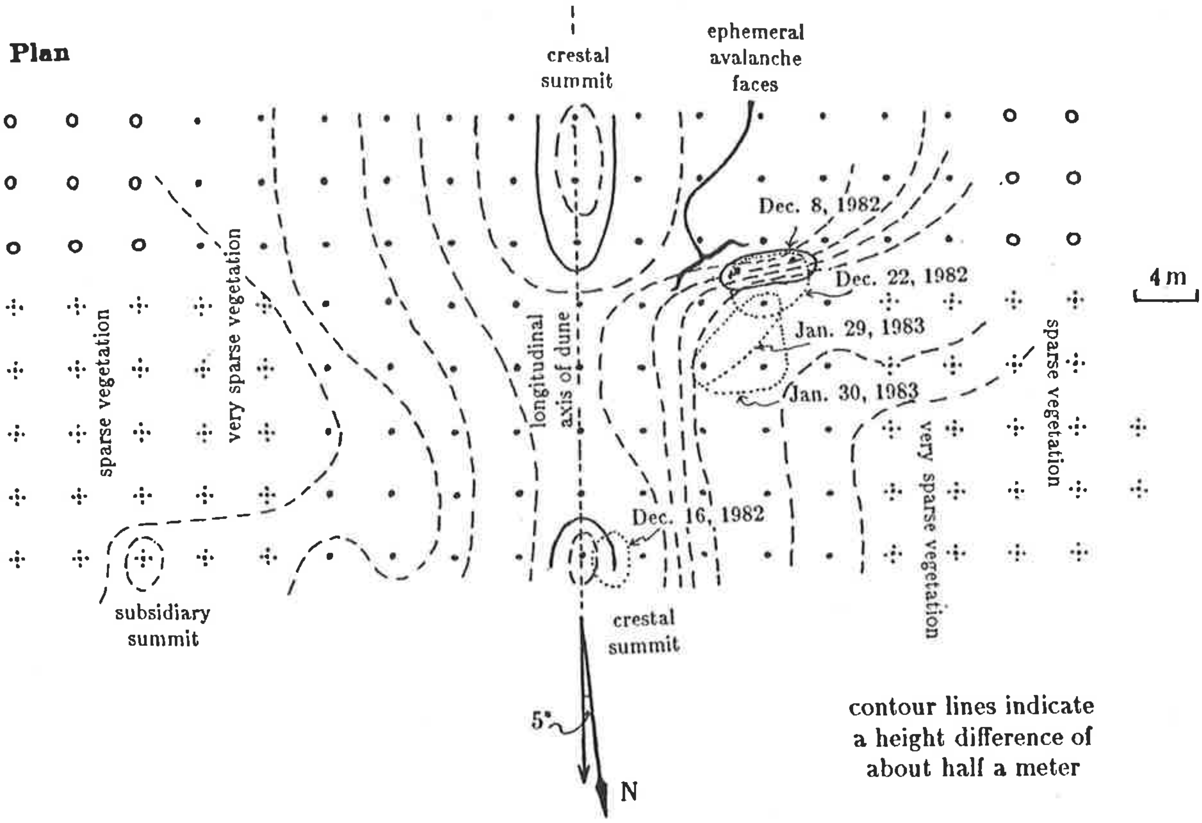

• stakes planted on December 8, 1982

o stakes planted on December 10, 1982

·⁞· stakes planted on December 11, 1982

– – – topographic contours sketched on December 10, 1982

Figure 37. Grid of stakes and topographic form lines.

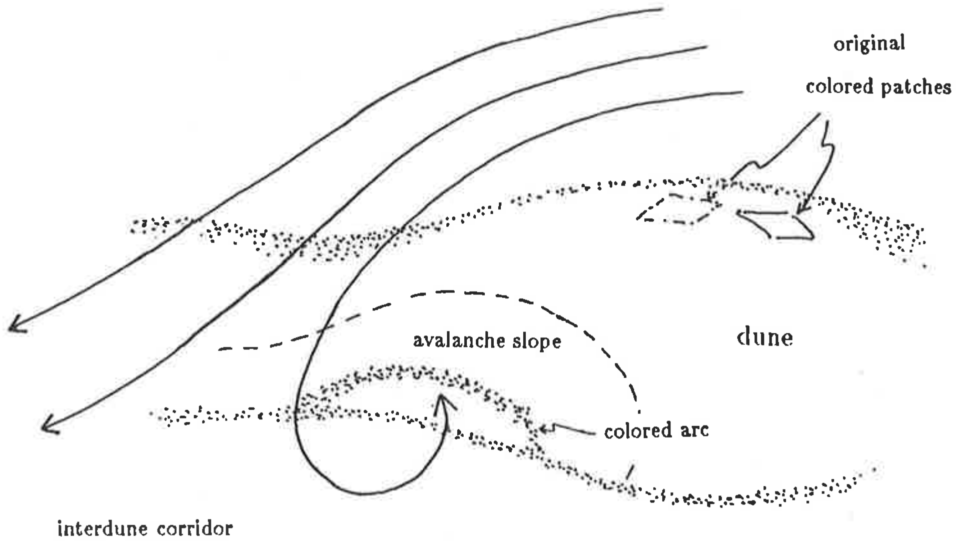

Figure 38. The leeward side rotor and the resultant arc of colored sand aggregates on the avalanche face. The highest point of the study site is ~ 5 m above the eastern side interdune corridor. The avalance face is ~ 2 m deep, and the high point of the colored arc is about 1/3 way up the greatest depth of the avalanche face

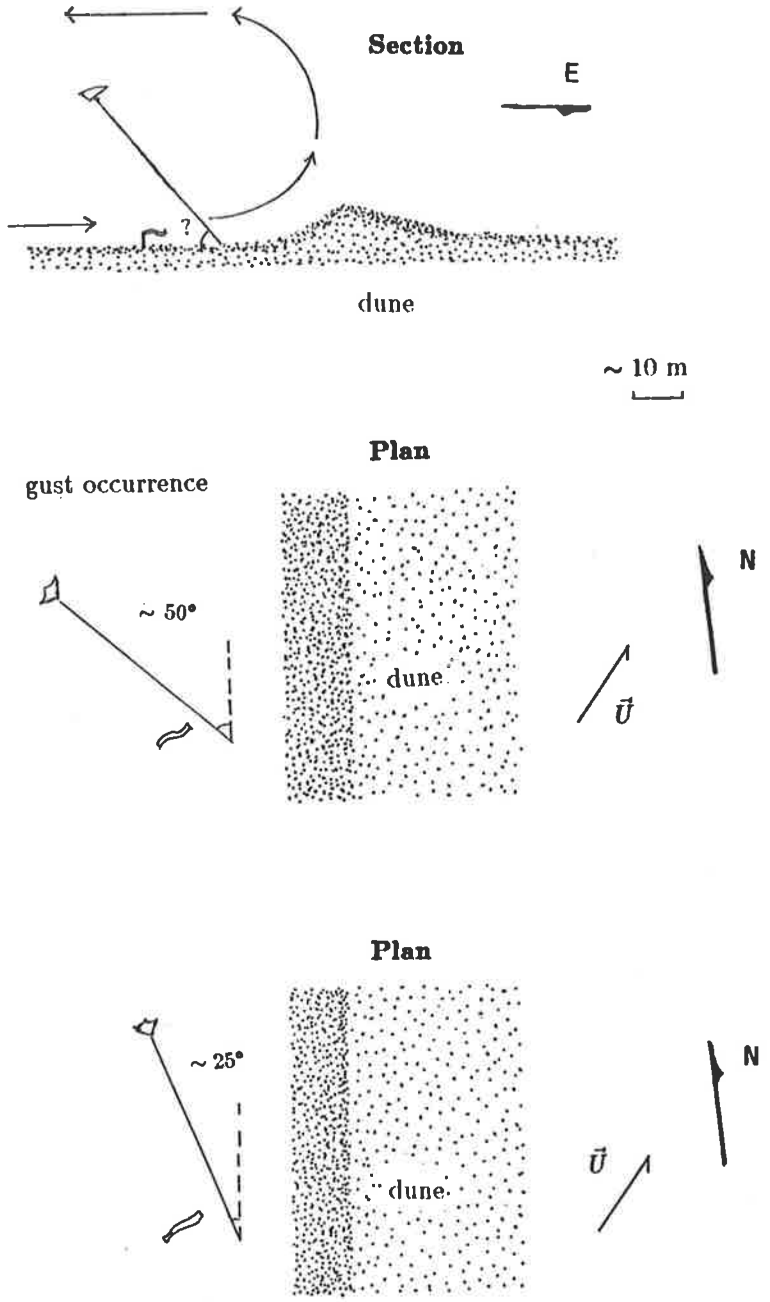

Figure 39. Kite and ribbon configuration believed to indicate a windward side rotor. Mainstream wind in all frames was from ~ 220° SSW. Mean wind speed was ~ 13 knots, and gust speed was >15 knots. Time for all frames was around 5:00 PM, December 17, 1982. Exact angular orientation for the ribbon in the plan frames is unknown. Kite cord length was ~ 50 m. symbols as in Fig. 37

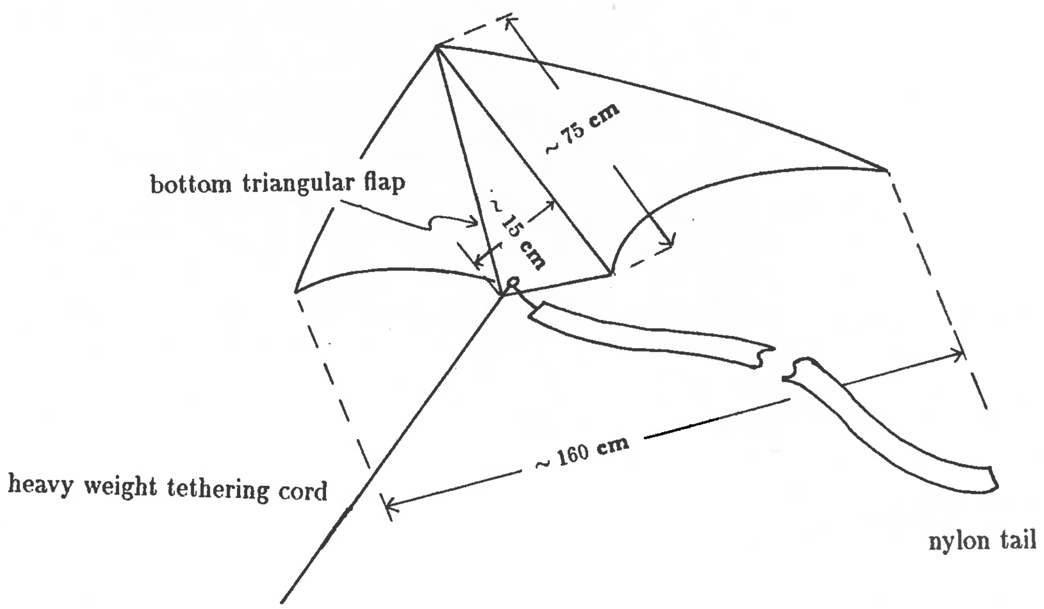

Figure 40. Delta wing kite with ~ 50 m tethering cord and 6 - 7 m nylon tail.

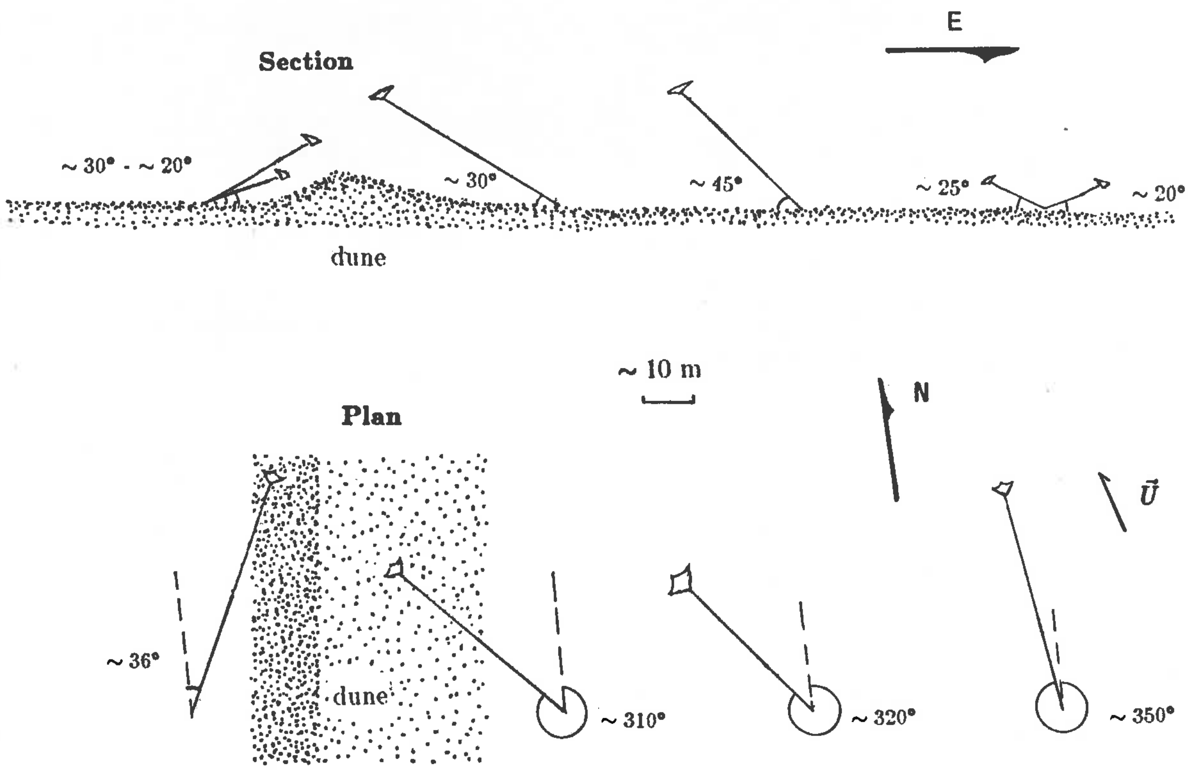

Figure 41. Kite flight configuration believed to indicate roll vortices centered on the dune during nearly parallel wind. Wind was shifting slightly between SSE and SSW. Mean wind was from ~ 164° SSE at ~ 10 knots ±4 knots. Time was around 3:00 PM on December 18, 1982. Note that from the viewing perspectives chosen, tethering lines appear to be of different lengths although they were uniformly ~ 50 m.

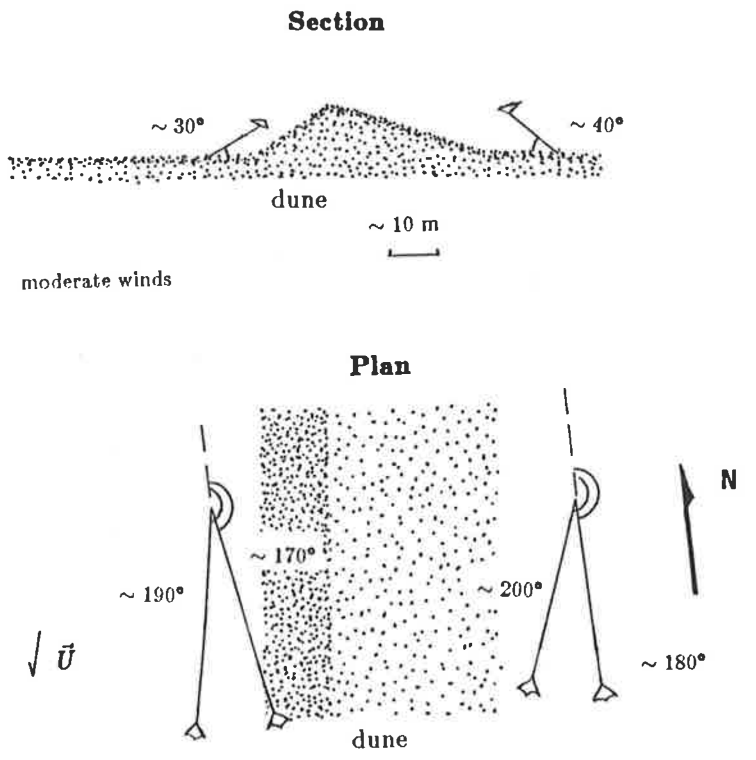

Figure 42. Tethered kites configuration believed to indicate roll vortices around the study dune. Mean wind was from ~ 14° NNE at ~ 7 knots. The observation was made around 2:30 PM on December 19, 1982. Convergent kite flight lasted for several minutes.

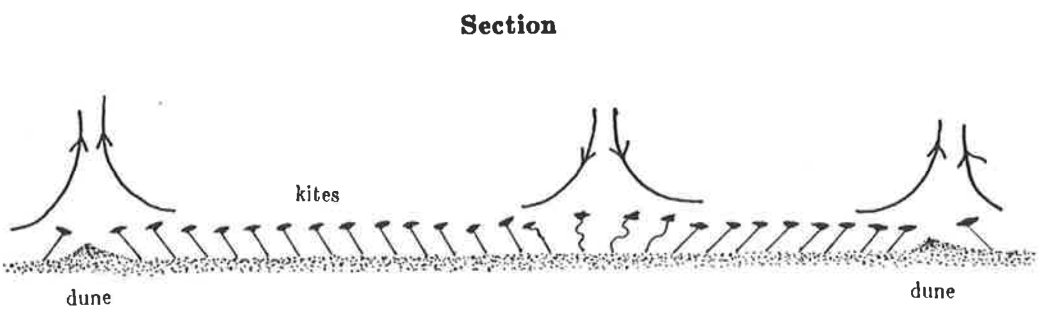

Figure 43. Array of tethered kites for the observation of roll vortices in a linear dune field. A large number of kites distributed over a distance encompassing at least two adjacent dunes is necessary if a complete wavelength of the secondary circulation is to be observed. The mainstream is directed into the plane of the paper.

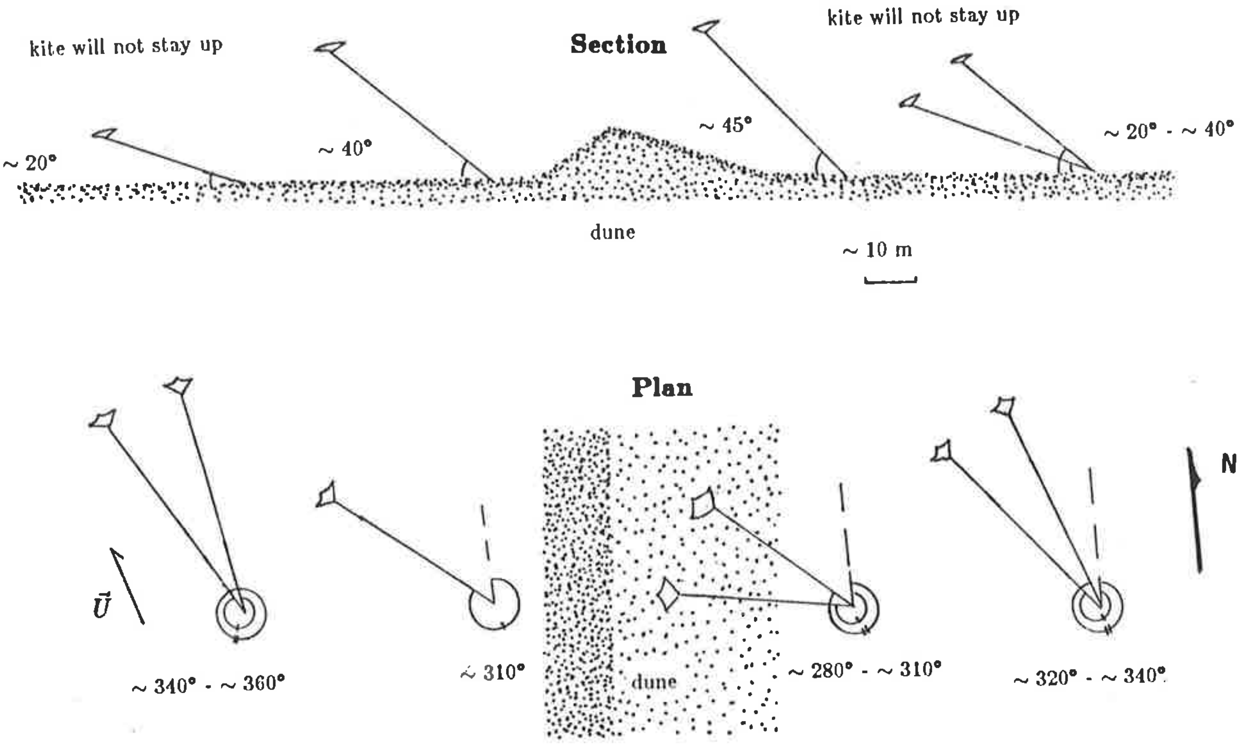

Figure 44. Tethered kites configuration believed to indicate quasi-laminar flow over the study dune during oblique winds. Mean wind was from ~ 160° SSE and at ~ 13 knots. The observation was made during the afternoon of December 19, 1982.

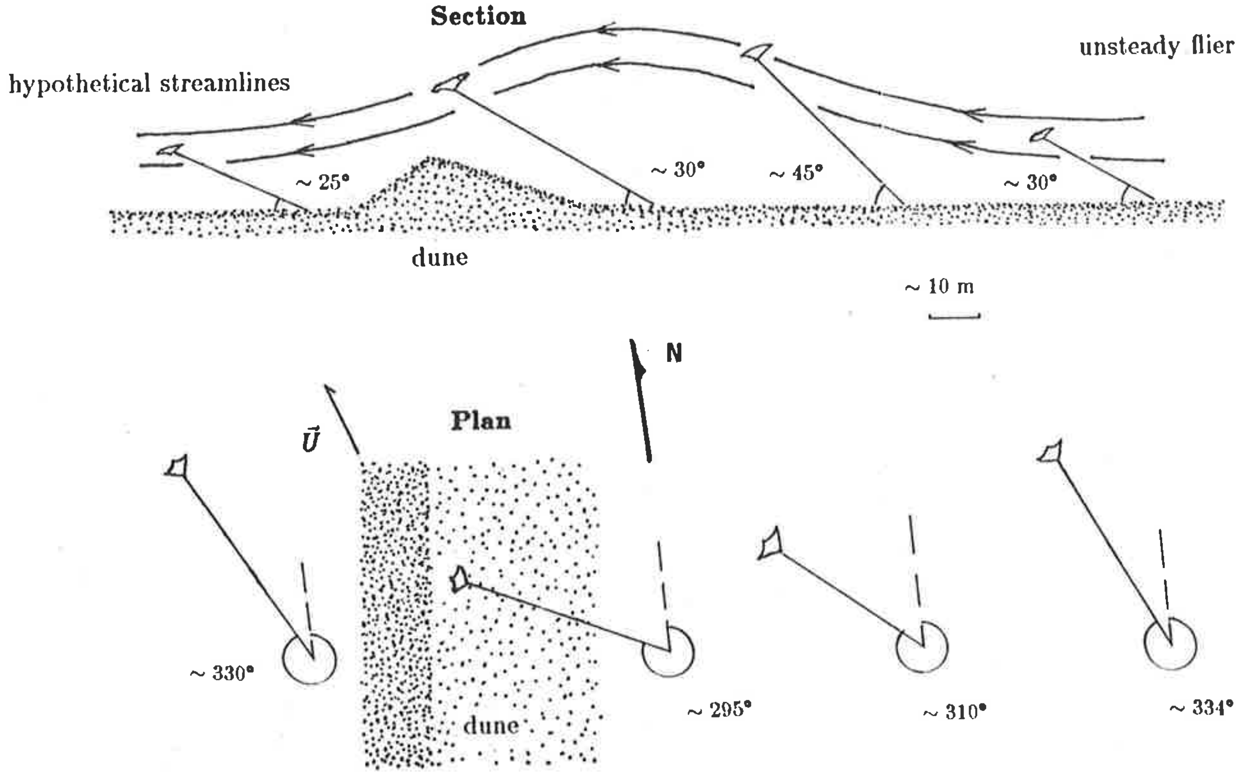

Figure 45. Tethered kites configuration believed to indicate quasi-laminar flow over the study dune during oblique winds. Mean wind was from ~ 160° SSE and at ~ 12 knots. The observation was made at about 9:30 AM on December 18, 1982.

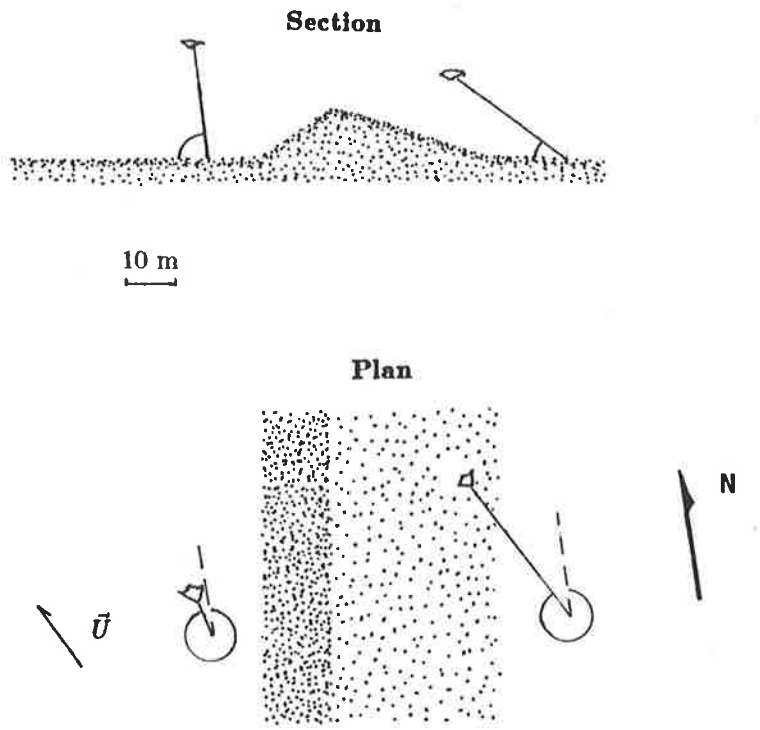

Figure 46. A peculiar tethered kites configuration during oblique flow. Angle measurements were not taken for this configuration. The figure derives from a field sketch in which line vertical inclinations and horizontal orientations were purely qualitatively estimated. Mean wind was from ~ 150° SSE and at ~ 12 knots. The observation was made during the morning of December 19, 1982.

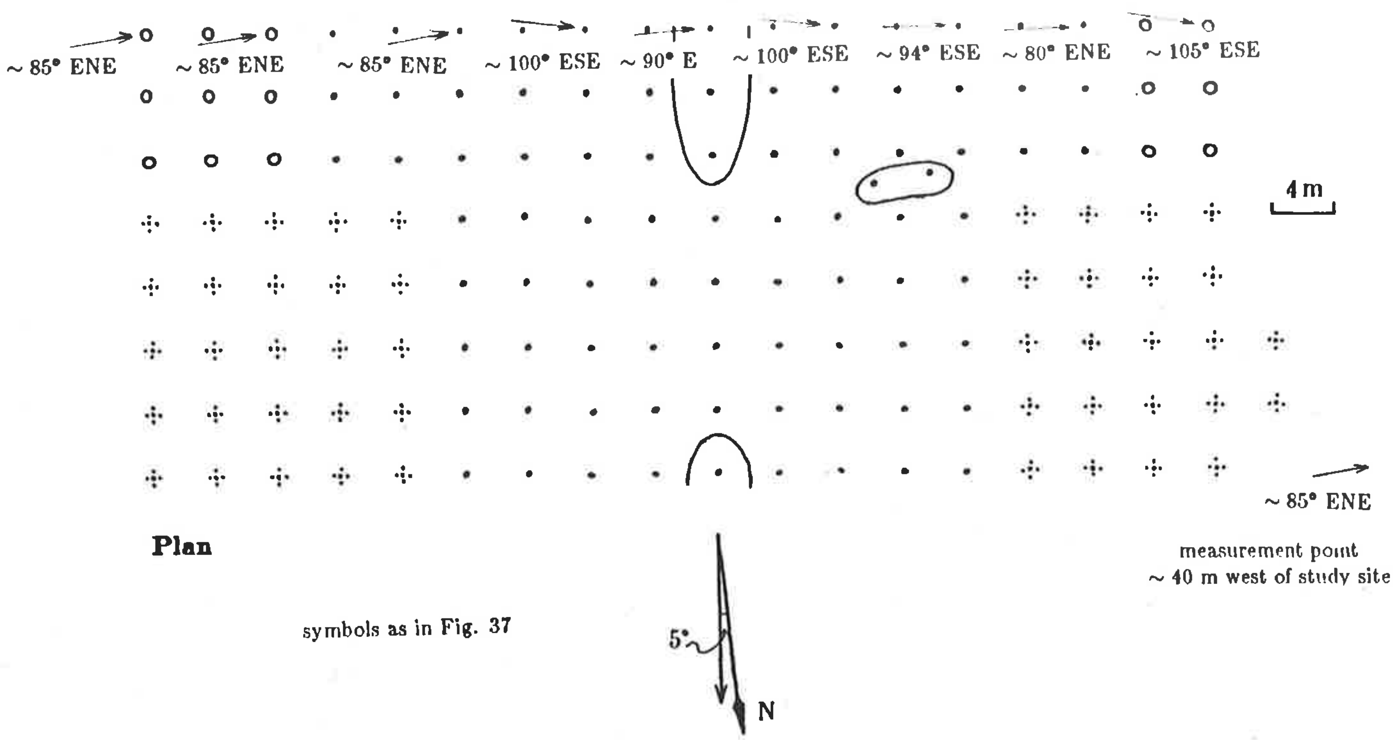

Figure 47. Horizontal plane wind directions across the southern perimeter of the study site. The measurements were made at 8:00 AM on December 11, 1982. At 7:35 AM, the wind was measured at ~ 2 knots from ~ 120° ESE at a point ~ 40 m west of the dune. At 8:30 AM, at this same point, the wind was at ~ 7 knots and from ~ 95° ESE. Because of the similar wind directions at 8:00 and 8:30 at ~ 40 m west of the dune, the wind speed at 8:00 is thought to be close to 7 knots.

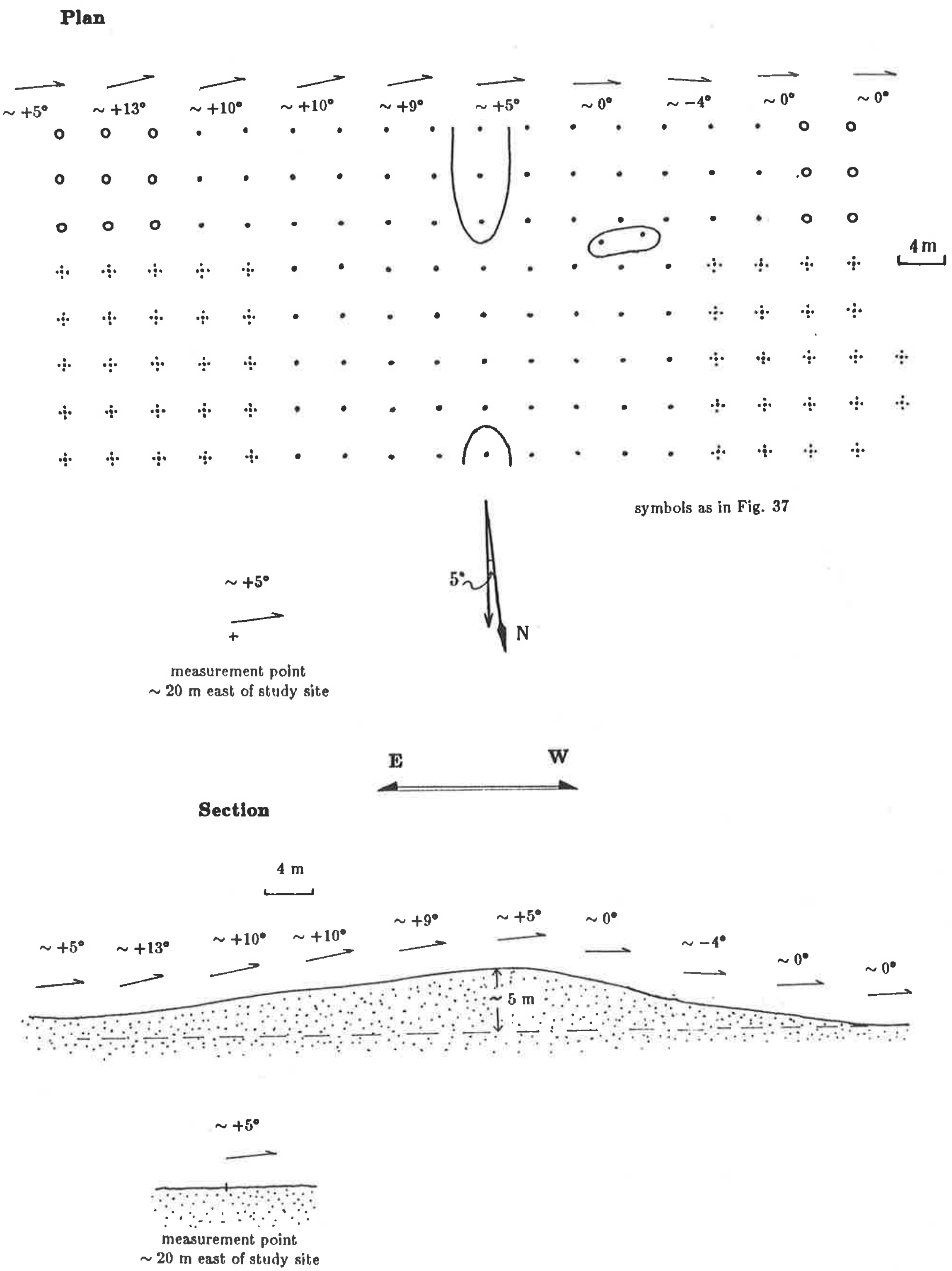

Figure 48. Vertical plane direction vectors of flow across the southern perimeter of study site during oblique winds. Measurements made at 8:45 AM on December 11, 1982.

E ⟵⟶ W

walking from	lower flank	upper flank	crest	upper flank	lower flank	
E to W Trial 1	slow	moderate, fast	fast, fastest	fast, moderate	slow	(9,15)
W to E Trial 2	slow	moderate	slow	moderate	moderate	(0,5)
E to W Trial 3	slow	moderate	fast, fastest	fast, moderate	slow	(7,15)
W to E Trial 4	moderate	slow, slow	moderate, fastest	moderate	slow	(5,10)
E to W Trial 5	moderate	moderate, fast	fastest, fast	moderate	moderate	(10, 13)
W to E Trial 6	moderate	slow, slow	moderate, fastest, moderate	moderate	moderate	(5,10)

4 m

Section

E ⟵⟶ W

Trial 1

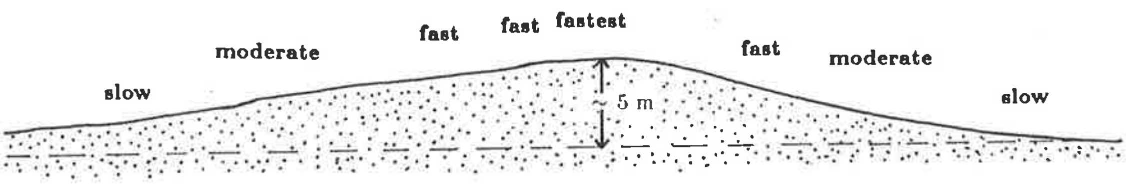

4 m

Figure 49. Relative wind speed measurements across the southern perimeter of the study site. Measurements taken at 8:30 AM on December 11, 1982. Mean wind was at ~ 7 knots and from ~ 95° ESE, making it almost perpendicular with respect to the study site's longitudinal axis. The anemometer was held at a height of ~ 1.4 m. The range of wind speeds for each trial is summarized at the far righthand side of the table, and as a general illustration of wind speed variation, the results of of Trial 1 are shown in relation to a section of the dune in the lower portion of the figure.

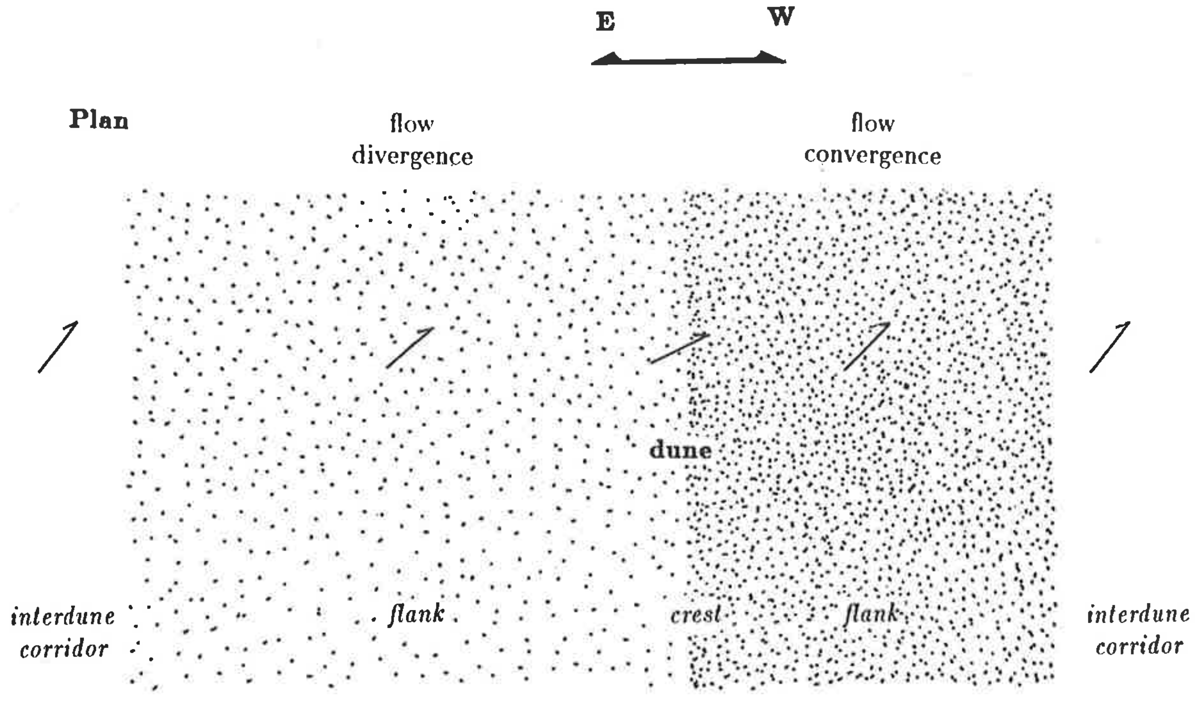

Figure 50. Horizontal flow divergence/convergence pattern over the study linear dune.

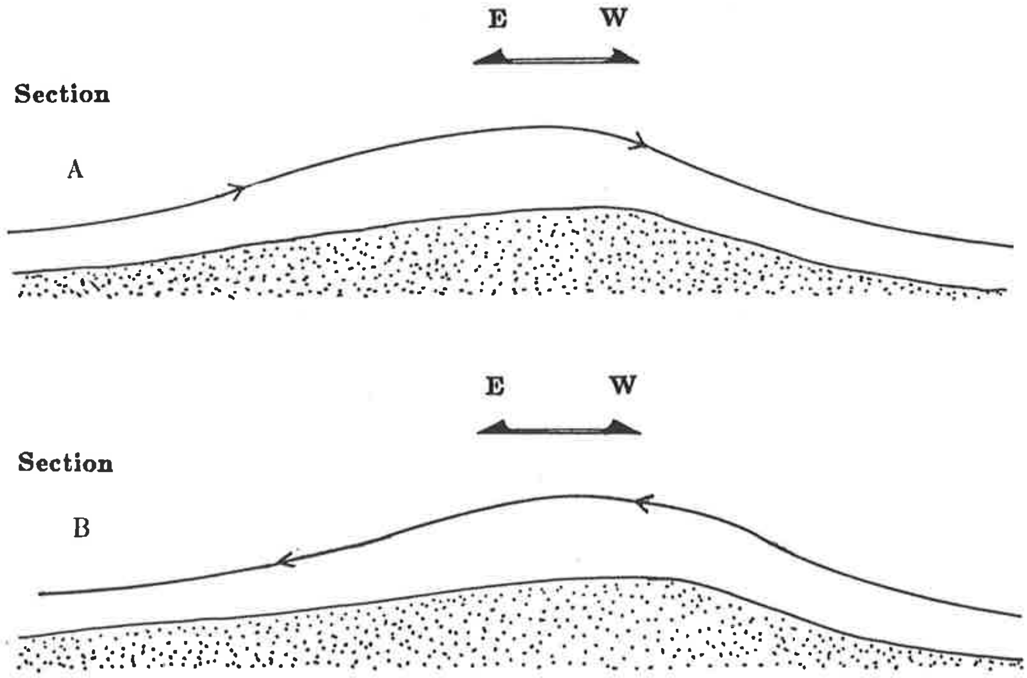

Figure 51. A) Streamline during oblique flow incident upon the broad flank of the study dune. Maximum upward flow component occurs just to windward of the crest. B) Streamline during oblique flow incident upon the avalanche flank of the study dune. Maximum upward flow component occurs just to leeward of the crest.

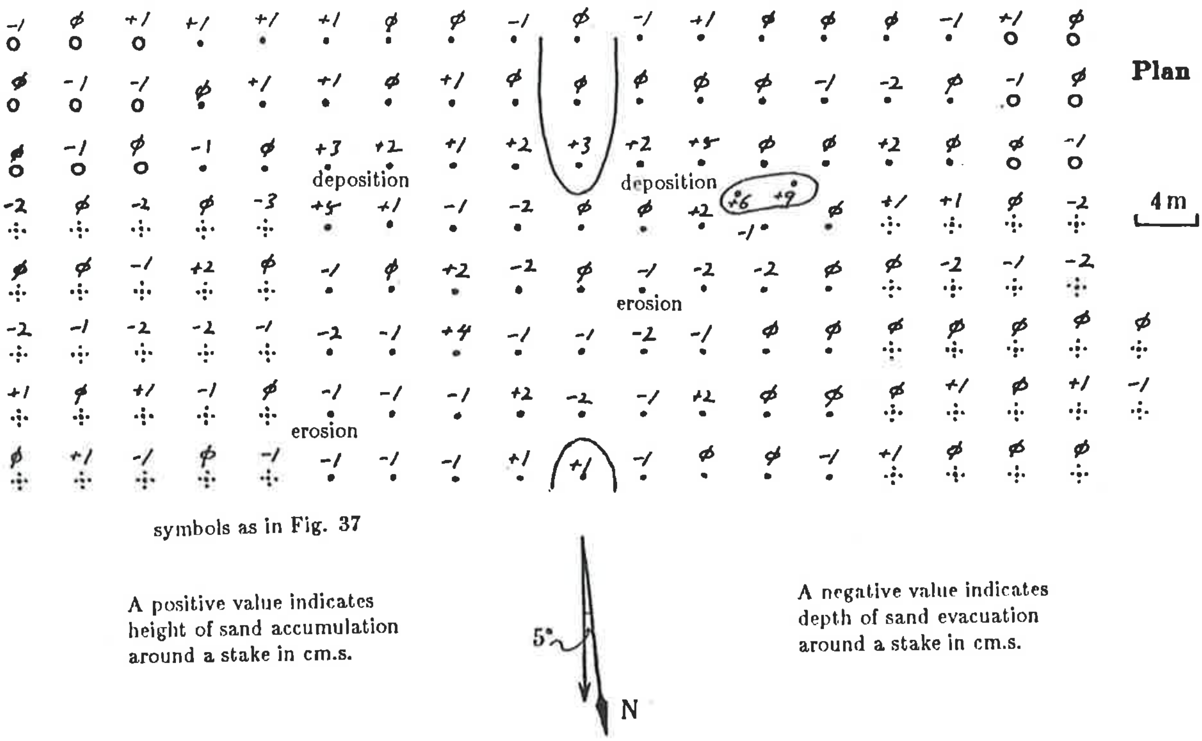

Figure 52. A typical deposition and erosion record for the study site. Southerly winds of ~ 13 knots prevailed during the observation interval, which was from December 16, 1982 (2:50 PM) to December 18, 1982 (8:25 PM).

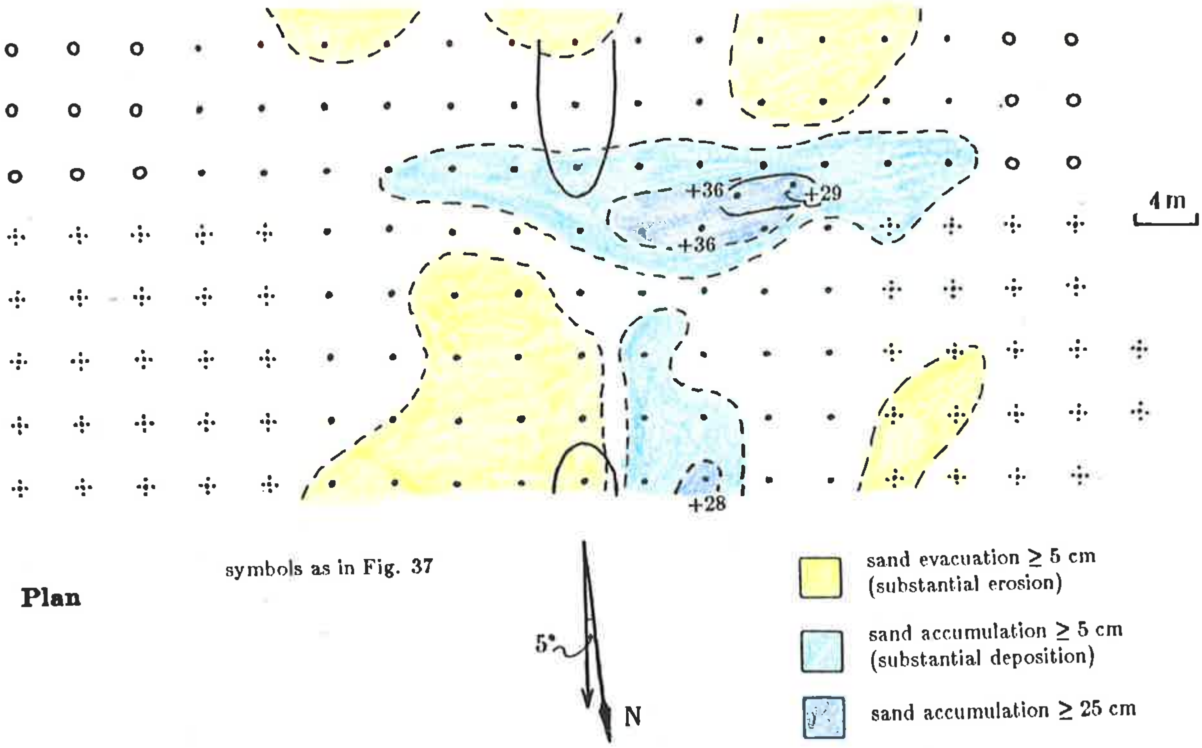

Figure 53. Deposition/erosion pattern over the study site between December 14, 1982 (3:15 PM) and December 24, 1982 (8:30 PM). Southeasterly winds prevailed during the observation interval.

Plan

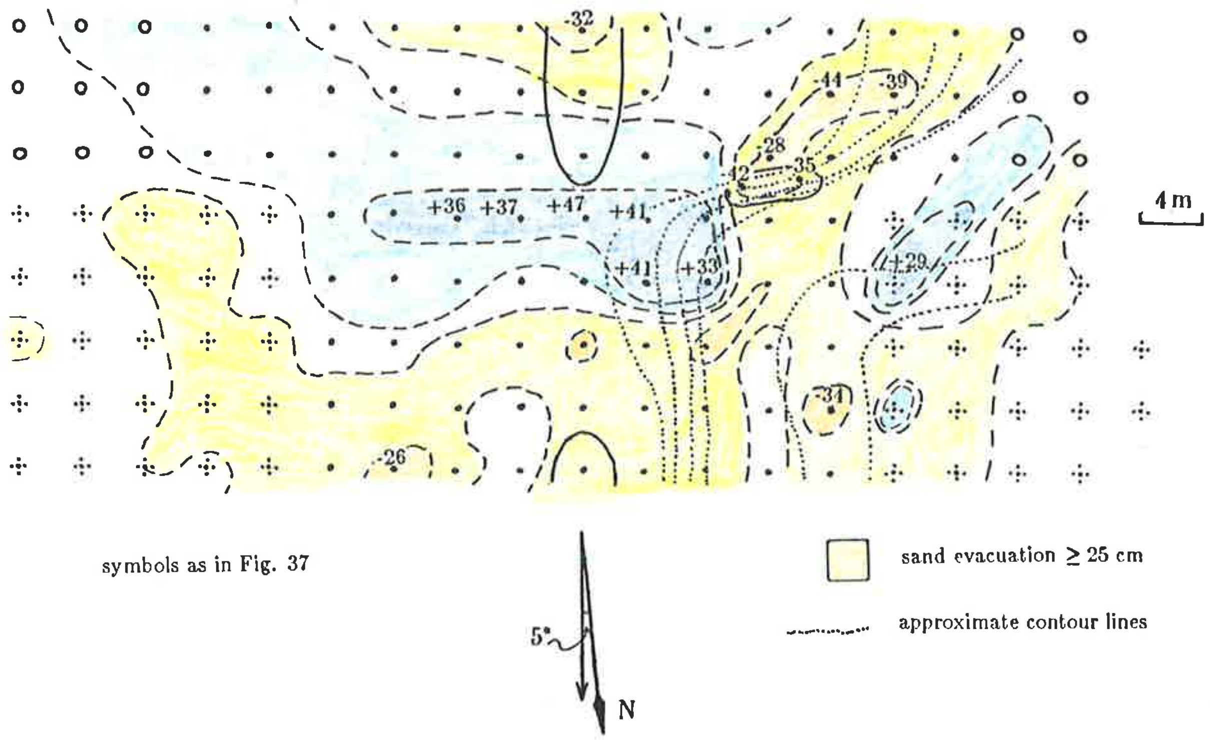

Figure 54. Deposition/erosion pattern over the study site for December 24, 1982 (8:30 AM) to February 11, 1983 (6:30 AM). Southeasterly winds believed to have prevailed during the observation interval.

Plan

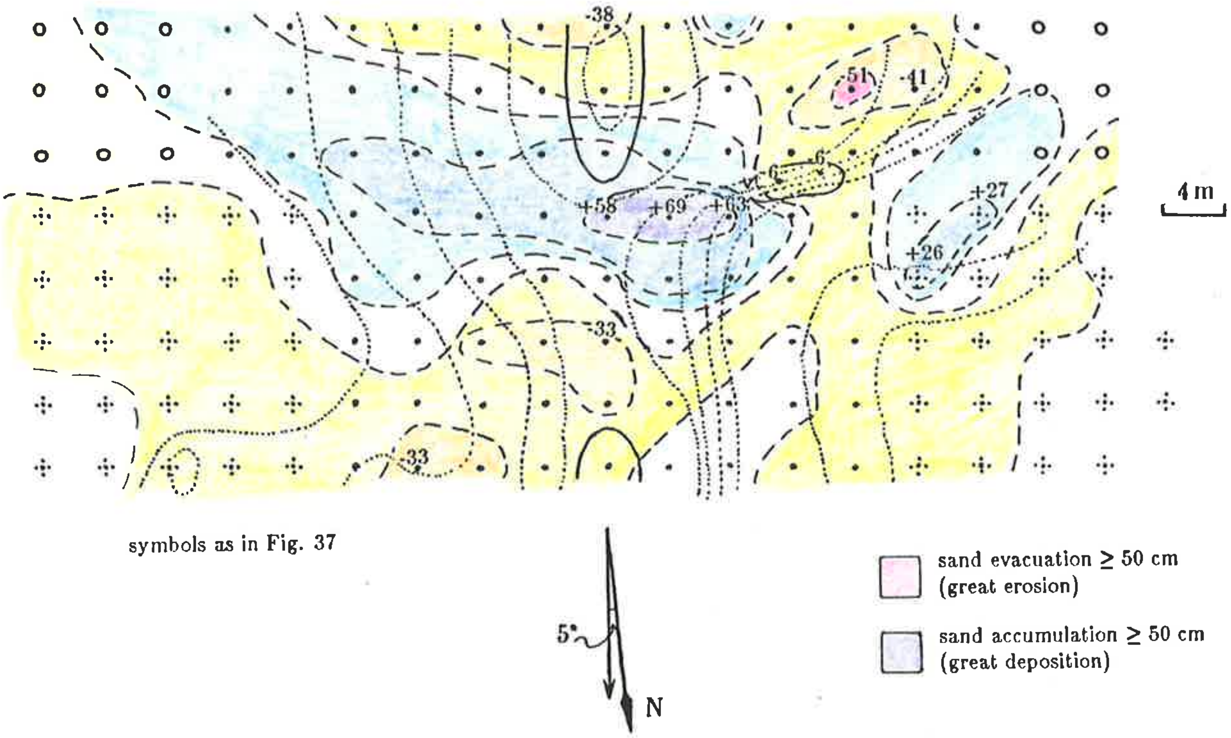

Figure 55. Deposition/erosion pattern over the study site for December 14, 1982 (3:15 PM) to February 11, 1983 (6:30 AM). South southeasterly winds believed to have prevailed during the observation interval.

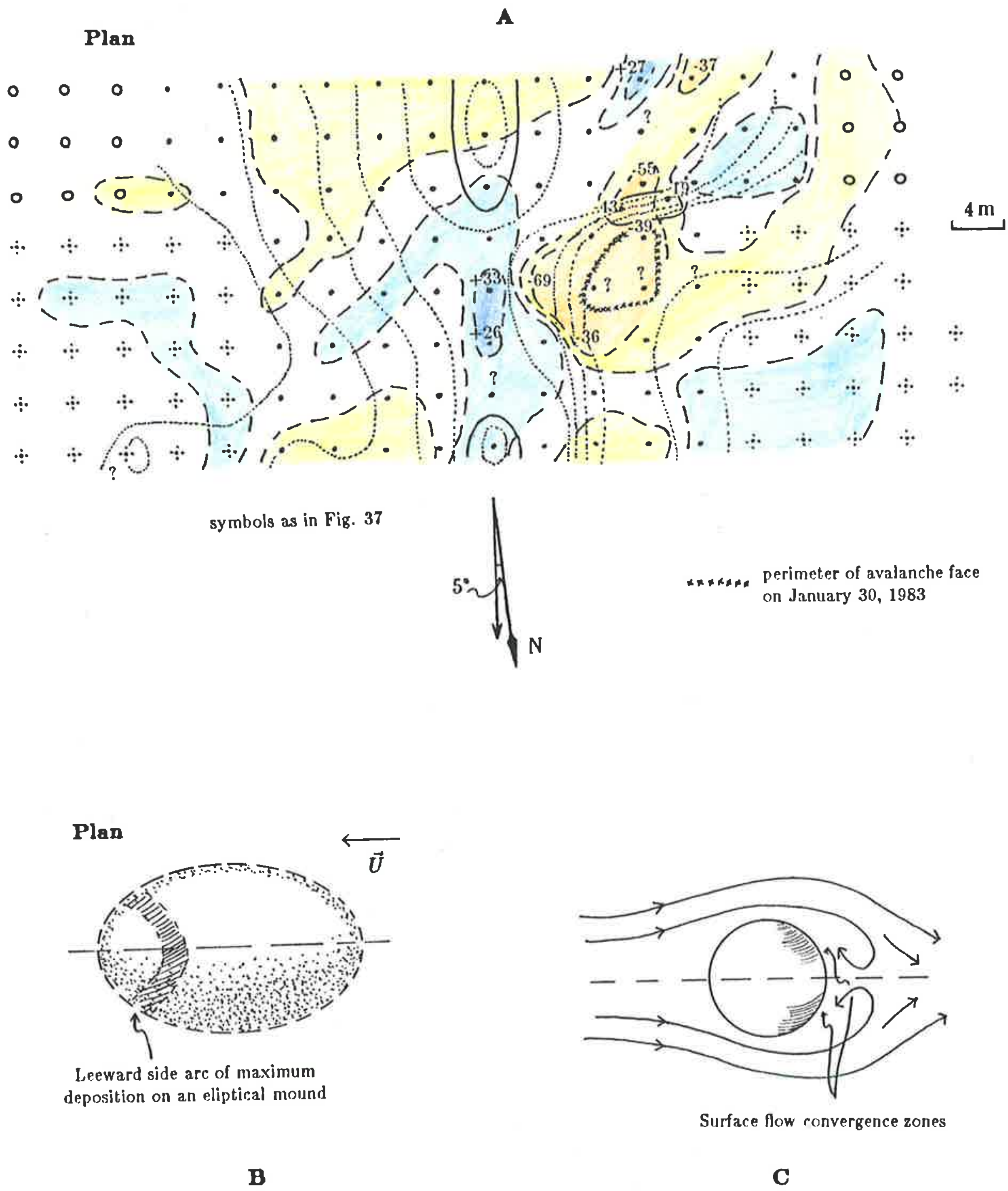

Figure 56. A) Deposition/erosion pattern over the study site for February 11, 1983 (6:30 AM) to April 10, 1983 (12:40 PM). The distinct deposition band oriented more or less orthogonally with respect to the contours just east of the crest is interpreted to be the result of flow separation to leeward of the elliptical summit during southerly winds. This deposition band is thought to be similar to the leeward side deposition arc that may develop on elliptical mounds during longitudinal flow (B). Flow over an elliptical mound may be likened to flow over half a sphere. Flow separation and surface flow convergence occur to leeward (C). Note that ?'s appear beside points where the stakes were lost sometime during the observation interval.

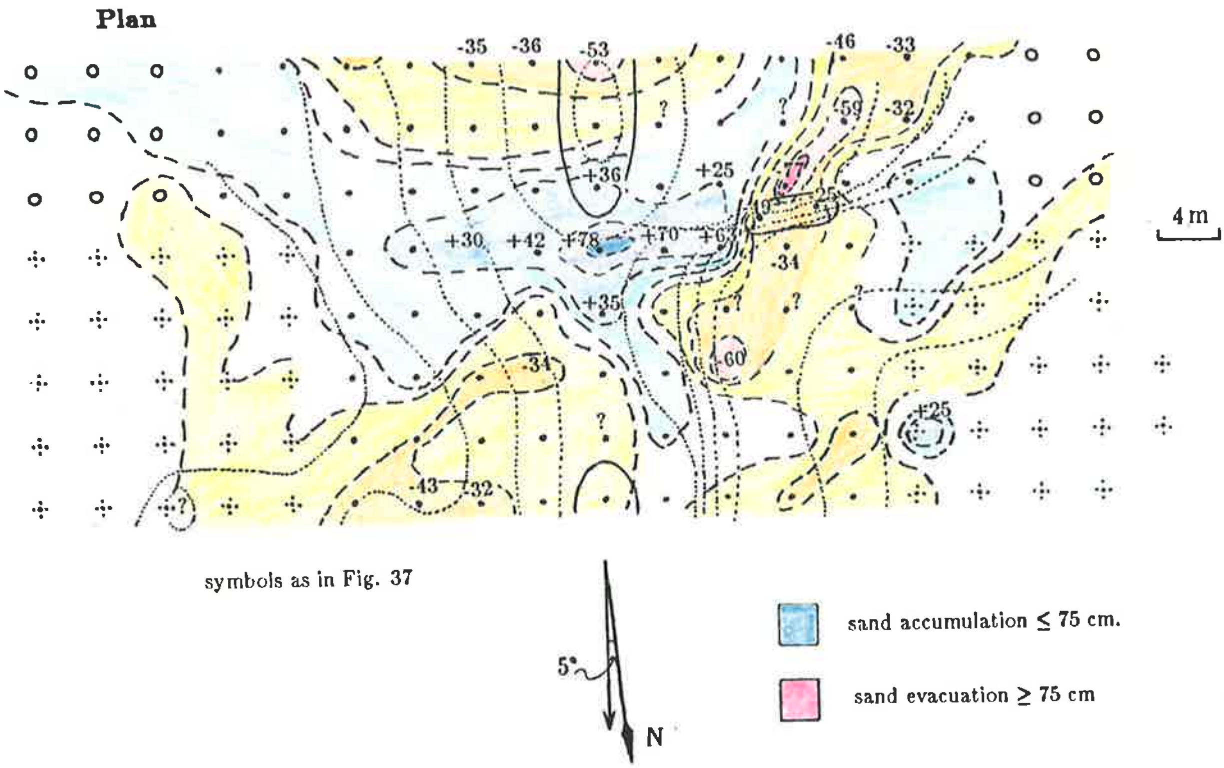

Figure 57. Deposition/erosion pattern over the study site for December 14, 1982 (3:15 PM) to April 10, 1983 (12:40 PM). South and southeasterly winds believed to have prevailed during the observation interval.

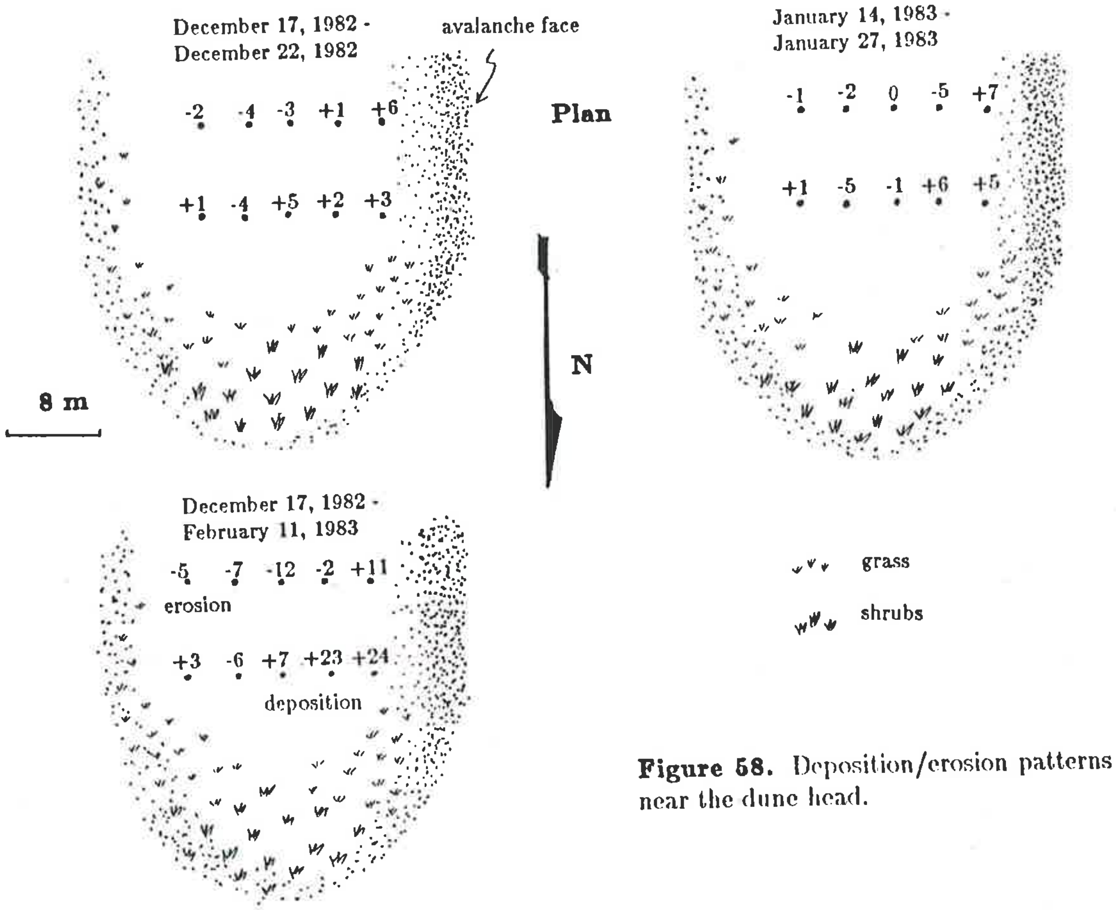

Figure 58. Deposition/erosion patterns near the dune head.

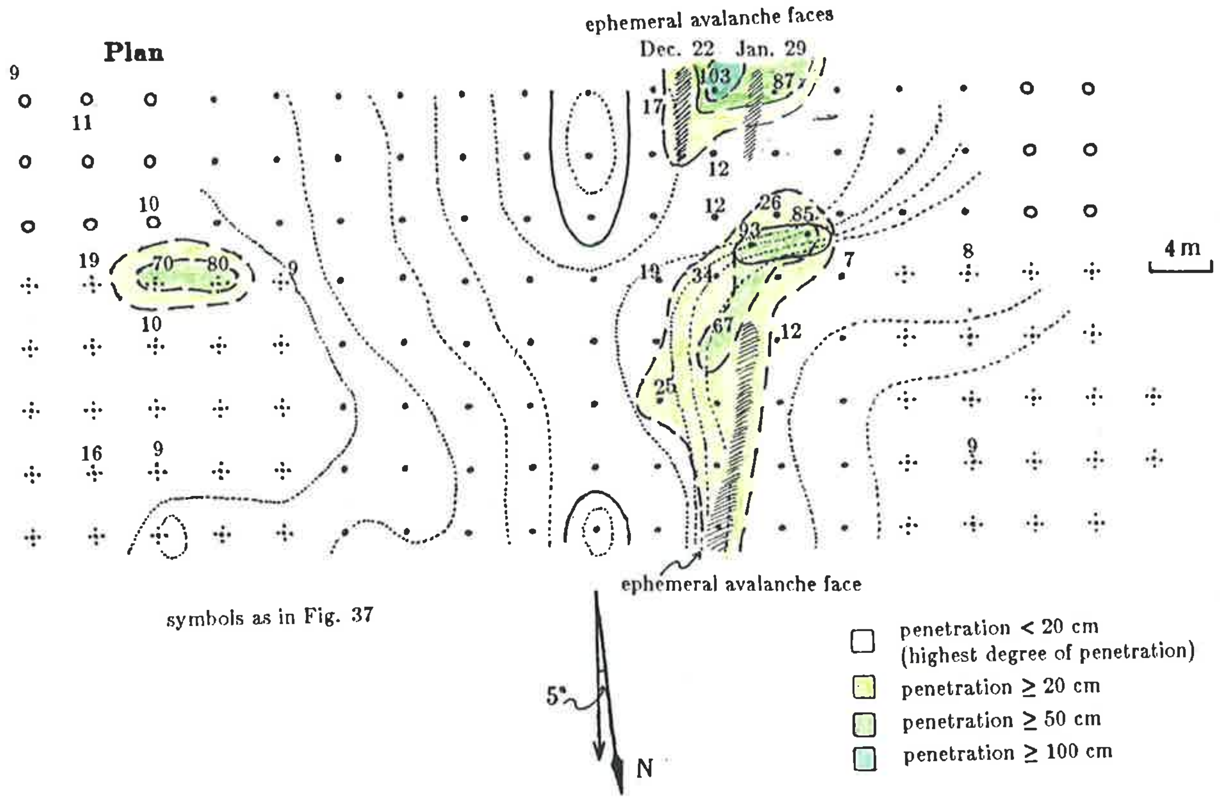

Figure 59. Firmness of study site surface as gauged by penetration pattern. Penetrometer readings taken on December 22, 1982.

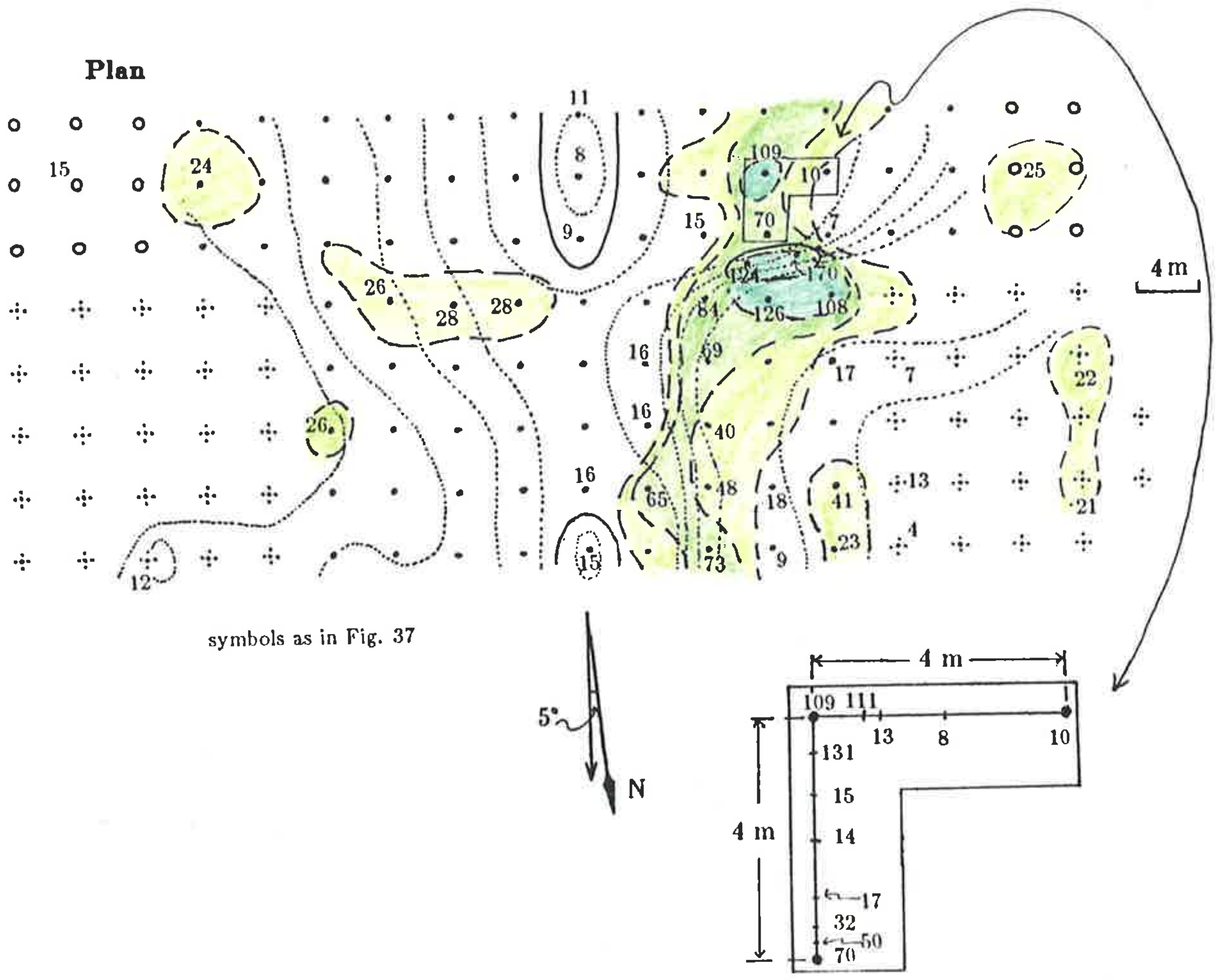

Figure 60. Firmness of study site surface on January 30, 1983.

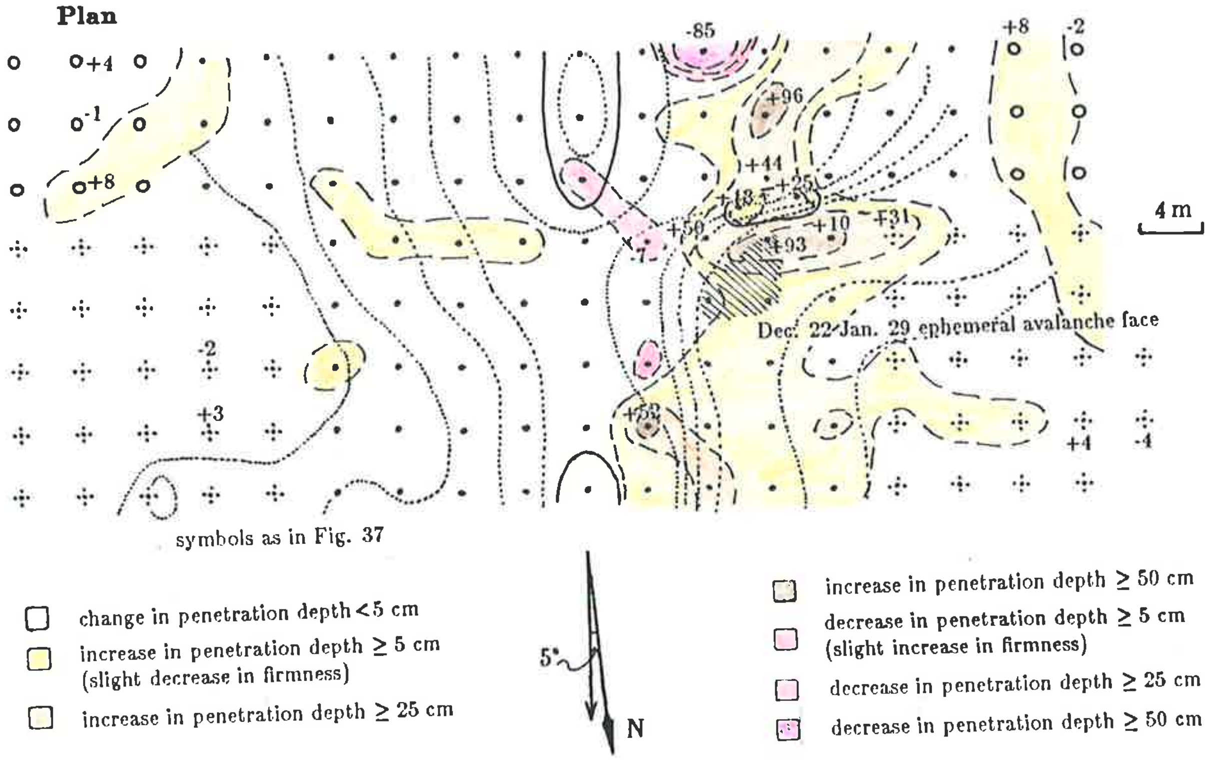

Figure 61. Change in firmness of the study site surface as gauged by change in penetration. Assessment period is from December 22, 1982 to January 30, 1983.

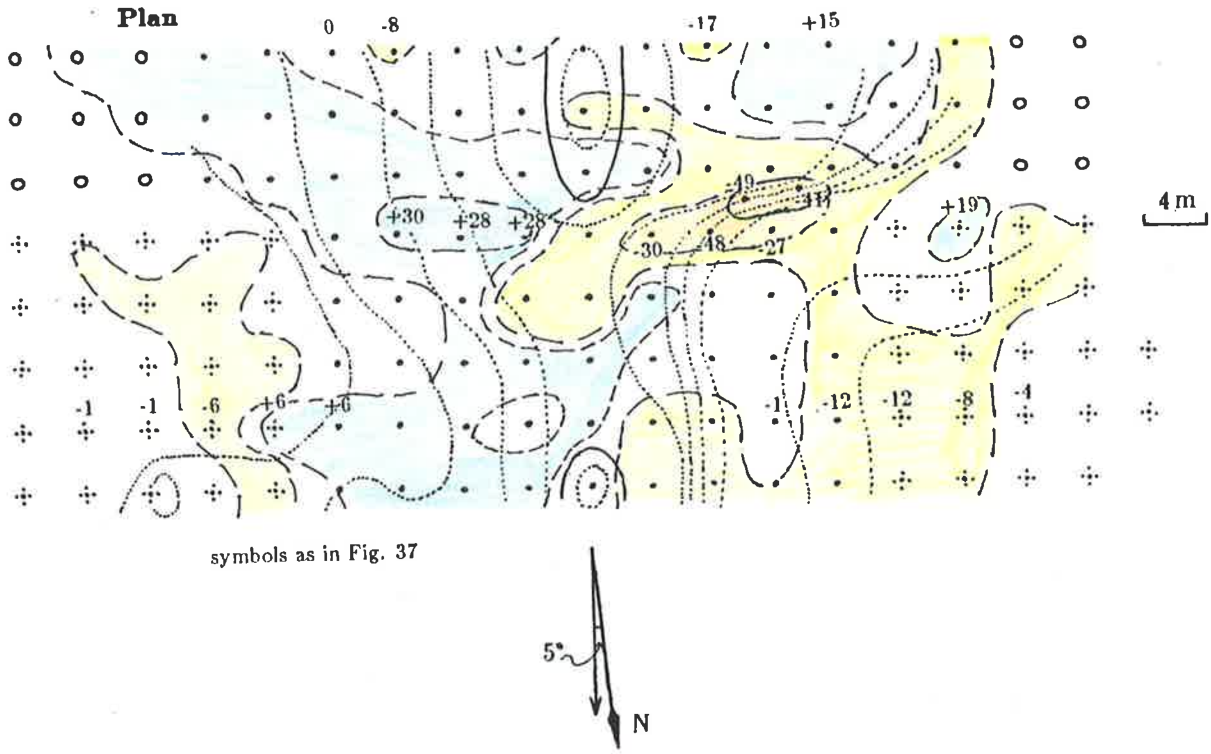

Figure 62. Deposition/erosion pattern over the study site for December 22, 1982 (9:00 AM) to January 30, 1983 (1:55 PM). East to eastsoutheasterly winds believed to have prevailed during the observation interval.

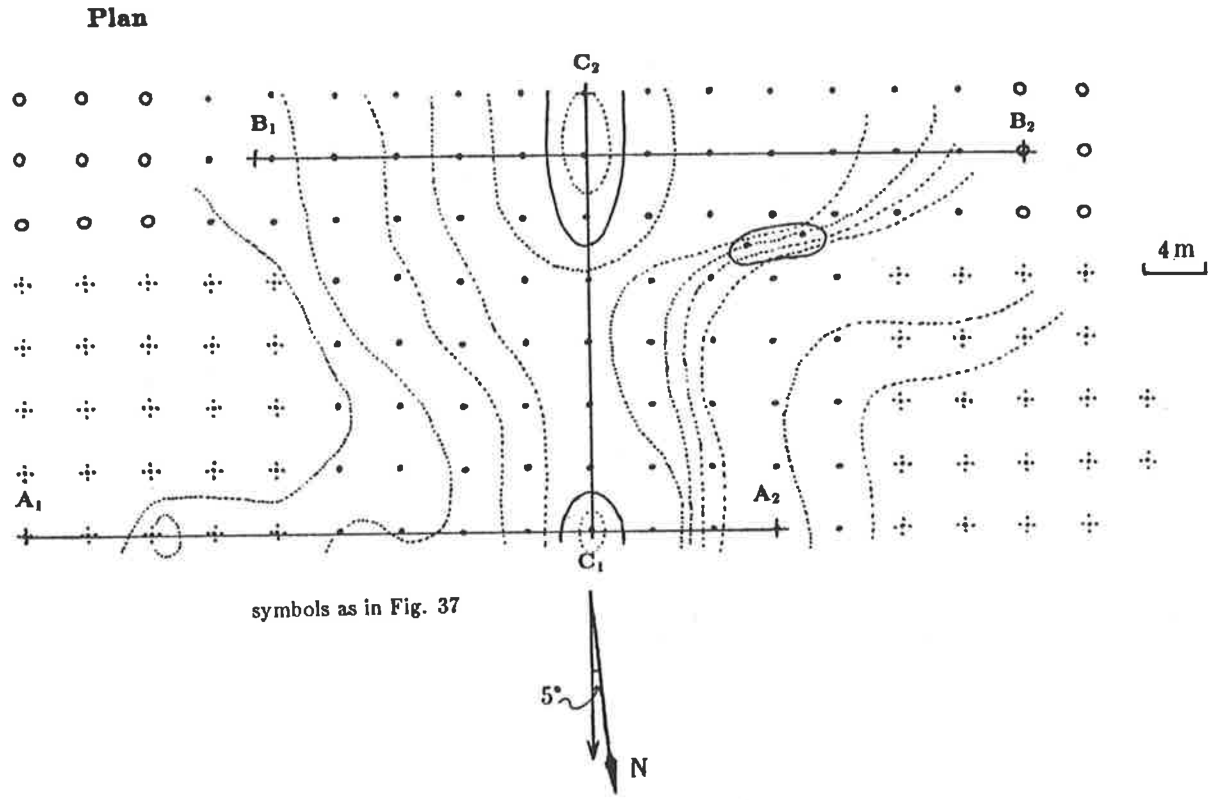

Figure 63. Lines along which topographic change was monitored (Fig.s 64, 65 and 66).

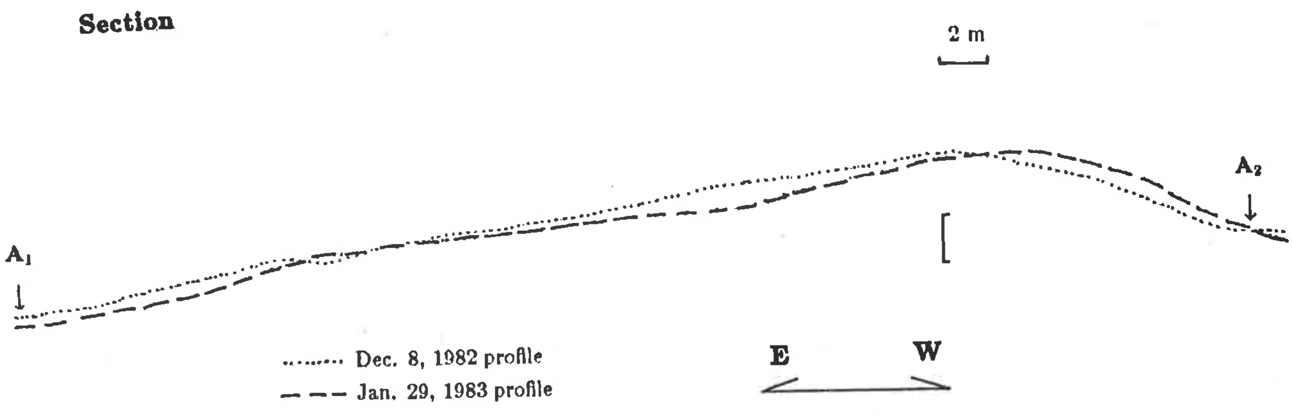

Figure 64. Topographic change in the study site northern perimeter between December 8, 1982 and January 29, 1983.

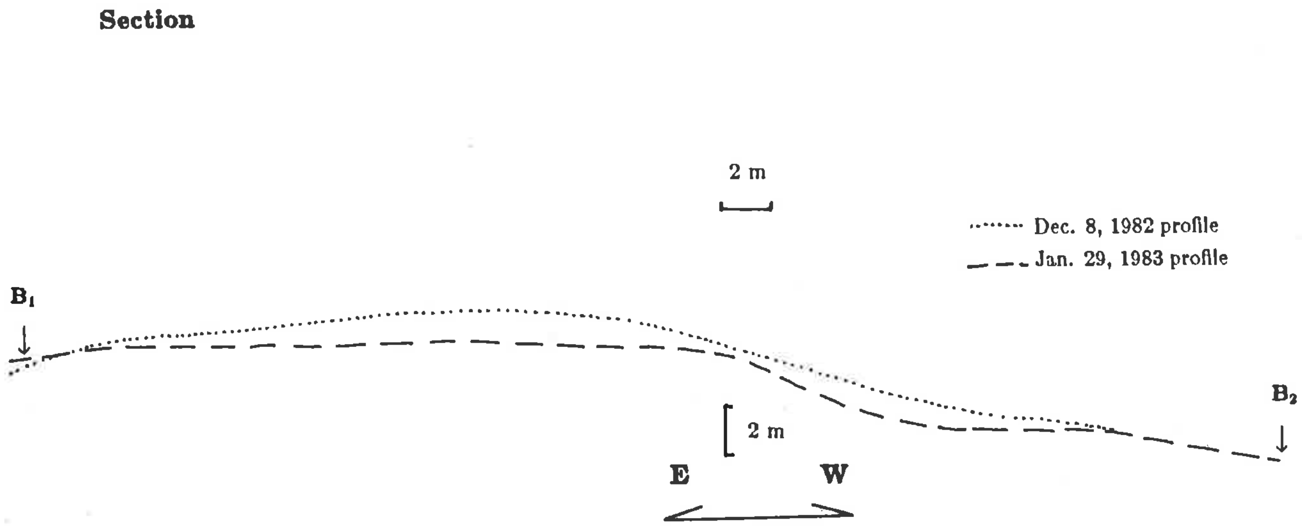

Figure 65. Topographic change in the study site southern perimeter between December 8, 1982 and January 29, 1983.

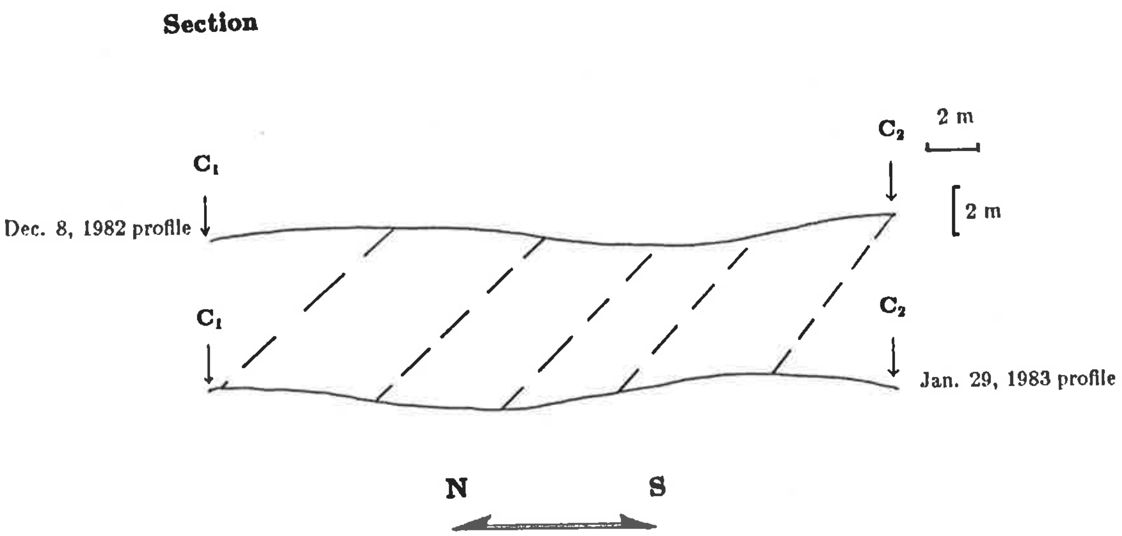

Figure 66. Topographic change in the crestal axis between December 8, 1982 and January 29, 1983. Note that the crestal topography seems to translate with minor distortion. In a southward migration of ~ 6 m, the separation between the two summits increased by only ~ 1 m.

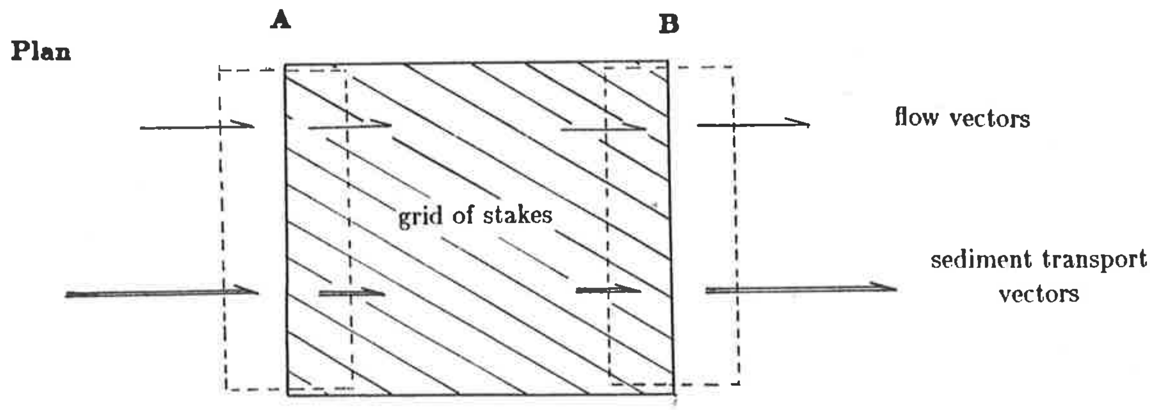

Figure 67. A) Flow and sediment transport convergence in a zone centered on the windward perimeter of the grid of stakes resulting in deposition. B) Flow and sediment transport divergence in a zone centered on the leeward perimeter of the grid of stakes resulting in erosion. Note that while flow changes linearly, transport changes cubically.

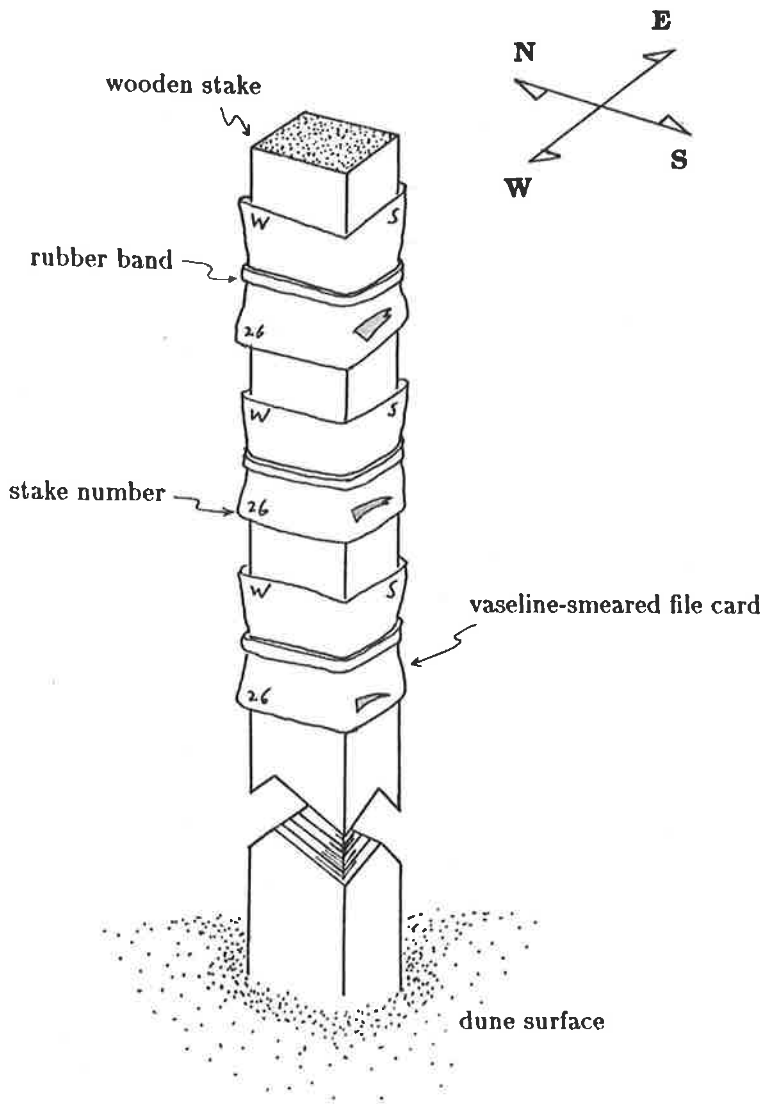

Figure 68. Stake with vaseline-covered file cards for sand collection during saltation.

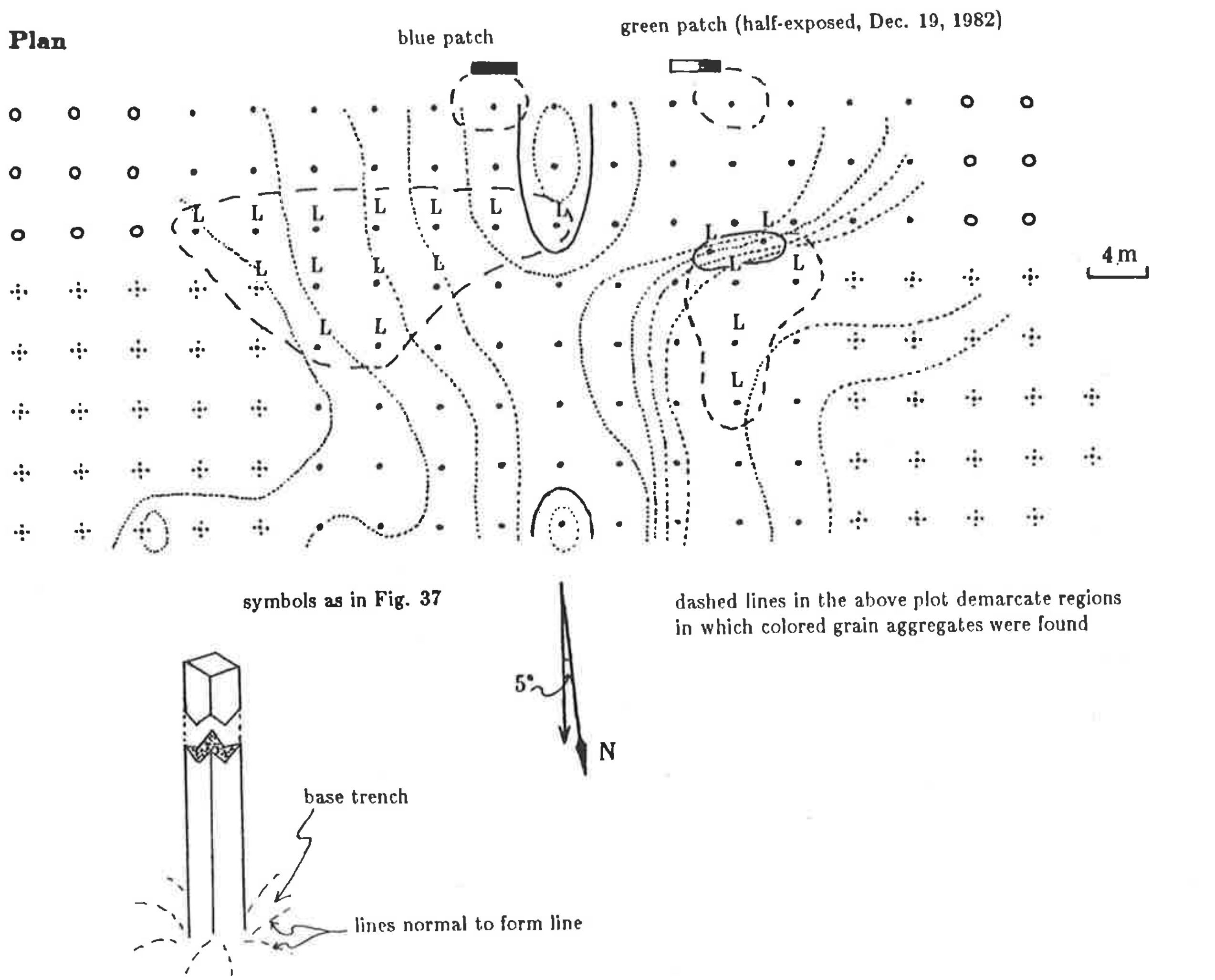

Figure 69. Distribution of colored grain aggregates over the study site on December 16, 1982. Stakes with colored aggregates in the trenches excavated around their bases are marked "L". The original colored sand patches were ~ 0.5 m × ~ 3 m × ~ 0.0015 ± 0.005 m.

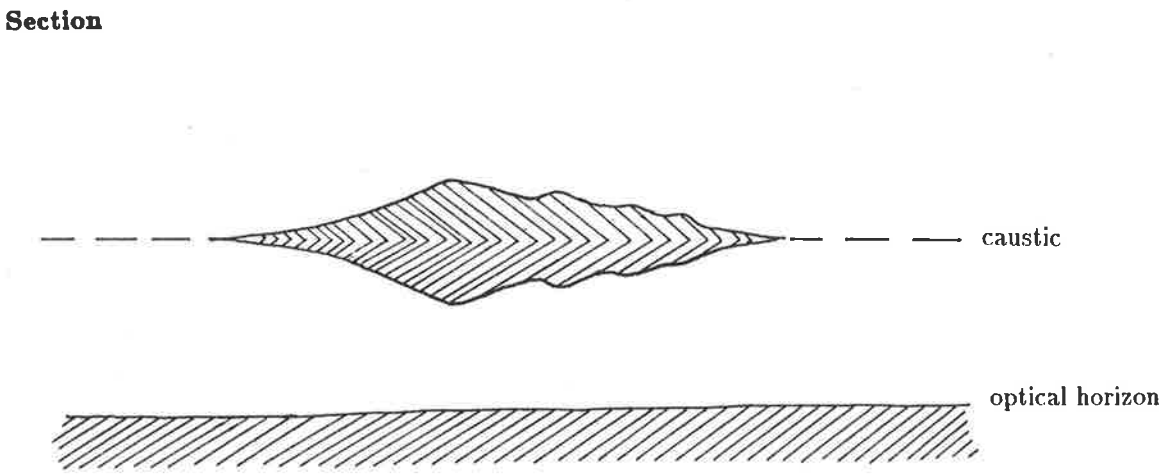

Figure 70. Inferior mirage of a mountain.

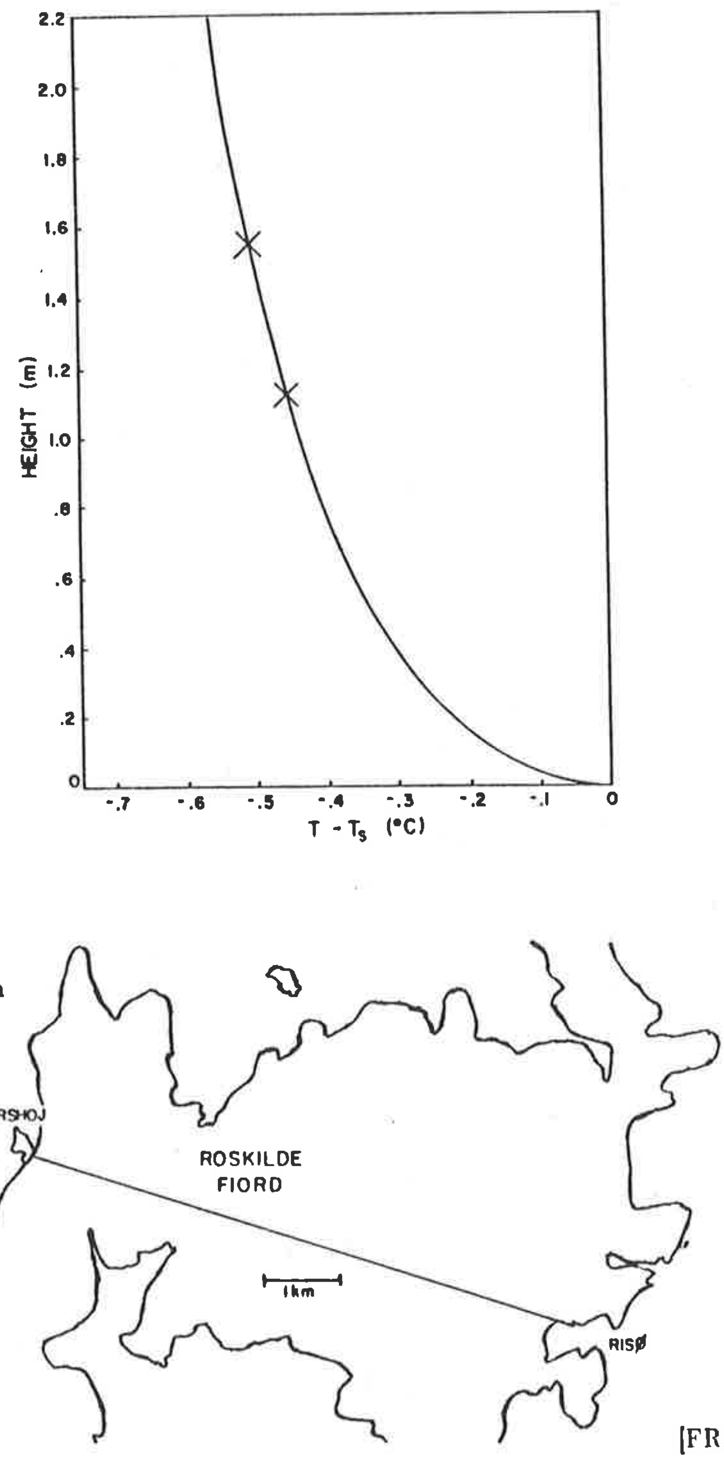

[FRASER, 1979]

Figure 71. A) "Optically deduced profile for Gershoj deduced from two different heights (marked with x's) plotted on top of each other to give a single line." B) "A map of a portion of Roskilde Fiord in Denmark. The observation point was on the shore at Risø." The target Gershoj (7220 m) is shown.

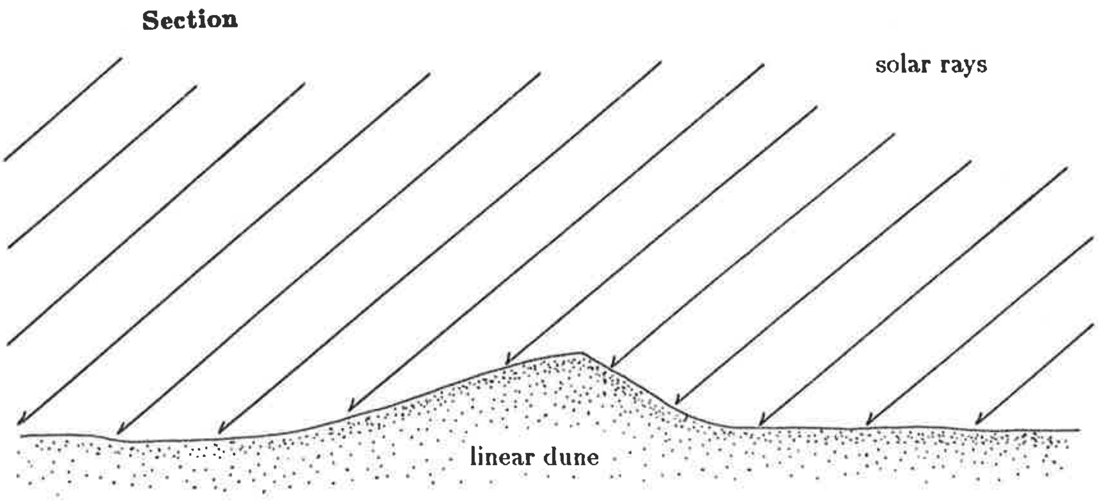

Figure 72. The comparative rates of solar radiative heating of a linear dune's flanks depend upon the orientation of the incoming solar rays with respect to the slopes of the dune flanks. This is ultimately determined by the position in the sky of the sun.

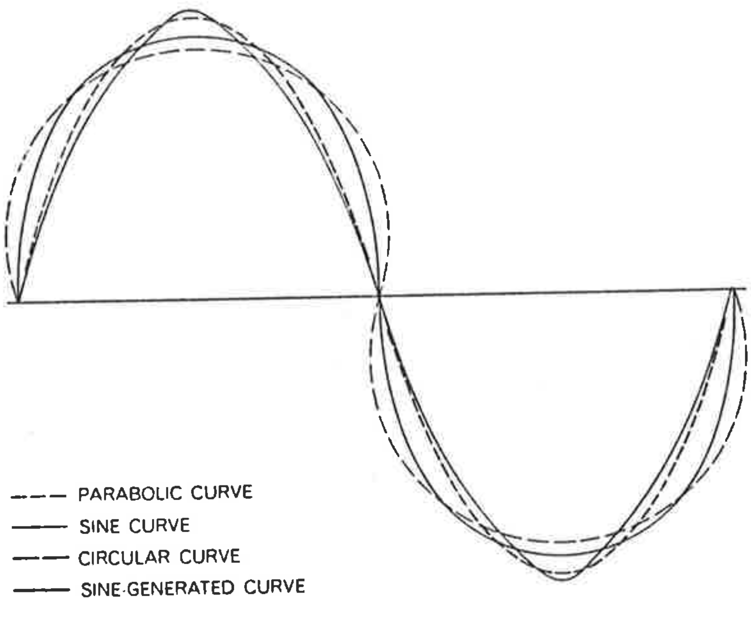

Figure 73. "Variation in curvature of a sine-generated curve is less than for any other regular geometric curve. This means that when the changes in direction are tabulated for small distances along several hypothetical meanders, the sums of the squares of the changes in direction will be less for a sine-generated curve than for any other curve. The changes in direction were measured in degrees over 10 equally spaced intervals for each of the four curves depicted here. When the squares of these changes were summed, the following values were obtained: parabolic curve, 5,210; sine curve, 5,200; circular curve, 4,840; sine-generated curve, 3,940. The four curves are equal in length, wavelength and sinuosity."

Plan

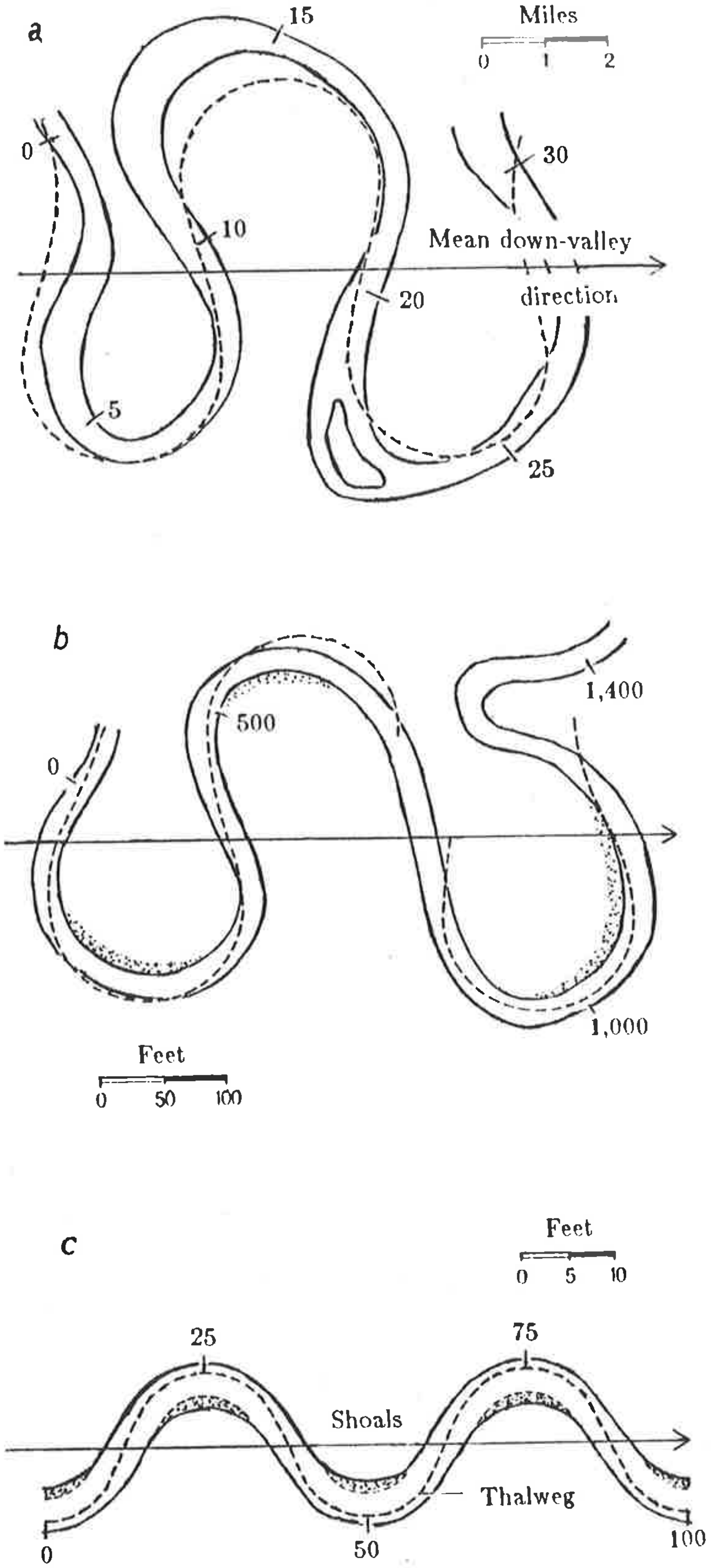

[LEOPOLD and LANGBEIN, 1966]

Figure 74. Above are shown "segments of two typical meandering streams, the Mississippi River near Greenville, Miss. (a), and Blackrock Creek in Wyoming (b), as well as a segment of an experimental meander formed in a homogenous medium in the laboratory (c)." Dashed lines trace the correspondent sine-generated curves.

Plan

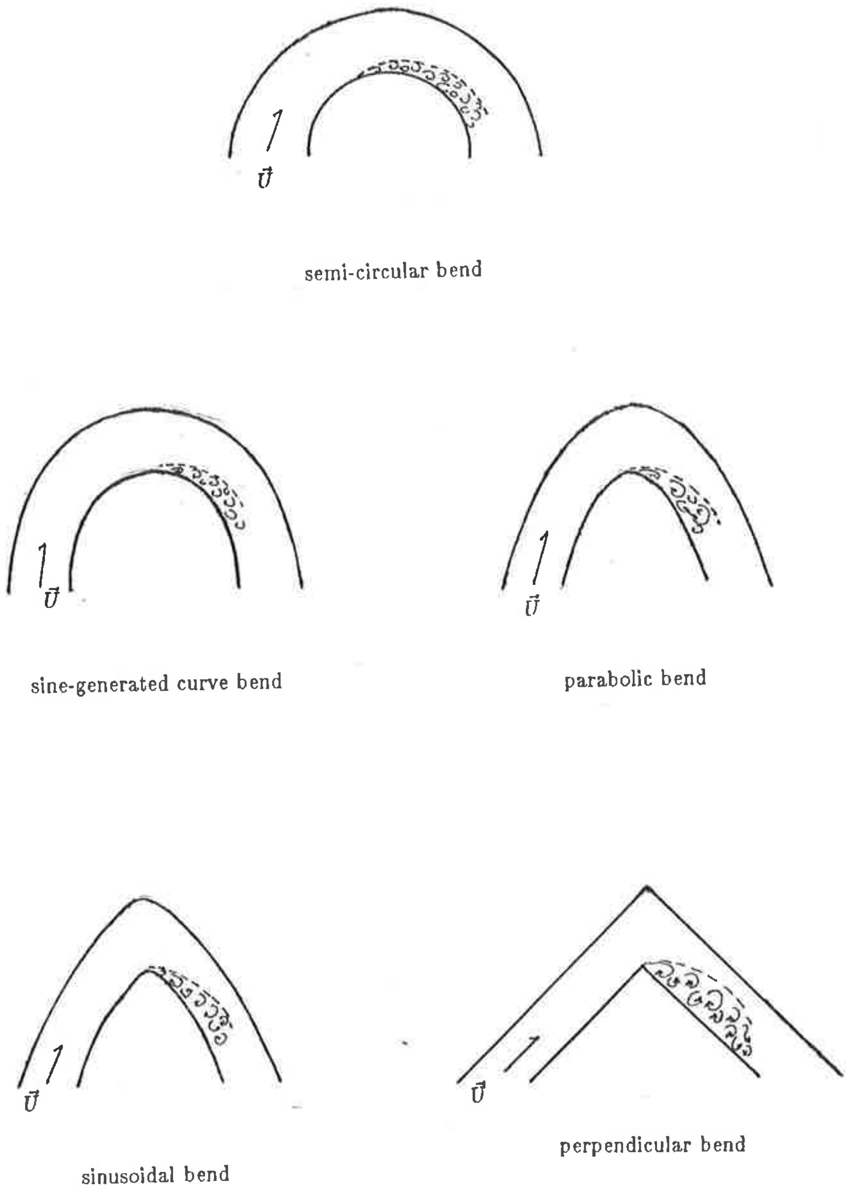

Figure 75. Asymmetry of turning flow and the associated turbulence are minimalized in a channel bend conforming to a sine-generated curve.

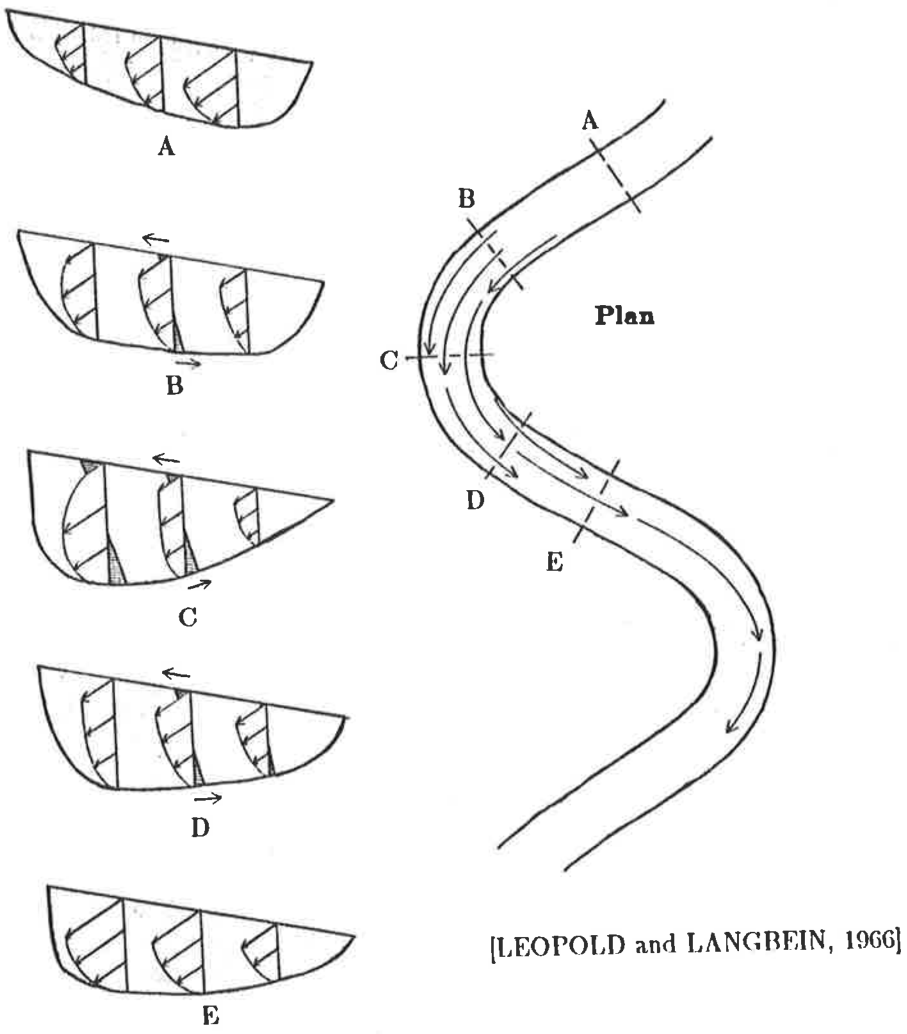

Figure 76. "Idealized flow pattern of a typical meander." Vertical velocity profiles are provided for five sections at various points along the first bend (A, B, C, D and E). Note the counterclockwise rotation of the flow rounding this bend. Flow rotation would be clockwise around the subsequent bend."

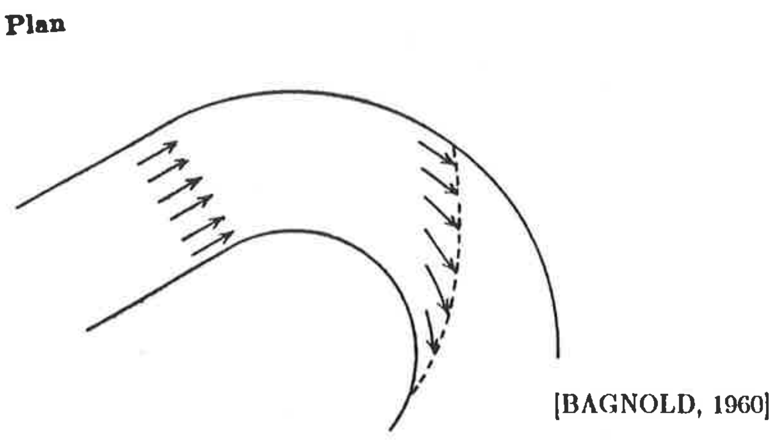

Figure 77. "Idealized diagram of shearing motion between water filaments in a pipe bend if transverse flow were prevented."

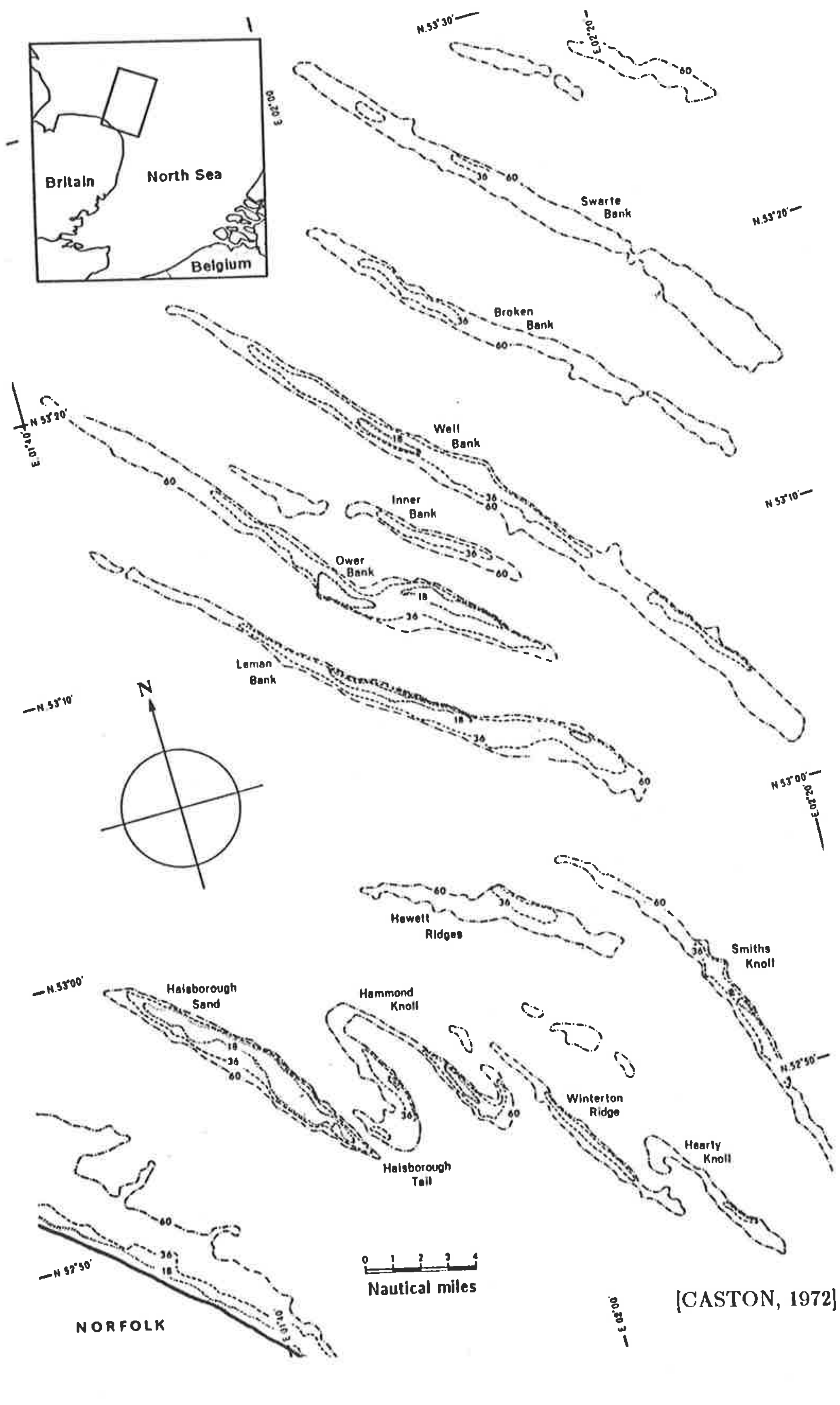

Figure 78. Map of "linear sand banks of the Norfolk Banks area. Isobaths at 18, 36 and 60 ft." Inset shows location of plotted area.

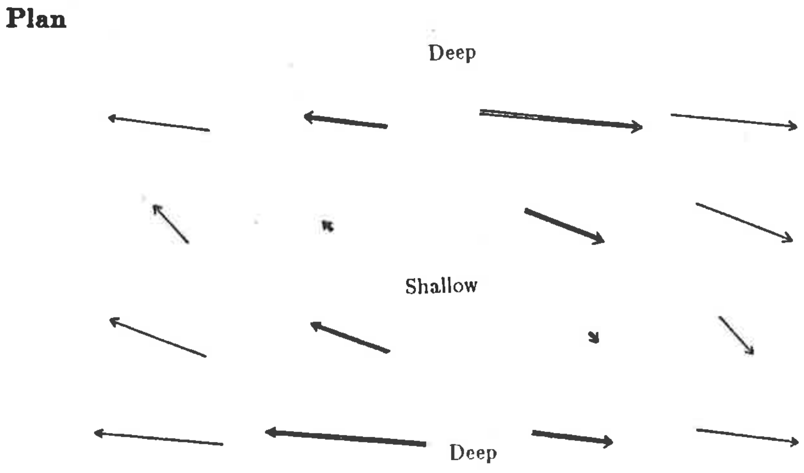

[HUTHNANCE, 1982a]

Figure 79. Flow and sediment transport deflection in the shallow water over the linear sand bank.

A

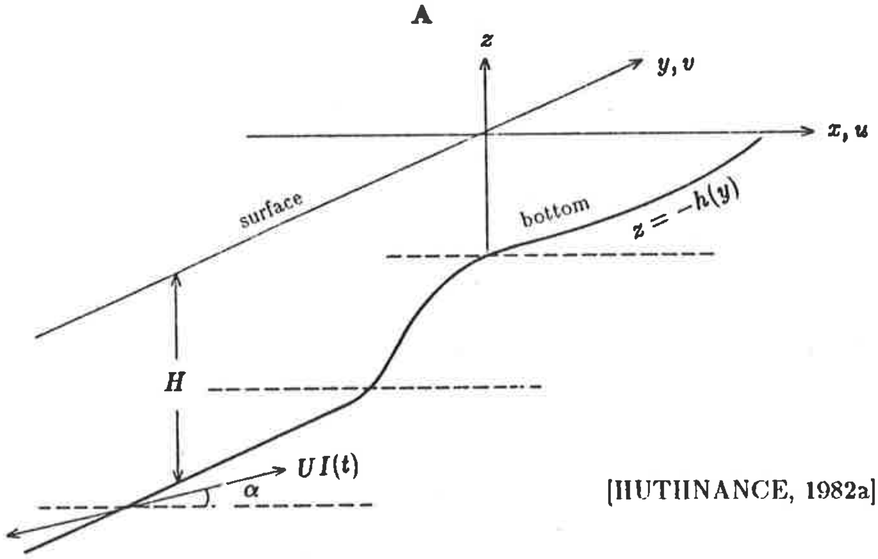

[HUTHNANCE, 1982a]

B

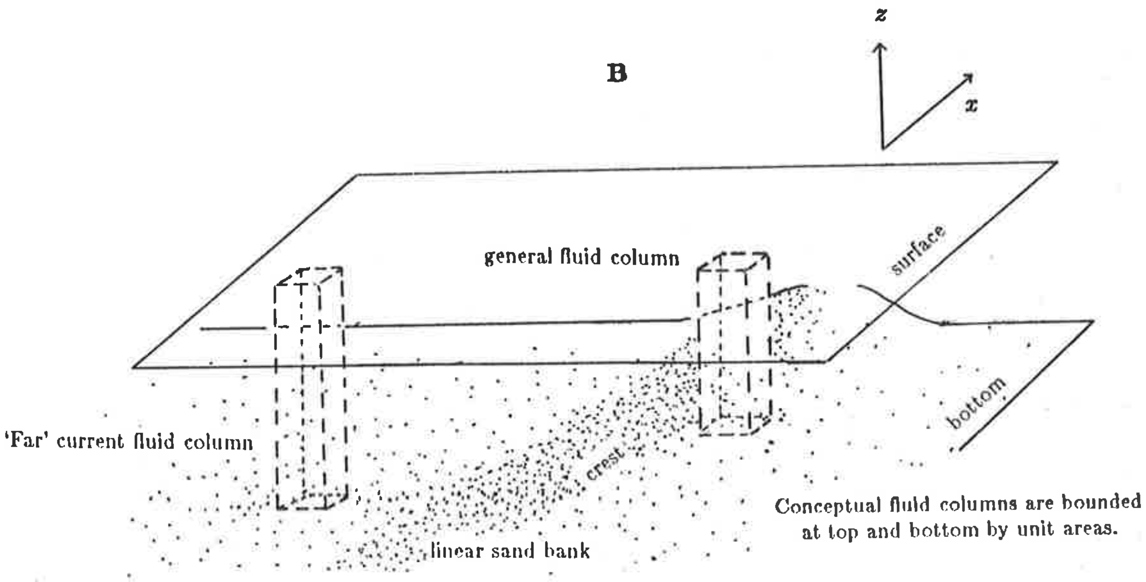

Figure 80. A) Axes of topography. B) Momentum is conserved over the sand bank. The 'far' current momentum ($\rho HUI(t)$) must equal the fluid column momentum (ρhu) over the sand bank. That is, $HUI(t) = hu$.

Plan

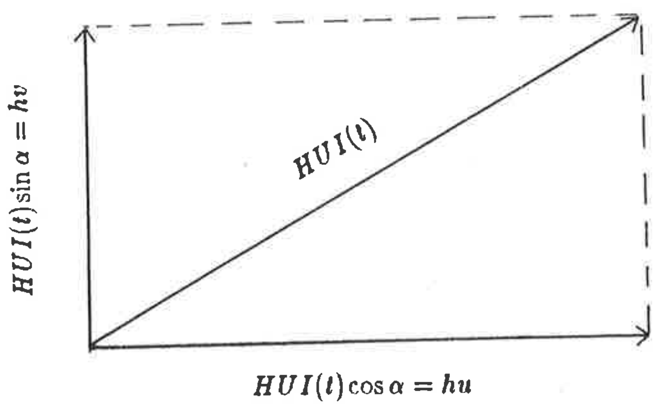

Figure 81. Momentum vector and its components.

Section

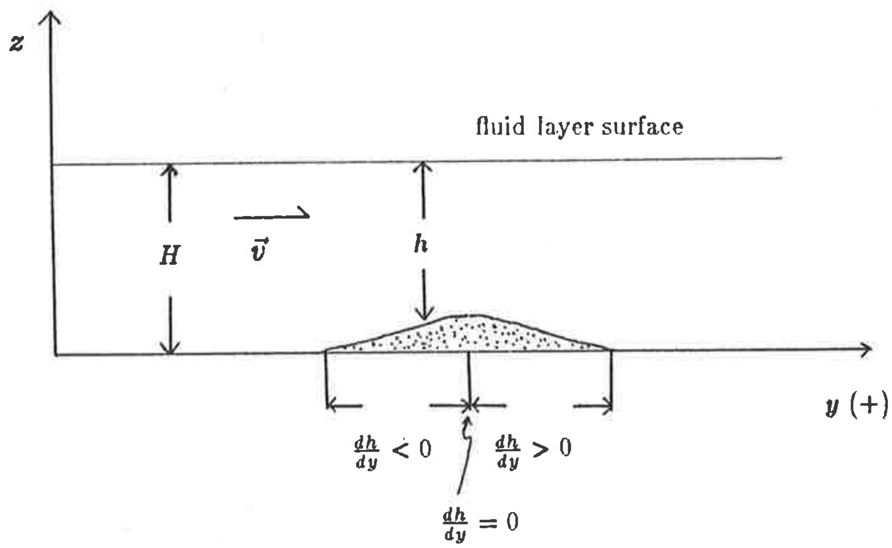

Figure 82. The relationship between the parameters h and $\frac{dh}{dy}$ and the bottom topography.

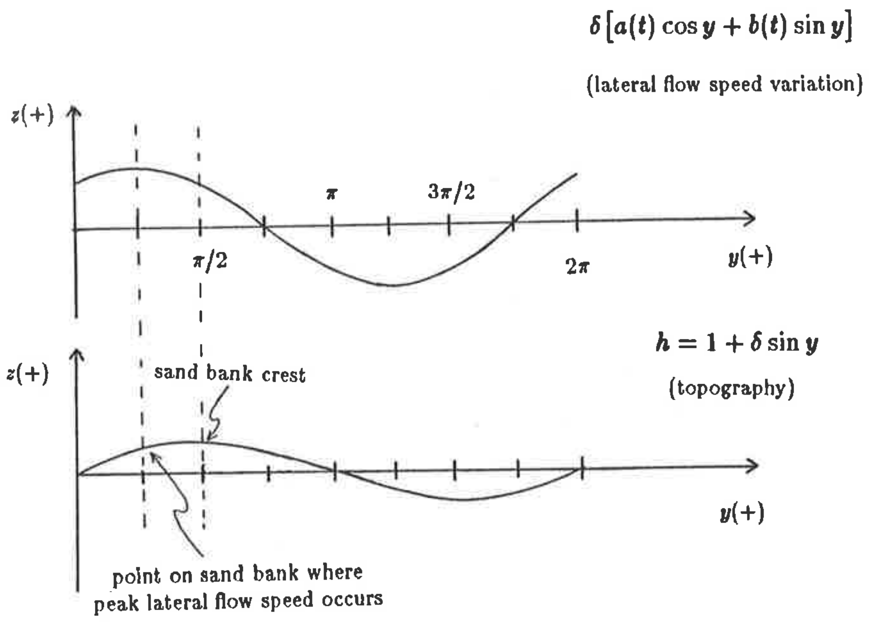

Figure 83. The relationship between lateral flow speed variation and topography.

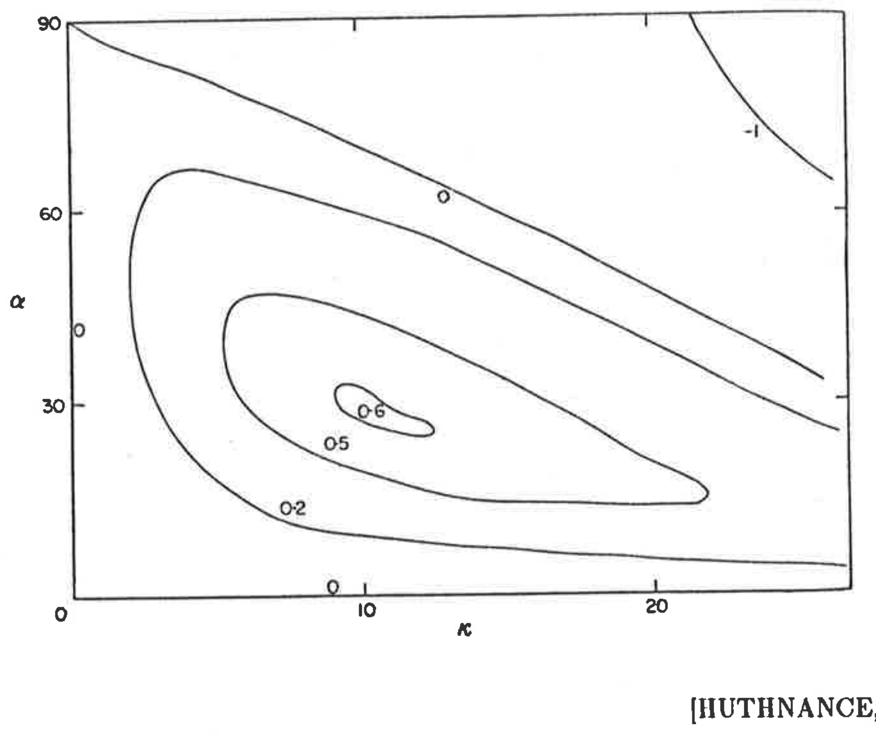

[HUTHNANCE, 1982a]

Figure 84. "Contours of growth rate $\sigma(\kappa, \alpha)$ as a multiple of $SU^2Fn/2(1-p)gH$ when $f = 0$, $F = 1$, $\hat{\Lambda} = 0.005$ and $m = 2 = n$."

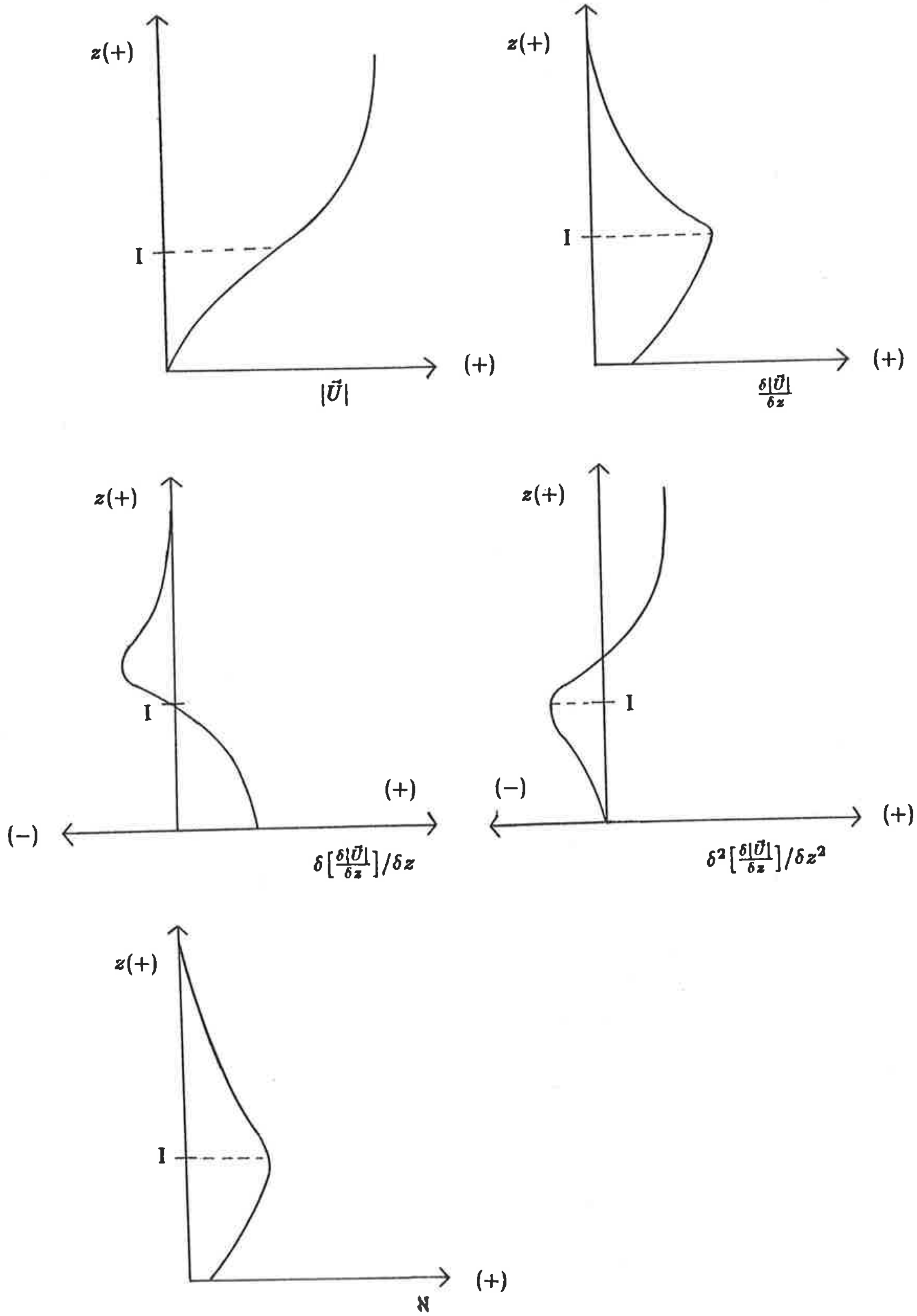

Figure 85. Inflection point vertical velocity profile (A) and vertical profiles of associated parameters (B – E). "I" indicates the inflection point, and ℵ ≡vorticity.

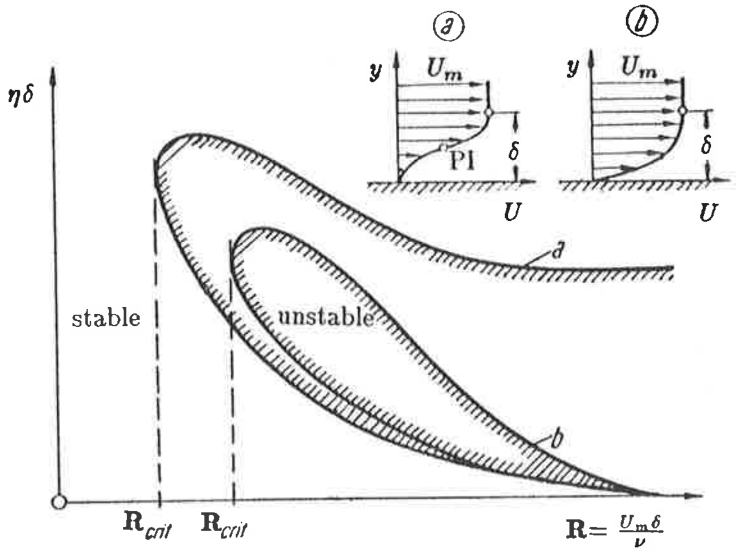

[SCHLICHTING, 1960]

Figure 86. "Curves of neutral stability for a two-dimensional boundary layer with two-dimensional disturbances (a) 'non-viscous' instability; in the case of velocity profiles of type *with* point of inflection PI, the curve of neutral stability is of type a (b) 'viscous' instability; in the case of velocity profiles of type b *without* point of inflexion, the curve of neutral stability is of type b."

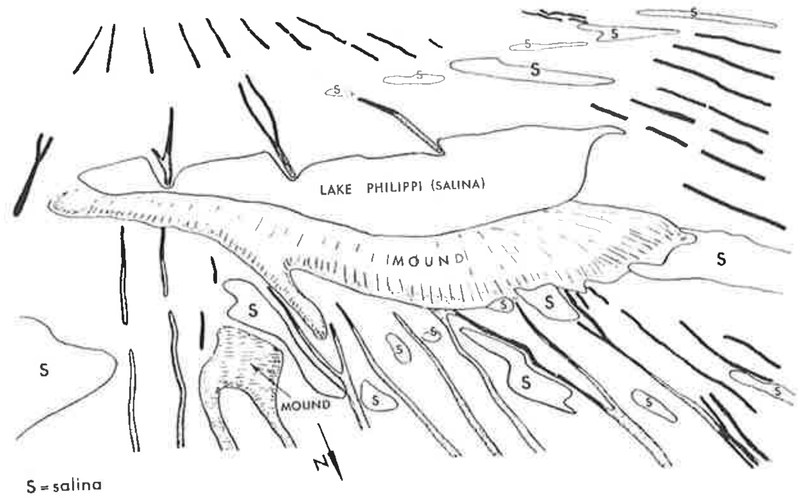

[TWIDALE, 1972]

Figure 87. "Sketch of the Lake Phillipi area, near the eastern margin of the Simpson Desert in western Queensland. Note the leeside mound some 20 km east-west, standing some 30 m above the bed of the salina, and the related dune ridges."

[TWIDALE, 1972]

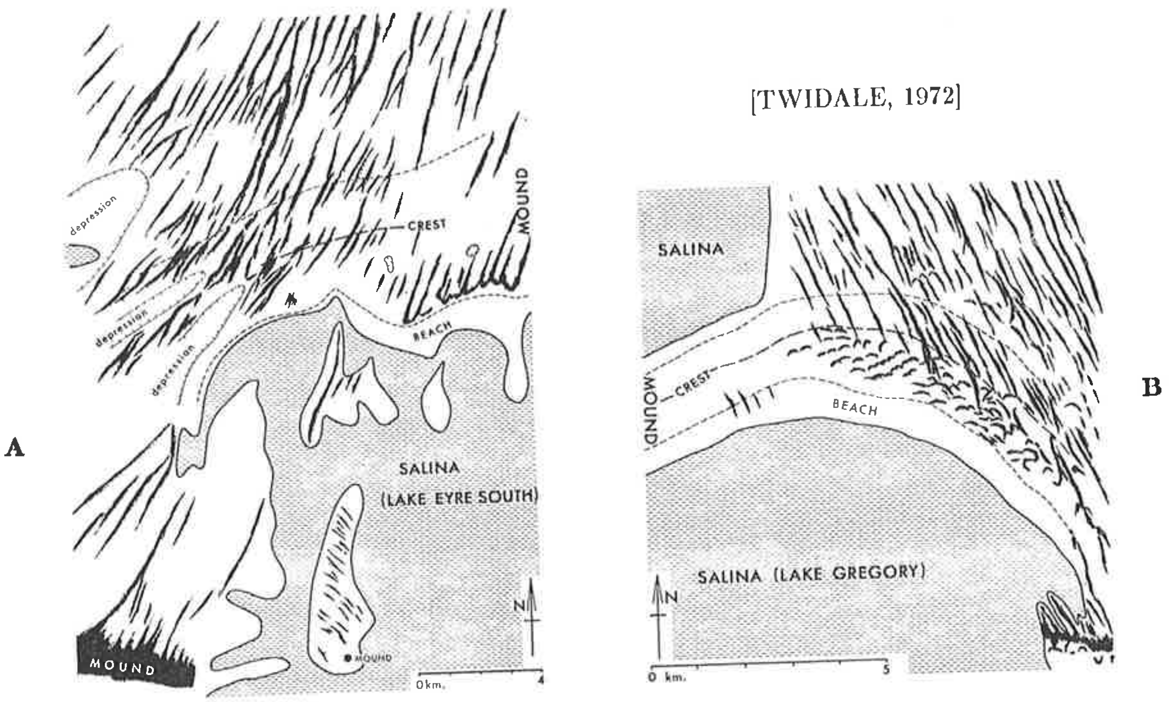

Figure 88. A) "Map of the south-western margin of Lake Eyre near Warriners Arm, showing leeside debris mound and associated dune ridges. (Drawn from air photographs)"
B) "Map of part of the northern shore of Lake Gregory showing debris mound and associated dunes. (Drawn from air photographs)"

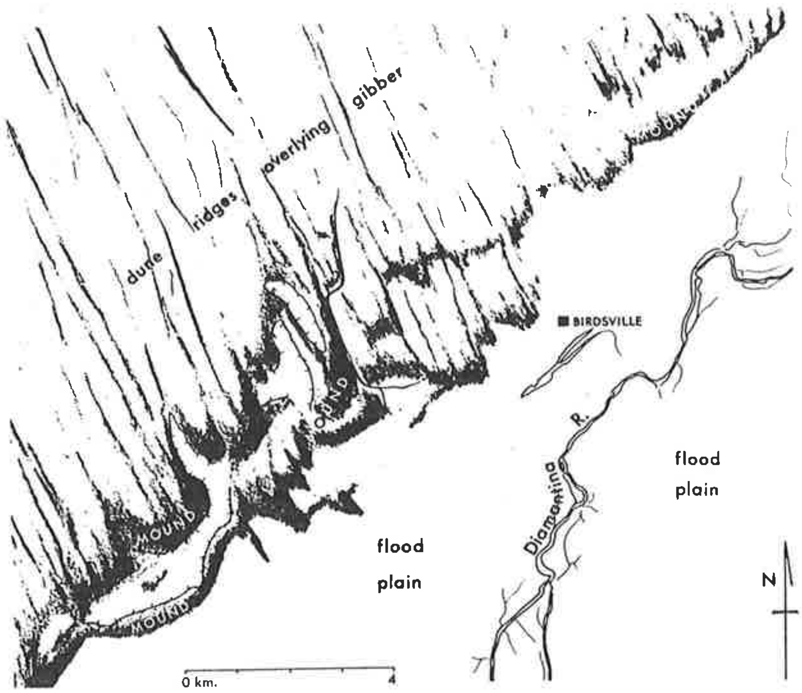

[TWIDALE, 1972]

Figure 89. "Map drawn from air photographs of the Diamantina flood plain near Birdsville, south-west Queensland, showing leeside mound and longitudinal sand ridges extending from it."

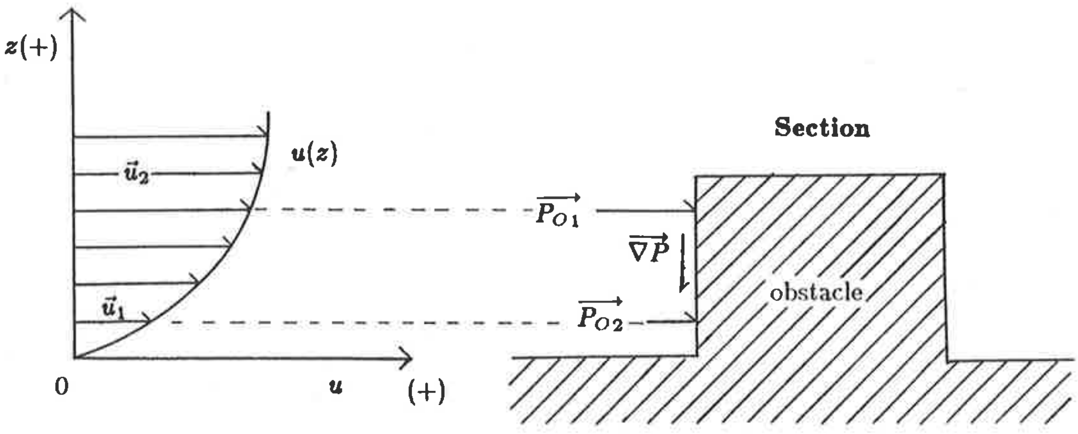

Figure 90. The vertical velocity profile for flow, the resultant stagnation pressure variation with height and the pressure gradient created over the flowward surface of an obstacle. $\overrightarrow{P_{Oi}}$ ≡the stagnation pressure vector at arbitrary level i, and $\overrightarrow{\nabla P}$ ≡the pressure gradient vector.

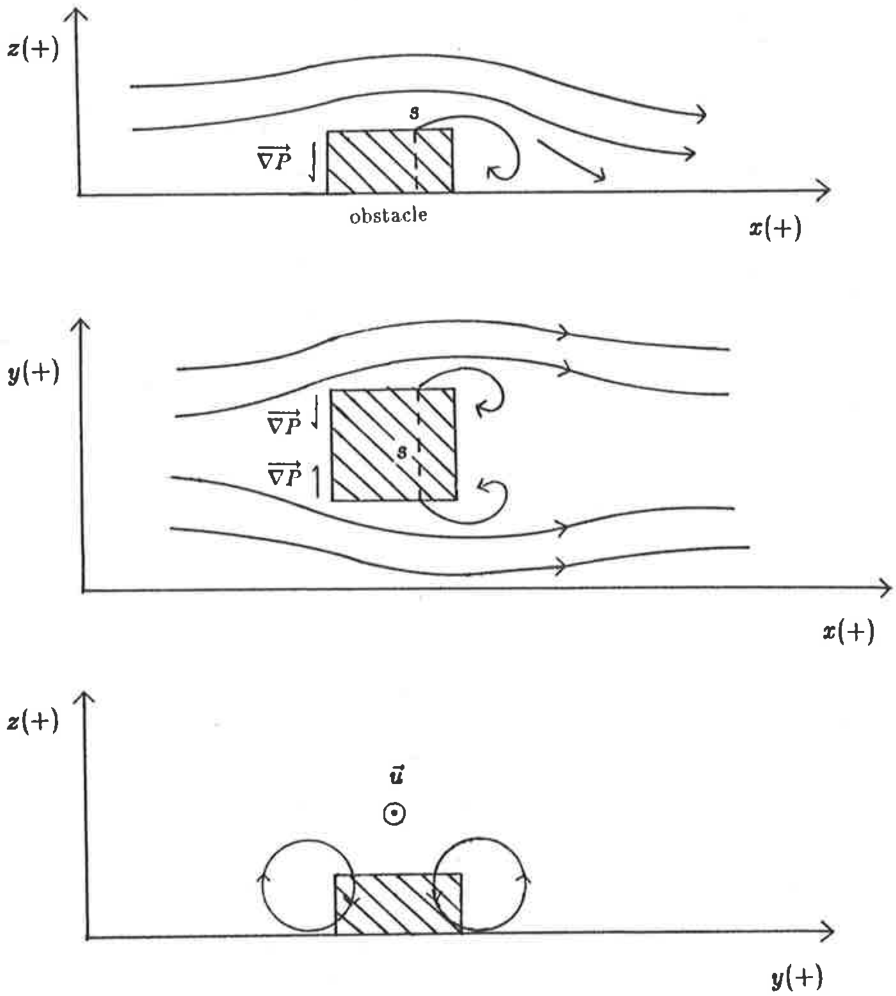

Figure 91. Pressure gradient generation of vortical flow around an obstacle. Dashed line s is the flow separation boundary.

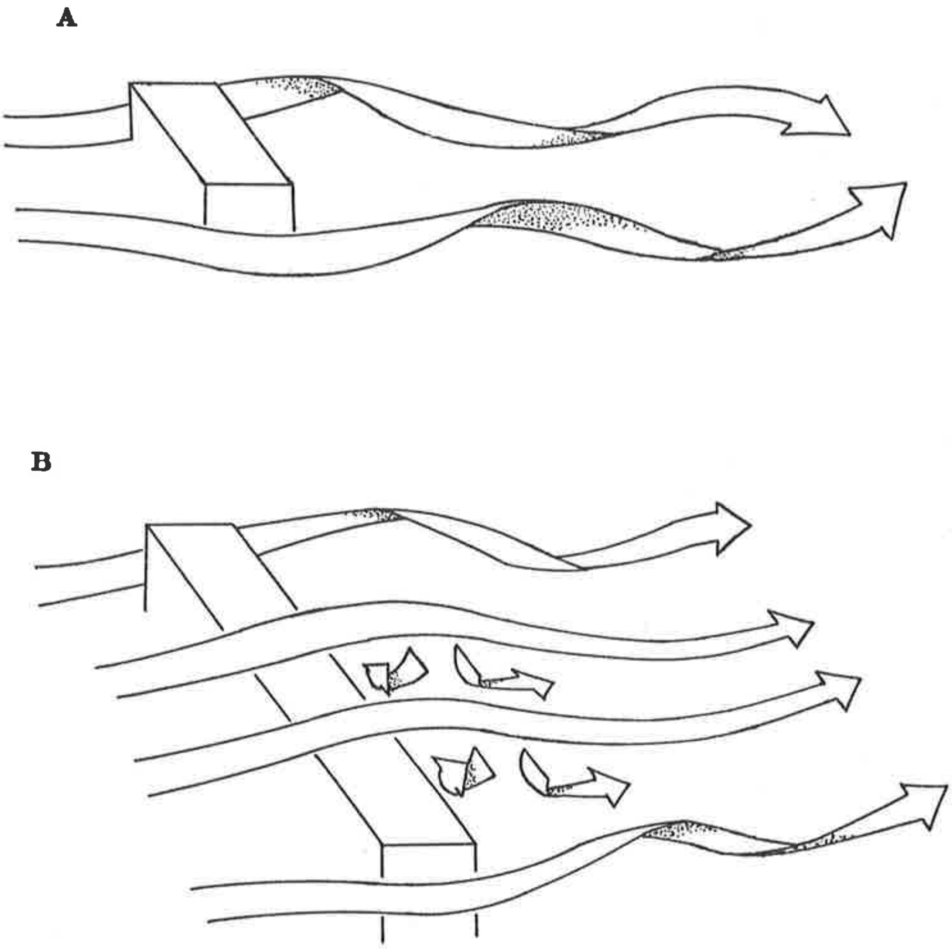

Figure 92. A) Roll vortices generated around a narrow obstacle. B) Vortical currents generated around the ends of a wide obstacle and rotors generated to leeward of the obstacle's main body.

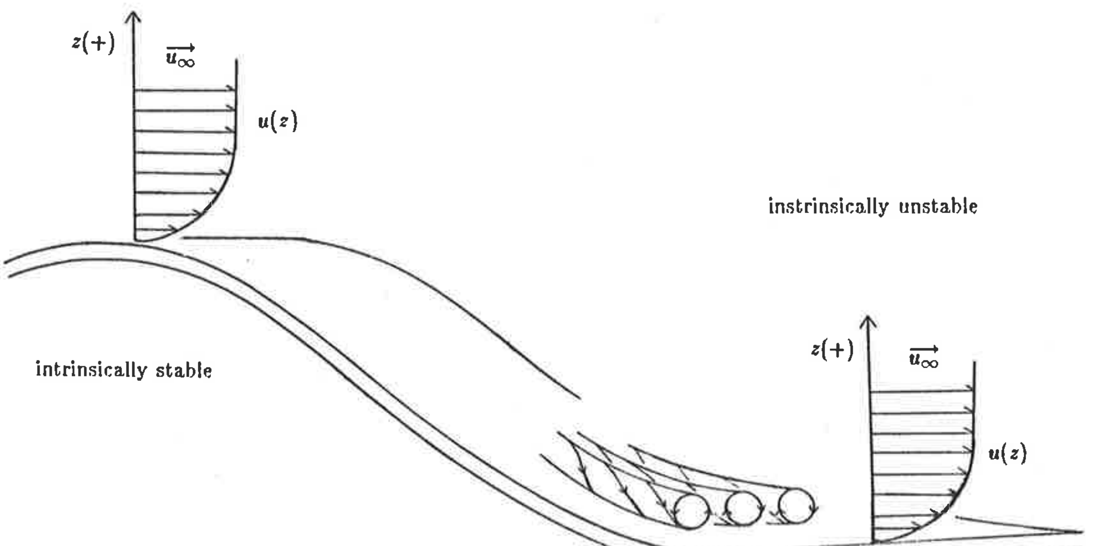

Figure 93. Görtler instability or instability over a concave surface. Note that in general, flow over a convex surface is intrinsically stable and flow over a concave surface is intrinsically unstable.

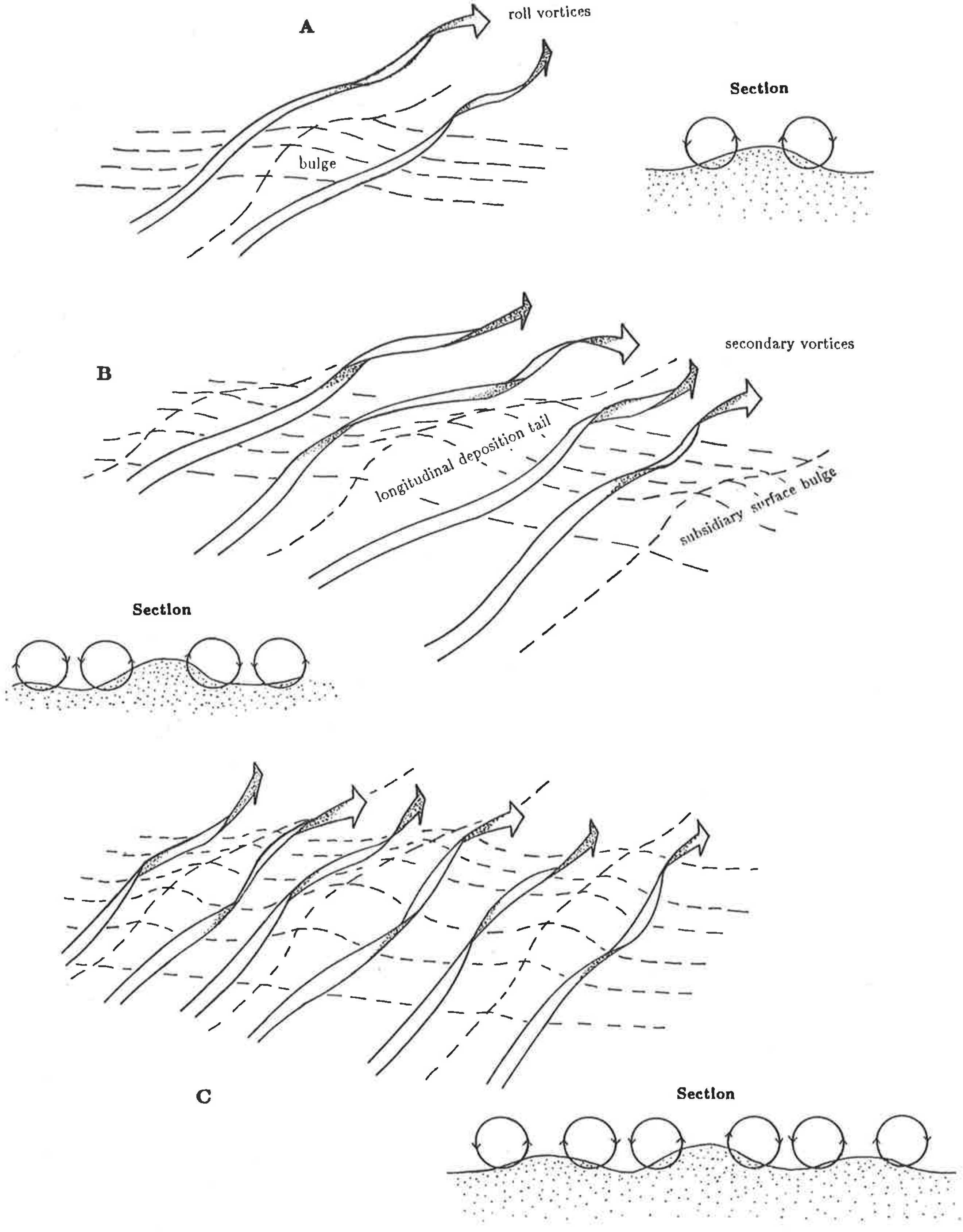

Figure 94. A) A bulge in a sand sheet gives rise to roll vortices. B) A longitudinal deposition tail is formed to leeward of the original bulge. As this linear mound grows, the roll vortices it gives rise to intensify. Secondary vortices are produced, and these initiate subsidiary surface bulges. C) A set of longitudinal mounds and their associated vortices pairs begins to form.

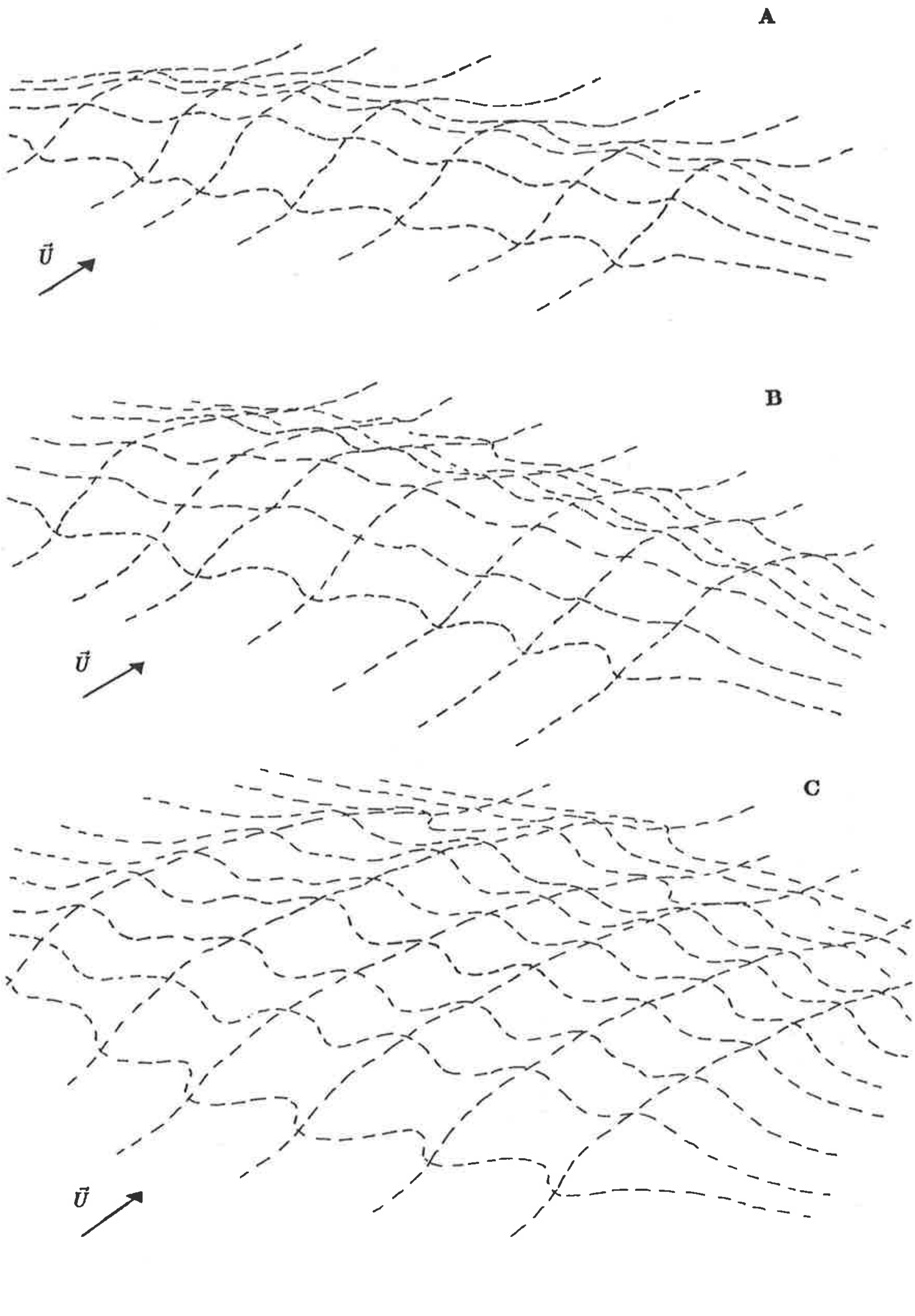

Figure 95 . The development of longitudinal dunes from a single debris mound. A) Original debris mound. B) The amplification of topographic irregularities and the initiation of longitudinal deposition tails. C) The development of longitudinal dunes.

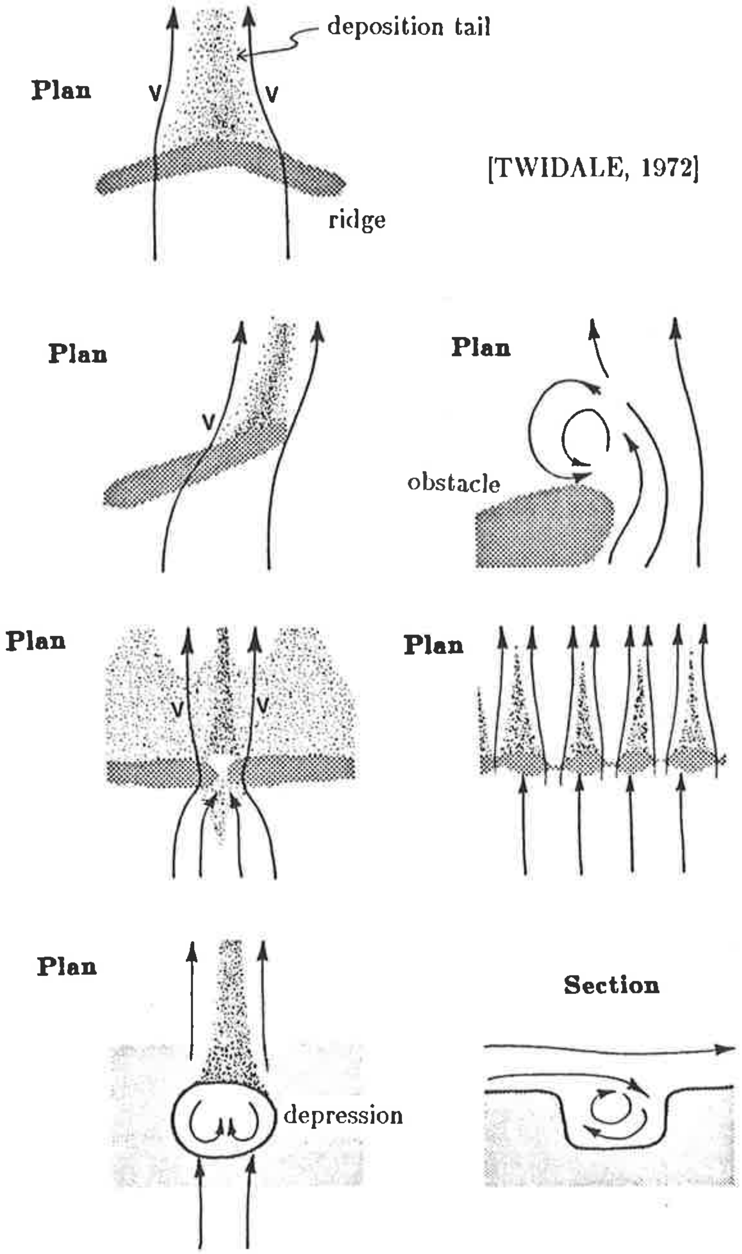

Figure 96. Leeward secondary flow and the resultant longitudinal deposition in wind tunnel trials using plasticene obstacles. V≡ vortices.

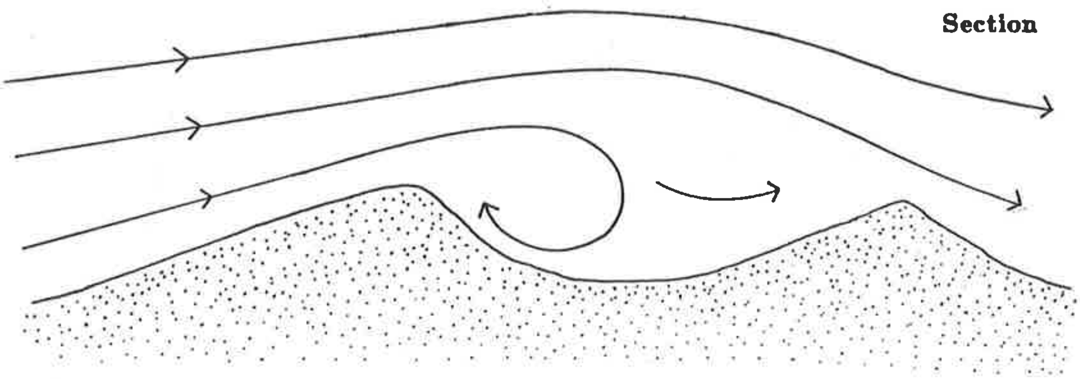

Figure 97. Wind rotor between two converging linear dunes.

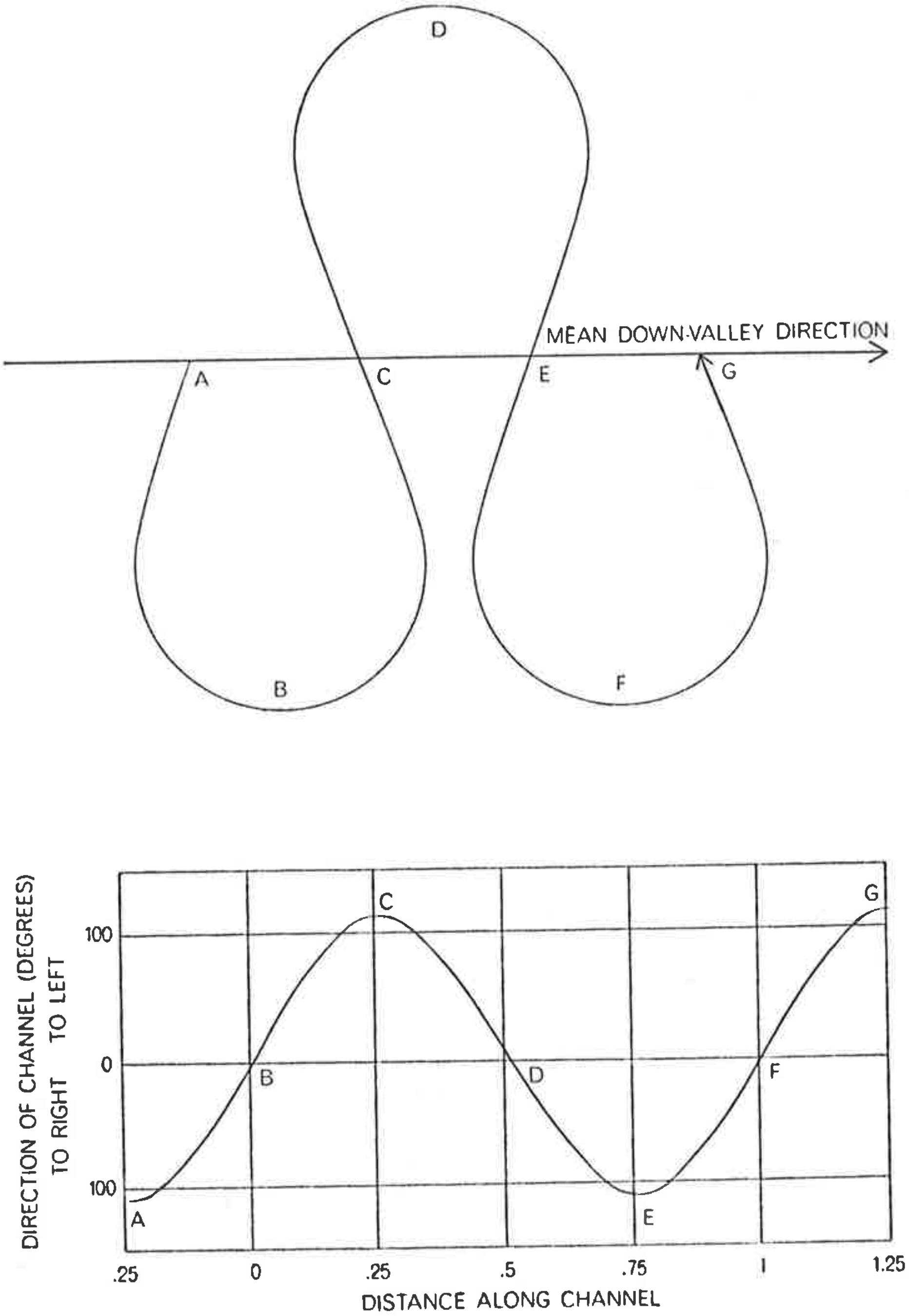

[LEOPOLD and LANGBEIN, 1966]

Figure 98. "Sine-generated curve *(top)* closely approximates the shape of real river meanders. This means that the angular direction of the channel at any point with respect to the mean down-valley direction *(toward the right)* is a sine function of the distance measured along the channel *(graph at bottom)*. At the axis of each bend *(B, D and F)* the channel is directed in the mean down-valley direction and the angle of deflection is zero, whereas at each point of inflection *(A, C, E and G)* the angle of deflection reaches a maximum value."

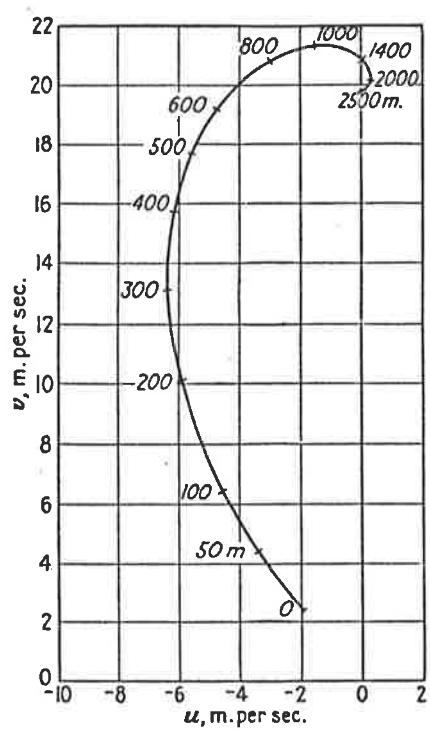

[HAURWITZ, 1941]

Figure 99. "Vertical variation of the wind distribution (Ekman spiral)."

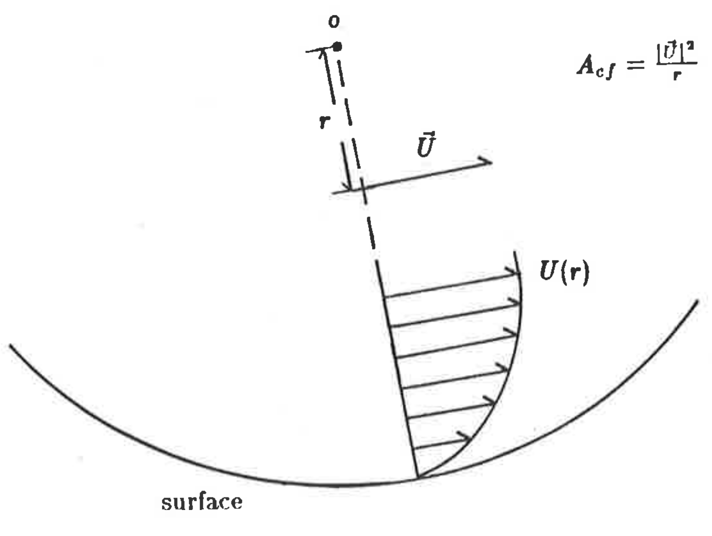

Figure 100. For flow over a concave surface, flow speed decreases non-linearly with distance away from the center of curvature and approaching the surface. Centrifugal acceleration at any point is equal to the square of the flow speed divided by the distance from the center of curvature. Therefore, flow centrifugal acceleration decreases non-linearly faster than does flow speed approaching the surface, and instability results. In the figure, o ≡center of curvature, r ≡radial distance to any point of interest and A_{cf} ≡centrifugal acceleration.